Viatcheslav Vanyukov

Effects of nonlinear light scattering on optical limiting in nanocarbon suspensions

UNIVERSITY OF
EASTERN FINLAND

VIATCHESLAV VANYUKOV

Effects of nonlinear light scattering on optical limiting in nanocarbon suspensions

Academic Dissertation
To be presented by permission of the Faculty of Science and Forestry for public examination in the Auditorium M 102 in Metria Building at the University of Eastern Finland, Joensuu, on August, 5, 2015, at 12 o'clock noon.

Department of Physics and Mathematics

Author's address: University of Eastern Finland
Department of Physics and Mathematics
P.O. Box 111
80101 JOENSUU
FINLAND
email: viatcheslav.vanyukov@uef.fi

Supervisors: Professor Yuri Svirko, Ph.D.
University of Eastern Finland
Department of Physics and Mathematics
P.O. Box 111
80101 JOENSUU
FINLAND
email: yuri.svirko@uef.fi

Professor Gennady Mikheev, Ph.D.
Institute of Mechanics
Ural Branch of Russian Academy of Sciences
426067 IZHEVSK
RUSSIA
email: mikheev@udman.ru

Reviewers: Professor Stelios Couris
University of Patras
Department of Physics
P.O. Box 1414
26504 PATRAS
GREECE
email: couris@iceht.forth.gr

Professor Nicolas Izard, Ph.D
Université de Montpellier
Place Eugène Bataillon
34095 MONTPELLIER
FRANCE
email: nicolas.izard@univ-montp2.fr

Opponent: Professor Werner Blau
Trinity College Dublin
The University of Dublin
College Green
Dublin 2
IRELAND
email: wblau@tcd.ie

ABSTRACT

This thesis reports the experimental investigation of the nonlinear light scattering and optical limiting in nanocarbon materials. The results are obtained by using the nonlinear transmittance and Z-scan techniques, which were combined with detecting of light pulses scattered in aqueous suspensions of carbon nanotubes and detonation nanodiamonds. The third-order nonlinear optical response of these materials was studied in the nanosecond and femtosecond time scales at the wavelengths of 532 nm, 800 nm, and 1064 nm, and within the optical communication window. The obtained results demonstrate that aqueous suspensions of detonation nanodiamonds possess a high ray stability and are attractive for optical limiting applications. The femtosecond Z-scan measurement at the wavelength of 800 nm also revealed a saturable absorption in this nanocarbon material.

Universal Decimal Classification: 535.36, 535.18, 546.2-026.743

Keywords: nonlinear optics; lasers; light scattering; nanostructured materials; carbon

Preface

First of all, I am very grateful my advisors, Professors Gennady Mikheev and Yuri Svirko, for guiding me through my PhD studies and for strong everyday support. I am also thankful to the Dean of the Faculty of Science and Forestry Professor Jukka Jurvelin and to the Head of the Department of Physics and Mathematics Professor Timo Jääskeläinen for granting me the opportunity to implement my research projects.

I also want to thank my co-authors Tatyana Mogileva, Alexey Puzyr and Vladimir Bondar for their contribution to our joint papers that form the basis of my Thesis. I also want to thank the Centre for International Mobility CIMO and Emil Aaltonen Foundation for the personal grants they provided.

I am grateful to the whole staff of the Department of Physics and Mathematics for help and assistance during my PhD studies. Special thanks to Dr Hemmo Tuovinen and Dr Kimmo Päivässari for providing me the possibility to work with nanosecond and femtosecond laser facilities, and to Dr Dmitriy Lyashenko for helping me with programming Z-scan experimental setups. I express my sincere gratitude to Hannele Karppinen and Katri Mustonen for all the help with administrative issues. I am also grateful to Pertti Pääkkönen, Tommi Itkonen, Timo Vahimaa and Unto Pieviläinen for their help and prompt response in my daily technical questions and requests.

I thank members of our research group, Rinat Ismagilov, Feruza Tuyakova, Mikhail Petrov, Petr Obraztsov, Tommi Kaplas, Denis Karpov and Semen Chervinskii for support and for nice time spent in and out of the lab.

In the end, I would like to thank the most valuable persons in my life, my parents Vladimir and Valentina, and my sister Natalia for their love and unfailing support. Last but not least, I want to express my deepest and warmest gratitude to my lovely wife Luiza for being with me from the first days of my research carrier.

Joensuu March 24, 2015   *Viatcheslav Vanyukov*

LIST OF ORIGINAL PUBLICATIONS

This thesis is based on data presented in the following articles, referred to by the Roman numerals I-VII.

I   Mikheev G. M., Mogileva T. N., Okotrub A. V., Bulatov D. L., Vanyukov V. V. Nonlinear light scattering in a carbon nanotube suspension. *Quantum Electronics 40, 45-50, 2010.*

II   Mikheev G. M., Puzyr A. P., Vanyukov V. V., Purtov K. V., Mogileva T. N., Bondar V. S. Nonlinear scattering of light in nanodiamond hydrosol. *Technical Physic Lett.36, 358-361, 2010.*

III   Vanyukov V. V., Mogileva T. N., Mikheev G. M., Okotrub A. V., Bulatov D. L. Application of nonlinear light scattering in nanocarbon suspensions for adjustment of laser pulse duration. *Journal of Nanoelectronics and Optoelectronics 7, 102-106, 2012.*

IV   Vanyukov V. V., Mogileva T. N., Mikheev G. M., Puzyr A. P., Bondar V. S., Svirko Y. P. Size effect on the optical limiting in suspensions of detonation nanodiamond clusters. *Applied Optics 52, 4123-4130, 2013.*

V   Vanyukov V. V., Mikheev G. M., Mogileva T. N., Puzyr A. P., Bondar V. S., Svirko Y. P. Concentration dependence of the optical limiting and nonlinear light scattering in aqueous suspensions of detonation nanodiamond clusters. *Optical Materials 37, 218–222, 2014.*

VI   Vanyukov V. V., Mikheev G. M., Mogileva T. N., Puzyr A. P., Bondar V. S., Svirko Y. P. Polarization-sensitive nonlinear light scattering and optical limiting in aqueous suspension of detonation nanodiamond. *Journal of the Optical Society of America B 31, 2990–2995, 2014.*

VII   Vanyukov V. V., Mikheev G. M., Mogileva T. N., Puzyr A. P., Bondar V. S., Svirko Y. P. Near IR nonlinear optical filter for optical communication window. *Applied Optics 54, 3290-3293 2015.*

AUTHOR'S CONTRIBUTION

The publications selected in this dissertation are original research papers on nonlinear light scattering and optical limiting in nanocarbon materials.

The papers **I**-**VII** present results obtained by the team members stated in the list of authors. The main ideas of the papers were created in productive discussions of all team members. In papers **I** and **II,** the author has contributed in performing Z-scan measurements, been involved in processing and analyzing the experimental data and participated in preparation the manuscripts. The experimental results on adjustment of the duration of nanosecond laser pulses by suspensions of carbon nanotubes presented in paper **III** were partially obtained by the author. The author has participated in analyzing the experimental data and wrote the manuscript. The experimental measurements and calculations on optical limiting performance of detonation nanodiamonds presented in papers **IV-VI** were mainly performed by the author. The author has contributed in the interpretation of the experimental results and wrote the manuscripts. In paper **VII,** the author has performed the experimental measurements, interpreted the results and prepared the manuscript.

The papers have been completed with significant co-operation with co-authors.

Contents

1 Optical limiting phenomenon

In this Chapter, we discuss on the optical limiting (OL) phenomenon and provide an overview on the major mechanisms responsible for the OL process, with an emphasis on nanocarbon materials.

1.1 OPTICAL LIMITING IN CONDENSED MEDIUM

In a number of materials with a strong optical nonlinearity, the absorption coefficient increases with intensity of the light beam. These materials are capable to limit the optical power entering an optical system, i.e. they can be used to protect sensitive equipment or human eyes [1]. The nonlinear phenomenon that manifests itself as a limiting of the optical power in the medium is called optical limiting (OL) [2]. Correspondingly, nonlinear optical devices that employ this phenomenon to control the intensity of the laser beams are usually referred to as optical limiters [3].

All photonic sensors including human eye have a threshold intensity above which they can be damaged. Placing a suitable optical limiter prior to the sensor prevents the injuring of the sensor and allows it to operate under safety conditions. Optical limiters essentially rely on optical nonlinearities and exploit a diversity of nonlinear mechanisms [1]. These mechanisms are conventionally identified using simple but powerful technique, the so called Z-scan technique (discussed in details in the section 3.2.1 of the Thesis), in which the intensity dependence of the optical transmittance of a material is measured by changing sample position with respect to the focal point of a lens [4]. The transmittance coefficient can be strongly influenced by the

nonlinear absorption, the nonlinear refraction, and the nonlinear light scattering, depending on the incident laser pulse excitation and the state of matter.

In the nanosecond time scale, the thermal mechanism of the optical nonlinearity dominates OL due to the strong light absorption, i.e. the OL takes place due to the transfer of the light energy absorbed by the host particles to the surrounding liquid. As soon as the local temperature exceeds the solvent evaporation temperature, the light scattering of the incident wave on the cloud of the microbubbles created in the focal area reduces the intensity of the light passed through the suspension, thus enabling the OL [5]. For the ultrashort time scale, i.e. for femtosecond laser pulses, the thermally induced nonlinear scattering is much weaker than that for the nanosecond laser pulses because the bubble formation time is of the order of nanoseconds. The limiting of the femtosecond laser pulses with the intensity of much higher than that of nanoseconds is dominated by the electronic response of the matter with an essential requirement of a strong nonlinear absorption [6]. The nonlinear refraction response may also contribute in materials transmittance decrease in the femtosecond time scale.

Materials that can be employed for fabrication of the optical limiters should possess a high damage level, a low limiting threshold in a wide spectrum range and a fast response time. Considering the state of matter, liquids are often more convenient because they are exceedingly resilient. In liquids, the absorbed energy of the sufficiently long light pulse is efficiently dispersed via heating and bubbling of the solvent, while in solids, the increase of the temperature is accompanied with the stress and typically results in the optical damage of the material [1]. That is why the attention of the optical community has recently been attracted to the suspensions of the various nanocarbon species (e.g. carbon nanotubes, carbon black, nanodiamonds, graphene flakes etc.) that show strong nonlinear absorption in the spectral range that spans from the visual to the far infrared [5,7–10]. In this Chapter, we provide a review on the optical limiting addressing the advantages and weaknesses of particular nonlinear media.

1.1.1 Optical limiting in suspensions of carbon-based nanomaterials

Nanocarbon materials are widely recognized as efficient optical limiters. Suspensions of carbon black, carbon nanotubes (CNT), fullerenes, onion-like carbon (OLC), graphene and nanodiamonds (ND), all have been found exhibiting a significant nonlinear extinction effect with intense laser beams.

The possibility of changing their chemical properties by binding various functional groups and recent advances in the CNT fabrication technology makes carbon nanotubes especially attractive for the OL applications [11,12]. This is partially because being a one-dimensional nanostructure, CNT can be functionalized [13]. However due to the relatively high surface energy, CNT tend agglomerate into clusters, which become a serious barrier in their practical application. Fortunately it have been found that CNT can be dispersed in the range of polymers [14–16] and amide solvents [17,18] and in these dispersion CNTs can exist stably as individual nanotubes or small bundles for reasonable periods of time [13]. The synthesized polymer-CNT composites [15,16] demonstrate strong nonlinear attenuation effect of nanosecond laser pulses at the wavelength of 532 nm. The debundled in the *N*-methyl-2-pyrrolidinone solvent single-walled CNT [19] with a diameter of 2 nm at the wavelength of 532 nm show strong nonlinear extinction coefficient with a low limiting threshold [18]. The suspended in ethanol CNTs have shown superior OL performance in comparison with fullerene C_{60} in toluene and carbon black in water in a wide spectral range [20]. Z-scan and pump-probe time-resolved experiments have revealed that in a wide range of incident fluences, the OL in CNT suspensions originates from the solvent vapour bubble growth and from the sublimation of nanotubes [5]. Solvent vapour bubbles are formed due to the heat transfer from nanotubes to the surrounding liquid, while the sublimation of nanotubes corresponds to the phase transition (from solid to gas) of nanotubes [5]. Unsurprisingly for such thermal effects, the longer the pulse, the stronger the OL [5].

Table 1.1 summarizes factors including CNT structure and thermodynamic properties of solvent influencing on the OL performance in CNT suspensions [5,13].

Table 1.1. Summary of the factors that influence of the optical limiting response in CNT suspensions. The signs of inequality indicate the contrast of the optical limiting responses. Table has taken with permission of publisher from [13].

Effects on optical limiting		Optical limiting response	References
Nanotube structure	Single/multi-wall	Comparable	[21]
	Bundle diameter	The larger > the smaller	[18,21]
	Length	The longer ≈ the shorter	[21]
	Number density	The denser > the sparser	[17]
Thermo-dynamical properties of solvents	Boiling point	The higher < the lower	[18,22]
	Surface tension	The larger < the smaller	[18,22]
	Viscosity	The higher < the lower	[18,22,23]
Incident laser beam	Wavelength	The longer < the shorter	[24]
	Pulse duration	The longer > the shorter	[24,25]
	Repetition rate	The higher < the lower	[23]

It is clearly seen from the Table 1.1, that the OL properties are sensitive to the bundle diameter. Specifically, CNT bundles with larger diameter have bigger scattering centers, which are more efficiently transfer heat from the CNT to the host liquid. This results in a faster vapour bubble growth and thus gives rise to a lower OL threshold and better OL performance [18,21]. In contrast, the length of the CNT hardly effects on the OL properties [21]. At the same time, it is difficult to whether single- or multiwall CNT perform better in the OL. Along with the nanotube structure, the thermodynamic properties of the solvent strongly influence the performance of CNT in the optical limiters. In particular, the CNTs suspended in the solvent with a lower boiling point show a stronger nonlinear response. The thermo-induced vapour bubbles grow faster in a solvent with a smaller surface tension [18,22]. Following the Table 1.1, the OL response is stronger for a shorter wavelength [24], for a longer pulse duration [24,25], and for a lower repetition rate [23] which can be easily explained by the thermally induced nonlinear light scattering mechanism [13]. However suspensions of CNT usually

survive for not longer than few hours [22], unless they did not undergo a complex chemical processing [26].

Suspensions of OLC are also unstable with respect to sedimentation and have a low ray stability [27]. For example, the light-induced chemical reaction results in irreversible bleaching [27] of the OLC suspensions in dimethylformamide (DMF) at high fluence [28].

Fullerene solutions also possess OL properties and environmentally stable with respect to CNT suspensions. However the mechanism of the OL in fullerenes is different than that in CNT and OLC suspensions. Specifically, the OL in fullerenes originates from the reverse saturable absorption, which will be discussed in details in the section 1.2.1.2. The reverse saturable absorption takes place when the excited state absorption cross section is bigger than that of the ground state. This effect has been observed for C_{60} and for C_{70} fullerene films and solutions under 532 nm and 1064 nm excitations [1,2,29–31]. At these wavelengths, the OL performance of C_{60} toluene samples is better than that of C_{70} because the latter possesses a higher linear state absorption coefficient. That is the strong ground state absorption in C_{70} requires a much higher (in comparison with C_{60}) excited state absorption to achieve the same OL response [1]. Specifically, the OL threshold in C_{60} at 1064 nm is 40 GW/cm^2, while the transmittance of the C_{70} solution at this excitation remains the same. However, despite that fact that at this intensity both fullerenes are stable [31], the OL due to the reverse saturable absorption exists in a narrower spectral range in comparison with the thermally induced OL in CNT, ND or graphene.

OL in dispersed graphene have been recently intensively studied [9,10,32–35]. Strong broadband transmittance decrease of graphene dispersed in N–methyl–2–pyrrolidone (NMP), N,N–dimethylacetamide (DMA) and γ–butyrolactone (GBL) have been found accompanied with the increase in the scattered light signal at the wavelengths of 532 and 1064 nm [32,33]. The stronger limiting at the wavelength of 532 nm was observed for DMA sample as it has a lower (than GBL) surface tension. It has been found that the optical transmittance and the OL properties of

graphene and graphene-oxide are sensitive to oxygen-containing functional groups and structural defects. This finding can be employed to regulate the OL performance in these materials [34]. Graphene samples have been found possessing stronger nonlinear response in comparison with graphene-oxide at the first and second harmonics of the Nd^{3+}: YAG laser. Nonlinear light scattering along with two-photon absorption have been found main physical mechanisms responsible for the OL in graphene nanostructures [35]. As for graphene dispersed in DMA [33], the greater response have been found at the wavelength of 532 nm [35]. It have been found that for 3.5 ns laser pulses with the wavelength of 532 nm, the dispersed graphene-oxide single sheets exhibit saturable absorption or reverse saturable absorption depending on the solvent [10]. The graphene-oxide in chlorobenzene outperforms C_{60} in toluene and single-walled CNTs in tetrahydrofuran in terms of OL in the wavelength range of 450-1064 nm [10]. In [9], the graphene dispersed in organic solvents have been found limiting the laser pulses with repetition rates up to 10 Hz without losing in efficiency.

Comparing to other nanocarbons, nonlinear optical effects in nanodiamonds are less studied. OL in ND suspensions was to the best of our knowledge first reported by Koudoumas et al. He compared the OL efficiency in polydispersed and ultradispersed ND powders with onion-like structures and have found that the latter exhibits much stronger OL action [8]. The nonlinear optical response in ND suspensions was also been found to be directly correlated with the polydispersity of the ND suspensions effecting on the nonlinear light scattering [36]. A small amount of papers on the OL investigation in ND suspensions is probably because of nanodiamond suspensions become colloidal unstable under the laser action, i.e. under heating. Fortunately it has been recently shown that these particles can be modified to form aqueous suspensions [37,38], which are stable with respect to sedimentation and irradiation with powerful laser beams [39,40]. This makes detonation ND aqueous suspensions an attractive

material for OL applications. The original results on the OL in the ND suspensions are presented in Chapter 5 of the Thesis.

1.1.2 Optical limiting in nanocarbon films

Due to a high transmittance, thin film materials are among those who attract the attention for the OL applications. However film materials typically possess worse nonlinear response than suspended materials due to the absence of the host liquid for generating the scattering centers [6]. Additionally, the presence of a substrate makes the interpretation of the experimental data a difficult task because both film and substrate, especially for high intensity laser pulses, in particular for femtosecond pulses, contribute the OL. However Z-scan measurements with bilayer graphene on silicon carbide (SiC) substrate [41] have revealed that nanocarbon films have nonlinearity much stronger than the substrate.

In the experiment, the intensity of the femtosecond light beam varied in the range of 6 - 52 GW/cm^2. Figure 1.1 presents the reported in [41] the Z-scans of the bilayer graphene on the substrate (●) and the substrate alone (○) at 780 and 1100 nm. It is clearly seen that at the excitation wavelength of 1100 nm, the normalized transmittance of graphene on a substrate depends on the excitation intensity, while in a wide range of the incident intensities the substrate signal was zero. Accordingly, the dependence of the transmittance on the laser intensity have been found associated with graphene only [41]. It is worth noting that in bilayer graphene, the absorption saturation (i.e. decrease of the absorption losses) has been observed at low intensity of the incident beam, while the two-photon absorption (i.e. increase of the absorption losses) has been observed at high light intensity. One may expect that at larger intensities, the two-photon absorption will dominate resulting in strong OL. However, measurements performed at 780 nm have shown the absence of the two-photon absorption indicating a pronounced spectral dependence of the OL in bilayer graphene. This drastically

reduces the application potential when optical power limiting in a wide spectral range is required.
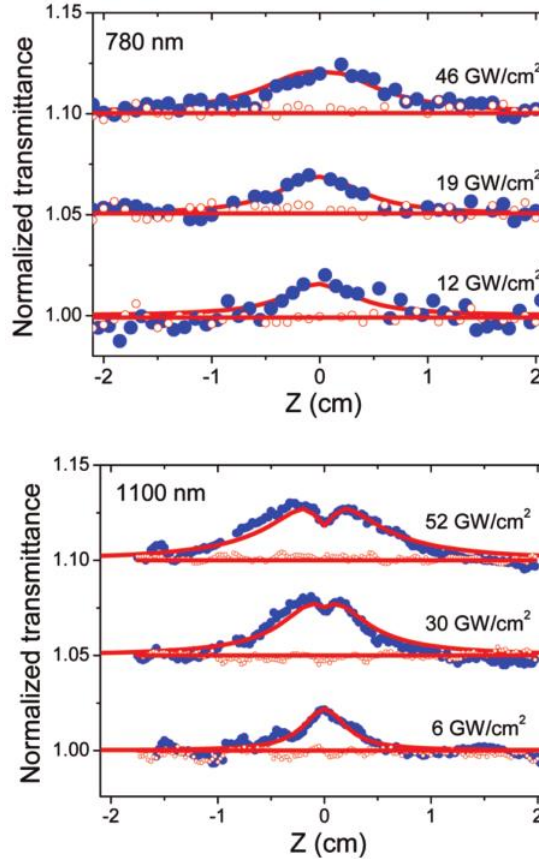
Figure 1.1. *The normalized transmittance of the bilayer graphene on the SiC substrate (●) and the substrate alone (○) in dependence on the sample position z. The measurements are performed for femtosecond laser pulses at the wavelengths of 780 and 1100 nm. Solid lines represent results of fitting. Picture has taken with permission of publisher from [41].*

In contrary to bilayer graphene on SiC substrate, thin films of graphene oxide on glass and plastic substrates have been found possessing a tunable widespread nonlinear optical response under femtosecond laser excitation [6]. The as-prepared graphene oxide films on glass substrates founded display extraordinary OL response both at 400 and 800 nm with a huge

two-photon absorption coefficient at 400 nm and effective two- and three-photon absorption coefficients at 800 nm. Most surprisingly, their OL responses were found to be expressively improved upon partial reduction of graphene oxide [6], which can be chemically or laser-induced achieved. The laser-induced reductions of graphene oxide result in significant improvement up to 19 times of the two-photon absorption coefficient at 400 nm and up to 12 and 14.5 times of the two- and three-photon absorption coefficients at 800 nm, respectively. The OL threshold of a 380 nm thick partially reduced samples have been found as low as 0.12 and 37mJ/cm^2 at 400 and 800 nm, respectively, which are much lower than that of the previously reported materials [9,10,35] and already described in the section 1.1.1 of the Thesis. The chemically reduced graphene oxide samples showed behavior significantly dependent on the degree of reduction. Specifically the slightly reduced films displayed nonlinear absorption, whilst the highly reduced films have been found exhibiting a saturable absorption [6]. The deposited on a top of a plastic highly chemically reduced graphene oxide films can be used as a flexible and broadband femtosecond pulses optical limiters.

Along with graphene and graphene oxide films, OL was studied also in polymer/carbon nanotube composites. It has been found that in these composites, the higher carbon nanotube mass content films block the incident light more effectively at higher incident pulse intensities [12]. The nonlinear mechanism involved in the OL in these CNT films along with nonlinear light scattering referred to nonlinear absorption and nonlinear refraction.

In should be noted that as for the SiC bilayer graphene, and for the reduced graphene oxide films, at some experimental conditions the saturable absorption may strongly contribute to the nonlinear transmittance for pico- and femtosecond pulses. This nonlinear optical mechanism, which is completely opposite the optical limiting, have been found responding also in the carbon nanotube films [42] for picosecond laser pulses, making the above materials also suitable for mode-locking applications.

1.1.3 Optical limiting in metal-based nanomaterials

Metal-based nanomaterials possess high and fast nonlinear optical response [43,44], which significantly increases at the surface-plasmon resonances (SPR) [45]. The nonlinear optical response of the metal-based nanomaterials was extensively studied in the ensembles of metal nanoparticles embedded in glass, i.e. glass-metal nanocomposites (GMN) and in metal particles colloidal solutions.

The nonlinear optical properties of glass-metal nanocomposites were widely studied in silver, copper, gold, and platinum-based GMN using the closed and the open-aperture Z-scan setups [12–15]. As the copper nanoparticles with the size of 3-5 nm are situated 60 nm beneath the glass surface, at 1064 nm the GMN shows both the self-focusing and the self-defocusing depending on the type of the host glass. Specifically, in glass consisting of 70% of SiO_2, 20% of Na_2O and 10% of CaO (matrix 1), the OL have been found originating from the self-focusing process. In contrary, in pure silica glass (100% of SiO_2, matrix 2), the self-defocusing has been observed [47]. Simultaneously, both glasses embedded with silver nanoparticles with size of 2-18 nm showed the self-defocusing effect. In the open-aperture Z-scan configuration, the incident intensity increase have been found giving rise to the transmittance of the silver nanoparticles samples (see Fig. 1.2, *a*), i.e. to saturable absorption (SA). The theoretical calculations with the SA absorption coefficients of **-** 6.7×10^{-5} and **-** 3.6×10^{-5} cm/W for silver nanoparticles in matrixes 1 and 2, respectively [48], have been found well approximating the experimental data as on can see from Fig. 1.2, *a*. The open-aperture Z-scan normalized transmittance for copper nanoparticles embedded in matrix 2 have been found (see Fig. 1.2, *b* [31]) possessing a possible competition between two nonlinear effects, SA and reverse saturable absorption (RSA). The RSA process takes place when the excited state absorption cross section is larger than the ground state (refer to 1.2.1.2 section). The RSA with absorption coefficient as high as 6×10^{-6} cm/W at 532 nm have been found resulting in the laser power attenuation as one

can see from the Fig. 1.2, *b*. However, this behavior has been found not existing at 1064 nm, making OL in glass-metal nanocomposites wavelength selective.
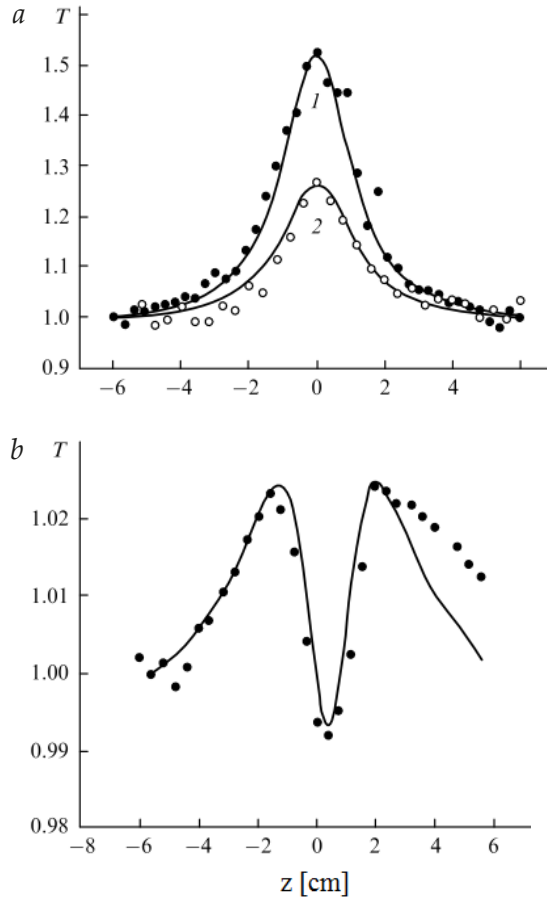
Figure 1.2. *The normalized transmittance of silver nanoparticles embedded in matrix 1 (70% of SiO_2, 20% of Na_2O and 10% of CaO, curve 1), and matrix 2 (pure silica, curve 2) (a), as well as copper nanoparticles embedded in matrix 2 (b) as functions of sample position z. The transmittance curves are obtained from the open-aperture Z-scan at excitation wavelength of 532 nm. Dots represents experimental data, while curves correspond the theoretical calculations [48]. Picture has taken with permission of publisher from [31].*

At the same time, the RSA have been found to be the leading nonlinear absorption mechanism in silver and platinum colloidal

solutions at 1064 nm [50]. In this case, the energy of the photon is not enough to induce two-photon absorption related either with SPR or with interband transitions [45]. For the gold colloids, the RSA process was also found to occur at 532 nm, whilst at 1064 nm both RSA and two-photon absorption have been found to occur [50]. In contrary for the silver-based aqueous suspension at 532 nm, the OL originated from the absorption-induced nonlinear scattering was observed [51]. The scattering was attributed on the micro-bubble induced scattering centers formation at the small laser spot. Nonlinear light scattering was also appealed to be dominating in the transmittance decrease in the gold nanoparticles with clearly laser fluence dependence. Specifically at small laser fluences the solvent bubble formed, while at high fluences fast expansion and vaporization of the particles occurred [52,53]. The effect of the metal nanoparticle size on the OL performance was studied under nanosecond excitation in gold colloidal solutions in the range of 2.5-15 nm. It was found that at 530 nm (almost at the SPR) the OL threshold decreases and its amplitude increases with increasing the particle size. The effect was caused by the scattering centers formation due to the particles vaporization [53]. For the same gold particles, the OL performance dependence on the excitation wavelength was reported. Specifically it was established that OL effect is more efficient below SPR, and decreases towards the red [52]. Size dependent third-order susceptibility associated with strong nonlinear refraction was found to be a central OL mechanism in colloidal solutions of copper nanoclusters [44]. Similar results on the optical Kerr effect have been observed in the colloids of gold [43] and colloidal silver particles with dependence on the rate of aggregation [50]. Most interestingly, that the absorption spectra in colloidal solutions of gold, silver, and platinum have been found to be shifting under the picosecond laser pulse excitation [50]. Specifically, the maxima of the optical density for the gold colloids was found to be shifted from their SPR, i.e. from 525 nm to the range of 525-550 nm, what is attributed to the metal particles aggregation under the picosecond laser pulses.

1.2 MECHANISMS OF THE OPTICAL LIMITING

Optical limiters may employ different mechanisms of the optical nonlinearity that may lead to nonlinear absorption, nonlinear refraction and the nonlinear light scattering. In particular, the nonlinear light absorption may arise from the multiphoton absorption, reverse saturable absorption, or free-career absorption. Among mechanisms of the nonlinear refraction is the electronic Kerr-effect, optically-induced heating, and photorefraction. Nonlinear light scattering, i.e. increasing of the scattering cross section at high intensities, may originate from the optically-induced heating at low light intensities and the particles sublimation or plasma formation at the high intensity regimes. Below we discuss variety nonlinear optical mechanisms that can be applied to fabricate optical limiters.

1.2.1 Nonlinear absorption

Nonlinear absorption manifests itself as the dependence of the absorption coefficient on the light intensity. For the OL applications, it is of practical interest when the increase of the light intensity results in the increase of the absorption coefficient. This may take place due to the multiphoton absorption, reverse saturable absorption and free-career absorption.

1.2.1.1 Multiphoton absorption

Multiphoton absorption is an optical process when two or more photons are absorbed simultaneously. For the two-photon absorption (TPA) the interaction of electromagnetic radiation with matter can be described by the equation in the 'Lambert-Beer' form $dI/dz = - (\alpha_0 + \beta I) I$, where α and β are linear and two-photon absorption coefficients. If the linear absorption is negligibly small, the intensity of the transmitted light beam is [13]:

$$I(L) = I_0/(1 + I_0 \beta L), \qquad (1.1)$$

where I_0 incident pulse intensity and L is the propagation length. It is clearly seen from Eq. (1.1) that the increasing on the incident light intensity results in decreasing the transmitted light intensity thus enabling OL. At very high intensities ($I_0 \beta L \gg 1$), the transmitted intensity is given by $I(L) \approx 1/\beta L$, i.e. the TPA may reduce the transmittance of the medium $T_{TPA} = I(L)/I_0$ down to zero resulting in a perfect OL [13].

The cross section of the two-photon absorption is determined by the two-photon absorption coefficient β and depends on the wavelength [13]. In addition, the two-photon induced OL is more efficient for the shorter pulse durations because the intensity of the shorter pulses is higher than for the longer pulses. The multiphoton absorption can coexist with other nonlinear mechanisms such as the nonlinear scattering and the nonlinear refraction thus improving the OL efficiency.

1.2.1.2 Reverse saturable absorption

RSA can be observed in a system that absorbs more in the excited state than in the ground state [1,54]. If the cross section for the absorption from the ground and the excited states are respectively σ_1 and σ_2, the material becomes more transparent when $\sigma_1 > \sigma_2$. This is because the population difference between the ground and the excited states decreases when the system absorbs light. If $\sigma_2 > \sigma_1$, i.e. when the population difference between the ground and the excited states decreases when the system absorbs light, the total absorption increases. These materials are known as reverse saturable absorbers [1]. The simplest electronic system possessing RSA has three vibronically broadened electronic energy levels [1].

In contrast to TPA, RSA cannot lead to an ideal OL, i.e. zero transmittance at high intensities. Blau et al. have demonstrated that the minimum transmittance that can be achieved by RSA mechanism is $T_{RSA} = (T_0)^{\sigma_2/\sigma_1}$, where T_0 is the linear transmittance [55].

1.2.1.3 Free-carrier absorption

In semiconductors, one- or two-photon absorption leads to generation of electrons in the conduction band and holes in the valence band. This results in the free-carrier absorption (FCA) that manifests itself similarly to the excited-state absorption in molecular systems [1]. FCA can be taken into account in the intensity propagation equation in the following form [1]:

$$\partial I/\partial z = -(\alpha + \sigma N)I, \tag{1.2}$$

where α is a linear absorption, σ is the total (electron + hole) FCA cross section, and N is the number of electron-hole pairs. One can observe from Eq. (1.2) that semiconductors with larger FCA cross section σ can exhibit stronger nonlinear optical response. The FCA-induced nonlinear response is independent of the incident pulse duration provided that pulse is shorter than the time required for the diffusion and the recombination of free carriers [13]. FCA may result in the OL in the wide spectral range.

1.2.2 Nonlinear refraction

The effect of the intensity dependent refractive index change is called nonlinear refraction [1]. The dependence of material refractive index on light intensity may be associated with a variety of physical processes, for example with electrostriction, i.e. with light-induced stress in the irradiated area. Another mechanism of the nonlinear refraction is the reorientation of anisotropic polarized molecules in liquids and gases in the polarized light beam that leads to the birefringence, i.e. change of the refractive index. This effect is often referred to as the high-frequency Kerr effect. The changes in the density and hence in the refractive index may be caused by heating also.

One of the important manifestations of the nonlinear refraction is the self-focusing and self-defocusing of the intense laser beams caused by inhomogeneous change of the refractive index over the beam cross section. Specifically, when the refractive index of the medium increases (decreases) under

irradiation, this media changes the wave front of the propagating light beam similarly to a positive (negative) lens. Correspondingly the light beam propagating in such a media will either converge (self-focusing) or diverge (self-defocusing) [1]. The nonlinear refraction is associated with the real part of the third order optical susceptibility $\chi^{(3)}$, i.e. it is not caused by the absorption losses in the medium. However, the nonlinear refraction can be used for the OL. The schematic of the optical limiter based on the phenomenon of the self-focusing is presented in Fig. 1.3.
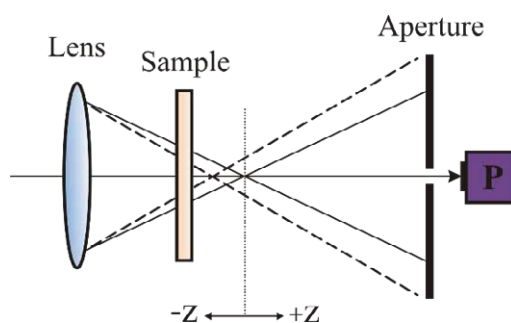
Figure 1.3. *The sketch of the optical system with the sample possessing the self-focusing effect placed before the focal point of the collecting lens. The dot lines show the shifted focus position.*

When the light intensity in the material is not sufficient to produce a noticeable nonlinear refraction, the light power measured by the detector after the aperture is a linear function of the incident beam intensity. However when the light intensity increases, the nonlinear refraction results in the shifting of the focal point, i.e. the beam waist position is shifting closer to the lens (dotted line in Fig. 1.3) [31]. As a result, the beam divergence in the far-field increases, and correspondingly the ratio of the optical power measured by the detector to the incident light intensity (i.e. the transmittance) decreases (Fig. 1.4). In contrary, the transmittance increases when the nonlinear refraction results in decreasing of the refraction index [4].
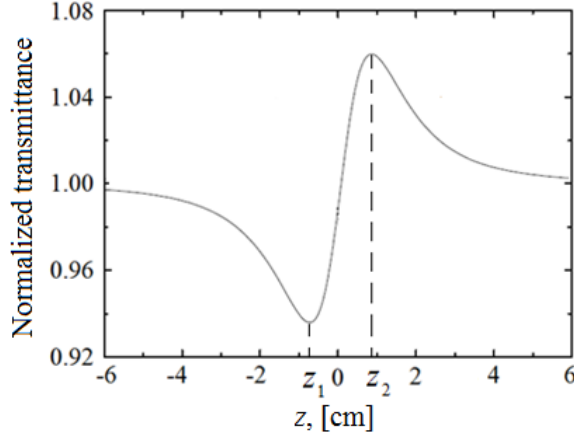
Figure 1.4. *The normalized transmittance as a function of sample position z. Picture has taken with permission of publisher from [4].*

Quantitatively this can be described by considering the self-focusing in the sample with the thickness much smaller than the diffraction length when the change of the beam profile inside the sample is negligible [4]. In the simplest case, the light-induced change in the refractive index is proportional to the light intensity. Therefore in the Gaussian beam, the radial dependence of the intensity gives rise to the following dependence of the refractive index change near the beam axis [1]:

$$\Delta n = \frac{\Delta n_0 e^{-2r^2}}{\Psi_0^2} \cong \Delta n_0 \left(1 - \frac{2r^2}{a\Psi_0^2} \right),$$ (1.3)

where Δn_0 is the on-axis index change, r is the radial distance, a is the correction term to the Taylor expansion for the higher order terms and Ψ_0 is the electric field radius associated with the beam in the medium. For the thin nonlinear medium with thickness L, the parabolic approximation yields a thin spherical lens with a focal length of [1]:

$$f = a\Psi_0^2 / 4\Delta n L.$$ (1.4)

Equation (1.4) clearly shows that the effective focal length of the lens decreases as the strength of the nonlinearity (Δn) increases [1]. If the nonlinearity of the medium is negative, then the effective focal length is negative, i.e. the self-defocusing arises. In contrary, if the nonlinearity is positive, then the effective length is positive, i.e. the self-focusing occurs [1].

1.2.3 Nonlinear scattering

The presence of irregularities in the medium that can be associated with variations of the refractive index, results in the scattering of light, i.e. gives rise to the extinction of the light beam. When the power of the incident light is high enough to produce or modify scattering centers in the media, the scattering cross section increases with the intensity suppressing the intensity of the transmitted light leading to OL [1].

The nonlinear light scattering caused by formation of the scattering centers under the laser irradiation can be pronounced in liquids, in which the local variation of the refraction index in the irradiated area is strongly influence by diffusion processes. In liquid media the scattering centers can be created by injecting nanoparticles that possess a high absorption coefficient. The light power is absorbed by the nanoparticles and heats the surrounding liquid until the local temperature exceeds the solvent evaporation temperature. As soon as the evaporation temperature of the solvent is achieved, microbubbles are generated. The size and hence scattering cross section of these microbubbles increases with incident fluence giving progress in the suppression of the transmittance, i.e. to the OL. The further increase of the fluence results in the sublimation of particles and formation of microplasma, which also results in efficient light scattering.

In more details, the nonlinear light scattering phenomenon is discussed in Chapter 2.

2 Linear and nonlinear light scattering

In this chapter, we present an overview of the linear and the nonlinear light scattering and describe mechanisms of the nonlinear light scattering in suspensions of carbon nanoparticles.

2.1 LINEAR LIGHT SCATTERING

Light scattering manifests itself as an appearance of weak (scattered) waves with frequencies and directions that may be different from the incident wave [56]. This phenomenon originates from light-induced oscillations of electrons in the medium that emit new scattered waves [57]. When all electrons oscillate in phase, the emitted radiation results in refraction of the incident light wave in the medium. However inhomogeneity caused by e.g. tiny particles or local variation of the refractive index will lead to dephasing of the emitted waves and hence to the light scattering. Quantitatively the scattering can be described in terms of the variations of the refractive index of the medium. It was first experimentally studied in 1869 by Tindall. The theory of this phenomenon was developed by Lord Rayleigh [58,59].

2.1.1 Elastic scattering

When the frequency of the incident and scattered waves are the same, the scattering is referred to as elastic light scattering. The scattering cross section primarily depends on the relationship between the wavelength and the particle size. For the particle size below 1/15 of the wavelength, the scattering is called the Rayleigh scattering, whilst for larger particles the scattering is referred to Mie scattering.

The Rayleigh scattering, i.e. an elastic light scattering by the particles much smaller that the wavelength of the radiation, results from the electric polarizability of the particles. The vibrating electric field light wave behaves on the charges inside the particle, initiating them to action at the same frequency. As a result, the particle turns to a small radiating dipole. This dipole radiation we see as the scattered light. The intensity of the scattered by any one of the small particles with the diameter d and refractive index n from unpolarized light beam is given by [60]:

$$I = I_0 \frac{1 + \cos^2 \theta}{2R^2} \left(\frac{2\pi}{\lambda}\right)^4 \left(\frac{n^2 - 1}{n^2 + 2}\right)^2 \left(\frac{d}{2}\right)^6, \qquad (2.1)$$

where θ is the scattering angle, r is the distance to the particle, λ is the incident light wavelength, I_0 is the intensity of the incident beam (see Fig. 2.1, a). One can see from Eq. (2.1) that the scattered light intensity is proportional to the power of six the particle size, and inversely proportional to the fourth power of the incident wavelength. These findings are of significant importance for the light scattering study.

Considering the theory of light scattering, it is of importance to notice its dependence on the light polarization. The angular distribution of the scattering of a polarized light from a single molecule is described by the following equation [57]:

$$I(\theta, \varphi) = \frac{9\pi^2 \sin^2 \theta}{N^2 \lambda^4} \left(\frac{n^2 - 1}{n^2 + 2}\right)^2 P_0, \qquad (2.2)$$

where θ and φ are the polar and axial angles, respectively (refer to Fig. 2.1). Equation (2.2) shows that scattering diagram is axially symmetric with respect to the polarization of the incident wave, while the maximum scattering is observed in the plane perpendicular this direction (see Fig. 2.1, b). The scattered radiation is polarized, i.e. the electric field lays in the containing the polarization of the incident wave and the observation direction.
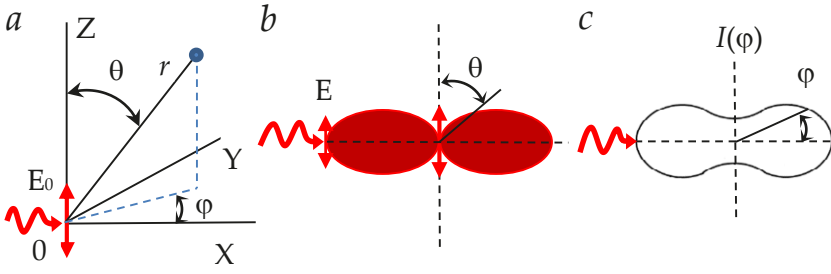
Figure 2.1. The sketch of the elementary light scatterer, where the incident light wave with an electric field oscillations in Y=0 plane propagates along X axis (a). Figures (b) and (c) represents the angular distribution of the scattered light intensity of a polarized and unpolarized light, respectively.

For the unpolarized incident wave, the scattered light intensity can be described by the following equation [57]:

$$I(\varphi) = \frac{9\pi^2}{2N^2\lambda^4}\left(\frac{n^2-1}{n^2+2}\right)^2 (1+\cos^2\varphi)P_0. \qquad (2.3)$$

The dependence $I(\varphi)$ is shown in Fig. 2.1, c. The scattering diagram is axially symmetric with respect to the propagation direction of the incident wave. Forward and back scattering have the same intensity and symmetrical with respect to the scattering center. For the unpolarized incident wave, the scattered light is a partially polarized light with the degree of polarization given by the following equation [57]:

$$P = \frac{\sin^2\varphi}{1+\cos^2\varphi}. \qquad (2.4)$$

It is evident from Eq. (2.4) that in the direction perpendicular to the incident beam ($\varphi = \pi/2$), the scattered light is completely linearly polarized ($P = 1$).

With an increasing the sizes of particles, the deviations from the Rayleigh theory predictions become noticeable and the Mie theory should be applied. The Mie theory allows one to present

the wave scattered by a spherical particle in terms of an infinite series of spherical multipole partial waves with parameter α [61]:

$$\alpha = ka = 2\pi a/\lambda, \tag{2.5}$$

where *a* is a radius of spherical particle. Despite the fact that Mie theory is applied for spherical shape particles mostly, the term "Mie scattering" is widely used to characterize the scattering of particles with arbitrary shapes.

The mechanism of the Mie scattering is similar to the Rayleigh scattering however, one should take into account that in large particles, elementary scatters separated at a finite distance placed in the medium with a finite refractive index. An important feature of the Mie scattering is its weak dependence on the wavelength for particles with linear dimensions much larger than the wavelength, which significantly differs from the Rayleigh scattering.

In addition to the Rayleigh and Mie scattering, the Thomson scattering is also considered as an elastic scattering. Thomson scattering is an elastic scattering of charged particles. The magnetic and electric fields of a light wave drive-in the charged particle as a result the rapidly moving charged particle radiate electromagnetic waves. Consequently, the energy of the incident wave is partially transferred into the energy of the scattered wave and scattering occurs. This type of scattering was explained by J. Thomson. The scattering cross section in Thomson's scattering does not depend on the electromagnetic wave frequency and remains the same for forward and backward scattering.

2.1.2 Inelastic scattering

The energy exchange between photons elementary excitations in the medium results in inelastic light scattering when the energies of the incident and scattered photons are different. In this section, we will briefly describe the Brillouin and Raman scattering.

In an elastic light scattering, the fluctuations of the refractive index or the medium permittivity δε are independent on time. Adding the time dependence leads to a new phenomenon in a

light scattering. In order to demonstrate this let us consider the propagation of the elastic wave in the medium. Assuming the permittivity ε of the medium being a function of the medium density ρ only, the variation of the permittivity can be written as $\Delta\varepsilon = (d\varepsilon/d\rho)\Delta\rho$ where $\Delta\rho$ represents the densities change due to elastic wave. Let us consider variations of the permittivity caused by two counter-propagated acoustic waves with frequency Ω:

$$\delta\varepsilon_1 = a_1 e^{-i(\Omega t - Kr)} + c.c., \tag{2.6}$$

$$\delta\varepsilon_2 = a_2 e^{-i(\Omega t + Kr)} + c.c. \tag{2.7}$$

where $|K| = \Omega/v$ is the wave vector and v is the speed of sound in the medium. When light wave with frequency ω and wave vector k, $E = E_0 e^{-i(\omega t - kr)} + c.c.$ propagates in the medium, the counter-propagated acoustic waves produce medium polarization (and, hence, in the scattered light waves) oscillating at Stokes (ω-Ω) and anti-Stokes (ω+Ω) frequencies:

$$\delta P_1 = \frac{E}{4\pi}\delta\varepsilon_1 = \frac{a_1 E_0}{4\pi} e^{-i[(\omega+\Omega)t - (k+K)r]} + \frac{a_1^* E_0}{4\pi} e^{-i[(\omega-\Omega)t - (k-K)r]}$$
$$+ c.c., \tag{2.8}$$

$$\delta P_2 = \frac{a_2 E_0}{4\pi} e^{-i[(\omega+\Omega)t - (k-K)r]} + \frac{a_2^* E_0}{4\pi} e^{-i[(\omega-\Omega)t - (k+K)r]}$$
$$+ c.c. \tag{2.9}$$

In the spectrum of the scattered radiation, we will observe Stokes and anti-Stokes Brillouin components of the same intensity. Considering the acoustic waves propagate at angle θ with respect to the light wave, the Brillouin frequency shift will be given by the following equation:

$$\Omega = \frac{4\pi\upsilon}{\lambda}\sin\frac{\theta}{2} = 2\,\omega n \frac{\upsilon}{c}\sin\frac{\theta}{2}, \tag{2.10}$$

where c is a light speed in vacuum and n is the refractive index of media.

However, time-dependent fluctuation of the optical susceptibility can also be associated with intramolecular motion that may affect the polarizability of the molecule. Interaction of light waves with such intramolecular motion gives rise to the Raman scattering, discovered almost simultaneously by Soviet physicists Mandelstam and Landsberg and Indian physicists Raman and Krishnan in 1928. The Raman scattering can be described in terms of the transitions between the vibrational states of the molecule or crystal. In Raman scattering, the difference in energy between the excitation and scattered photons corresponds to the energy required to excite a molecule to a higher vibrational mode. The scattered Stokes photons have lower energy, $E_S = \hbar \, (\omega - \Omega)$, where Ω is the frequency of the molecular vibration mode. However since at a finite temperature a considerable number of molecules are higher vibrational states, the scattered light will also have the anti-Stokes component at the frequency of $\omega_2 = \omega + \Omega$.

2.2 NONLINEAR LIGHT SCATTERING

2.2.1 Intensity effects in the elastic light scattering

The cross section of the linear (e.g. Rayleigh and Mie) scattering is determined by the size and refractive index of the scattering centers. However, when the intensity of the laser beam is increases, the refractive index and absorption coefficient of these centers are changing. In such a case, the energy of the scattered light is a nonlinear function of the incident power, i.e. the spontaneous scattering becomes a nonlinear process. The mechanism of the nonlinear spontaneous scattering is determined by the optical properties of the scattering centers and intensity of the light beam. If the absorption coefficient of the scattered centers is much higher than that of the surrounding medium and the pulse duration is longer than the characteristic time of electron-phonon relaxation, the temperature of the scattering center is rapidly increases. This changes its optical properties and thermal mechanism dominates the nonlinear

scattering. The dependence of the scattering cross section on the laser power may be much stronger if heating of the scattering centers immersed in host liquid results in the evaporation of the surrounded liquid. In this case, light scattering on the vapor bubble may give raise to the drastic increase in the scattering cross section in comparison with linear regime. The further increase of the fluence results in the sublimation of particles and formation of microplasma, which also result in efficient light scattering. This mechanism dominates OL in nanocarbon suspensions for nanosecond pulses and will be discussed in the sections 4.1-4.3 and 5.1-5.3.

In the femtosecond domain, when the pulse is shorter than the electron-phonon relaxation time, the no lattice heating take place and scattering will be determined by the temperature of the electron subsystem of the inclusion. In this regime, one may also expect that this strong and fast electronic nonlinearity will result in a considerable change in the spontaneous scattering cross section leading to either increase or decrease of the extinction coefficient. In the section 5.6 we will discuss this mechanism in more details.

In the inelastic processes, the increase of the light intensity may result in the stimulated e.g. Raman (SRS) or Brillouin (SBS) scattering due to resonance coupling between incident and scattered waves mediated by materials excitation (e.g. lattice phonons in crystals or density fluctuations in liquids). The stimulated originates from the parametric amplification of the scattered Stokes wave in the presence of the intense pump.

2.2.2 Nonlinear light scattering in suspensions of nanocarbon materials

Nonlinear light scattering often dominates OL in suspensions of carbon black, carbon nanotubes, nanodiamonds and graphene dispersions. The effective scattering occurs due to the formation of the scattering centers with dimensions of the order of the incident laser beam wavelength. There are three main sources of the formation of these scattering centers in suspensions of nanocarbons [13].

The first source is the formation of the vapor microbubbles. In the suspensions of CNT [5], carbon black [7] and graphene [62], light absorption results in heating of the carbon clusters and formation of the vapor microbubbles surrounding them. Vapor microbubbles can efficiently scatter light since the refractive index discontinuity at the vapor-liquid boundary is large [1]. The scattering of nanosecond pulses is more efficient since the vapor bubbles are formed during the pulse duration. The OL process in nanocarbon suspensions was theoretically described in [63,64] and considered the dynamics of the bubbles growth and the Mie scattering. Specifically, the OL process is described by the processes of the vapor microbubbles forming and growth dynamics as well as the Mie scattering on the growing microbubbles and the nonlinear propagation through the medium. The objects of the theoretical study [63,64] are spherical carbon nanoparticles, however based on the Mie theory estimates qualitatively work for CNT suspensions and are useful for understanding the dynamics of the bubble growth [62]. The results of the study showed that the scattering cross section significantly increases, while the absorption cross section decreases with increasing the vapor bubble radius (see Fig. 2.2, *a*). The scattering cross section depends on the incident intensity because the size of vapor bubbles nonlinear depends on the input fluence. Specifically, the vapor bubble radius increases when the input fluence increases (see Fig. 2.2, *b*). The increase of the bubble radius is significant at relatively low input fluence, whilst at higher fluencies (more than 0.1 J/cm^2) the increase is not as noticeable.

Another mechanism of the scattering centers formation is the sublimation of nanoparticles [5]. Comparing with a long time of vapor bubbles formation, the sublimation of the nanoparticles lasts for tens of picoseconds enabling a faster OL [52]. However the sublimation process requires much higher the incident fluence than the vaporization and can lead to the destroying the carbon nanoparticles. Therefore, the limitation based on the sublimation mechanism of the light scattering requires lower repetition rate.

In some cases absorption of the laser radiation and heat convection can change the refractive index of the surrounding solvent or the boundary between particles and solvent [53,65]. These inhomogeneous centers with the refractive index changing due to the laser radiation can also play a role of the scattering centers in the nanosecond domain [13].
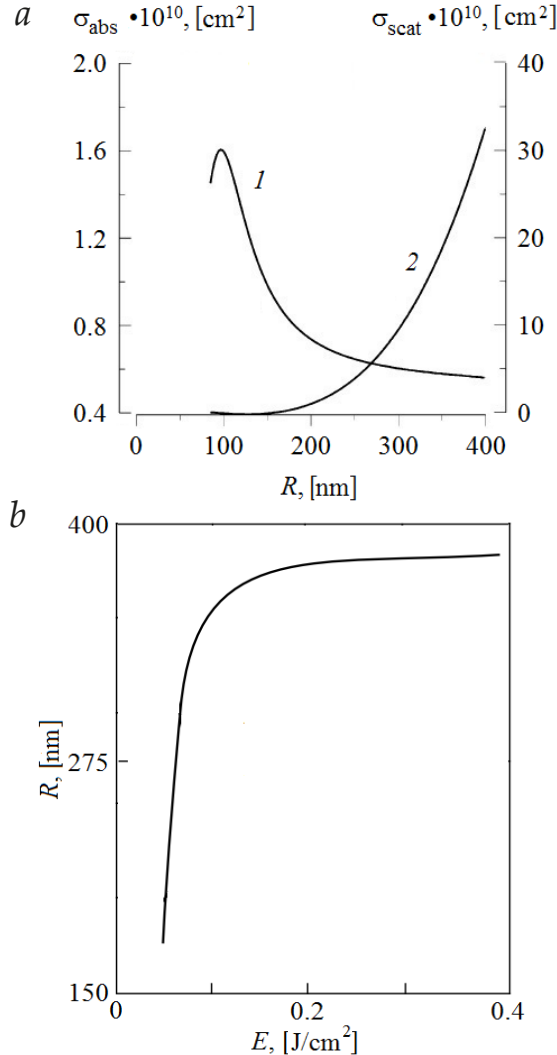

Figure 2.2. (a) The absorption 1, and scattering 2 cross sections as functions of vapor bubble radius R in suspensions of nanocarbon particles. (b) Vapor bubble radius R at the end of the laser pulse with pulse duration of 10 ns as a function of input fluence E. Pictures have taken with permission of publishers from [63] and [64], correspondingly.

Both vapor bubbles formation and sublimation mechanisms can exist in suspensions of carbon nanoparticles. The vapor bubbles are formed at the nanosecond time field at lower intensities, whilst the nanoparticle sublimation is usually takes place for picosecond laser pulses at higher intensities [13]. However, both mechanisms are existing in liquid solvents. The structure of the nanoparticles (average size, geometry, and the degree of aggregation) strongly influences on the attenuating properties because it plays an important role in the formation of the scattering centers [21]. Moreover, the thermodynamic properties of the solvents such as the boiling point, the surface tension, the viscosity and the thermal conductivity are closely related to the formation of the scattering centers, and hence to the OL efficiency what has already been presented in Table 1.1.

The nonlinear light scattering in suspensions of carbon black, carbon nanotubes and others has been widely studied. The dominant role of the nonlinear light scattering in suspensions of carbon black was showed by Mansour et al. in 1992 [7]. In the experiments, the absorbance and the fraction of the side-scattered light, and the transmittance were measured simultaneously. The experimental results revealed the insignificance of the nonlinear refraction, while the absorbance change being too small to explain the strong decrease in the transmitted light. For the incident fluence of 380 mJ/cm^2 when the strong limitation of the incident power was noticed, a strong fraction of the side-scattered light was observed (see Fig. 2.3 [7]). In the incident fluence range of $1 - 12$ J/cm^2, the fractions of the absorbed photons have been found decreasing. In contrary, the increase in the energy of the scattered radiation has been observed up to 12 J/cm^2 (see Fig. 2.3). The tiny suspended carbon particles are heated fast by strong linear absorption giving advance to the thermionic emission, which in the presence of a strong electric field leads to avalanche ionization [7]. The resulting microplasma then rapidly expands in the surrounding fluid and strongly scatters the incident light for the duration of the plasma existence (about 100 ns). Subsequently, when the incident energy is above the limiting

threshold, the heating leads to bubbles formation and further scattering that lasts for microseconds [7].
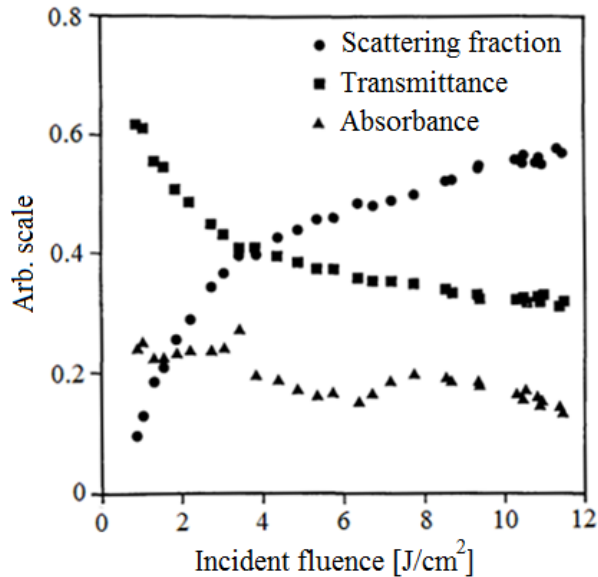
Figure 2.3. Absorbance, transmittance, and scattered fraction as functions of incident fluence for 1064 nm and 20 ns light pulses. Picture has taken with permission of publisher from [7].

In contrast to numerous studies on OL in CNT and carbon black suspensions, the studies on the nonlinear light scattering in the ND suspensions of are scarce. It has been demonstrated that ND enable high efficiency in limiting the laser beams of high intensities at the wavelengths of 532 nm and 1064 nm and that transmittance decreases due to the nonlinear absorption and nonlinear light scattering [39,40]. By using an ultracentrifugation it was shown that the OL efficiency by ND suspensions substantially depends on the particles polydispersity [36]. Suspensions of detonation ND clusters showed high stability to the periodic laser irradiation [40], which makes them extremely promising material for OL applications.

The OL and the effect of the nonlinear light scattering on the OL in suspensions of ND clusters described in details in Chapter 5 of this Thesis.

3 Experimental materials, techniques and instruments

This chapter presents the detailed description of the carbon nanomaterial samples, the experimental techniques, as well as the laser sources used for the measurements of their nonlinear optical properties.

3.1   MATERIALS

3.1.1 Suspensions of carbon nanotubes (CNT)

We studied OL in aqueous suspensions of multiwalled carbon nanotubes synthesized by the electric arc-evaporation of graphite [67]. To ensure the formation of a stable nanotube suspension in water and to remove glassy carbon nanoparticles, the samples were chemically treated as described elsewhere [68]. The oxidation of the multiwalled CNTs with a potassium permanganate solution ($KMnO_4$) in sulphuric acid (H_2SO_4) produce oxygen-containing surface groups, which ensure the formation of a colloidal CNT solution in water [69]. Deposition of carbon nanotubes was carried out using $FeCl_3$ solution. As a result of the hydrolysis, an iron hydroxide with forming a composite with oxidized CNTs was released. The air-dried composite was flooded with a small amount (~10 ml) of concentrated sulfuric acid and the mixture was kept in this state for days to dissolve iron hydroxide. The precipitate was washed on a filter to eliminate $FeCl_3$ with a 5% solution of hydrochloric acid until a colorless filtrate was obtained and then with distilled water - until a dark color of the filtrate appeared.

The obtained aqueous suspensions were stable for a rather long time (more than two years). The examination of the colloidal

solution of nanoparticles by a transmission electron microscope confirmed the absence of amorphous carbon and glassy carbon nanoparticles in the samples. At the same time, the sample also did not contain long CNTs. Most nanoparticles had a diameter of 15–20 nm and a length of less than 200 nm. The scanning electron microscope image of the prepared samples is displayed in Fig. 3.1.
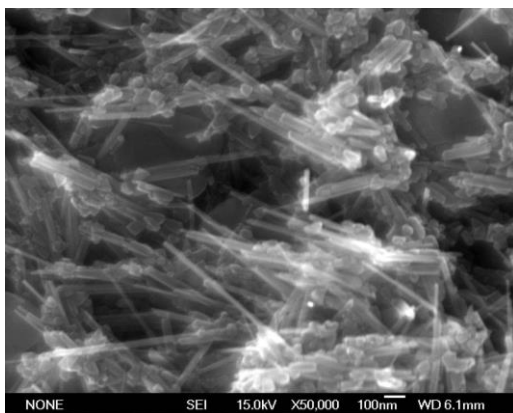

Figure 3.1. SEM image of carbon nanotube suspension with a diameter of nanotubes 15-20 nm and a length of less than 200 μm. The image was obtained with JEOL JSM-6700 F electron microscope.

3.1.2 Suspensions of detonation nanodiamonds (ND)

The ND clusters were manufactured using commercially available RDDM nanodiamonds [37], which were suspended in deionized water by ultrasonication. In order to remove surface impurities the ND clusters were treated in NaCl solution at atmospheric pressure and room temperature [70]. The treatment significantly increased the stability of ND suspensions with respect to sedimentation [37]. The chemical-physical properties of obtained ND were discussed in [37,71]. The X-ray diffraction pattern and high-resolution TEM image showed in Figs. 3.2, *a* and 3.2, *b*, respectively confirm that the treatment did not affect the ND crystallinity (see Refs. [37] and [40] for details).

The higher magnification TEM image of the obtained ND confirms the presents of a diamond core and approximately a monolayer coverage by sp^2 type carbon, which is either laying on the surface or forming a small blobs (semifullerenes). The

crystalline grain boundaries that are clearly visible from the figure indicate that agglomerates are not just particles stuck together, but serve as a solid and rigid crystalline body. The lower magnification analyses revealed that sp² monolayer is uniform over all particles.
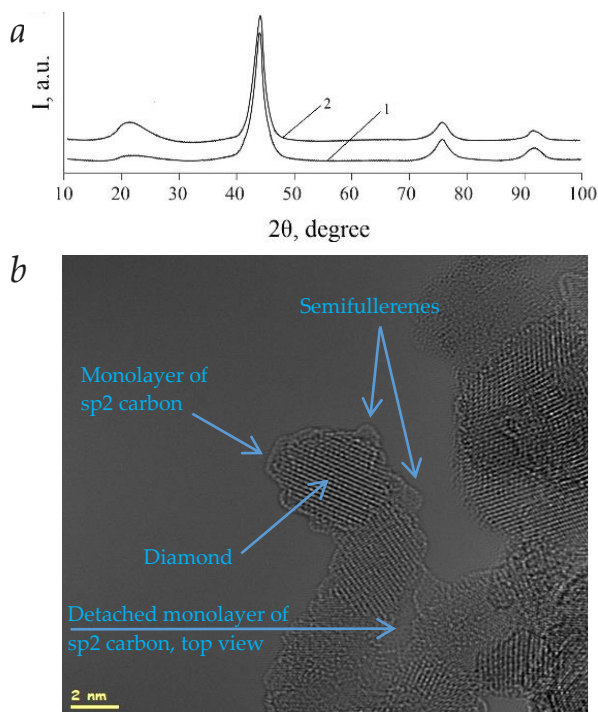
Figure 3.2. (a) The X-ray diffraction patterns of ND clusters with size of 50 nm (1) and 320 nm (2). The patterns were recorded on a DRON-3 diffractometer. One can observe the diamond reflections from the (111), (220) and (311) planes at $2\theta = 44.0°$, 75.7° and 91.6°, respectively. (b) High-resolution TEM image of the suspension with an average particle size of 50 nm was obtained with Titan 60-300 electron microscope (FEI, Netherlands).

The optical density of 1 mm thick samples of 0.03 (*1*) and 0.1 wt. % (*2*) aqueous ND suspension as a function of the wavelength and Raman spectra of the ND clusters are presented in Figs. 3.3, *a* and 3.3, *b*, respectively. The Raman spectra with the two excitation wavelengths of 473 and 633 nm (see Figure 3.3, *b*) clearly show the peak at 1325 cm^{-1} which is the ND signature [72–

74]. However, at the both excitation wavelengths, the Raman spectrum has a broadband background due to luminescence [75–77] of numerous defects and vacancies in ND particles [78].
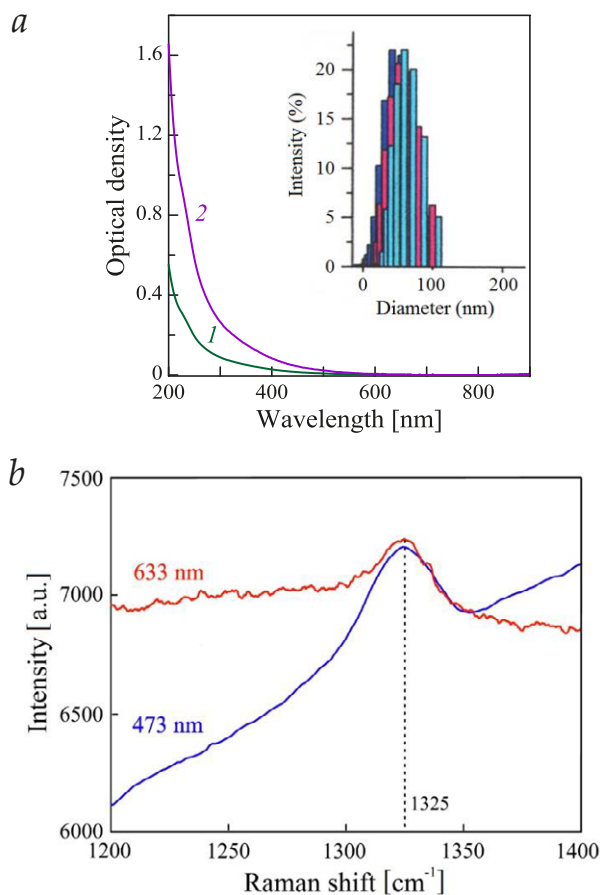
Figure 3.3. (a) Optical density of 1 mm thick samples of 0.03 (1) and 0.1 wt. % (2) aqueous ND suspension as a function of the wavelength. The inset shows the ND particle size distribution estimated by the dynamic light scattering technique. The average particle size is 50 nm. (b) Raman spectra of ND clusters at the excitation wavelengths of 473 and 633 nm. The ND clusters were prepared by evaporation of a liquid phase of the ND suspension at a temperature of 25 °C [75].

For the nonlinear light scattering study the ND clusters were separated in size by centrifugation (Avanti J-E Centrifuge, Beckman Coulter). Size distribution (see inset to Figure 3.3, *a*) and

zeta (electrokinetic) potential of NDs was estimated at a temperature of 25°C by the dynamic light scattering technique, using a Malvern Zetasizer Nano ZS particle size analyzer. We prepared three aqueous suspensions containing ND clusters with an average size of 50, 110 and 320 nm (see Table 3.1). The polydispersity index (PDI), an indicator of the "broadness" of the particle size distribution of the prepared samples is given in Table 3.1. All three suspensions possess a high colloidal stability. For example, 3 wt. % suspensions with an average ND cluster size of 50 nm have not developed sediment even after 3 years. High colloidal stability of the obtained aqueous ND suspensions also confirmed by the measurements of zeta potential [79], which is in all obtained *1-3* samples is above 30 mV. This indicates that the repulsion between adjacent ND clusters in suspension is strong enough to resist aggregation.

Table 3.1. *Average particle size, zeta potential and polydispersity index of ND samples.*

Samples	*1*	*2*	*3*
Average particle size, nm	320	110	50
Zeta potential, mV	-33.9	-48.2	-49.1
Polydispersity index (PDI)	0.15	0.28	0.22

The main distinctive feature of the obtained ND suspensions is that the ND clusters did not change their properties upon drying, i.e. they can be re-used to make a stable suspension again if necessary [37]. Such a property promises that high power laser action does not lead to the formation and precipitation of ND aggregates.

## 3.2 TECHNIQUES FOR MEASUREMENTS OF NONLINEAR OPTICAL PROPERTIES

Development of optical limiters requires a transparent media that have a strong and fast nonlinearity. Search for such a media relies on the measurement of the nonlinear refractive index and the nonlinear absorption coefficient. Z-scan technique is widely

recognized as one of the most reliable methods to obtain the nonlinear refractive index and the nonlinear absorption coefficient of condensed media [4]. In this section, we demonstrate how both of these parameters can be obtained using Z-scan technique. We also discuss how the Z-scan measurement system can be modified in order to study also the nonlinear light scattering. The nonlinear transmittance measurement technique with a smoothly controlling the incident light intensity is also described.

3.2.1 Z-scan technique

Simplicity and low cost have made Z-scan technique the standard one for the measurements of the nonlinear refractive index n_2 and nonlinear absorption coefficient β [4]. In most cases, n_2 and β can be obtained directly from the Z-scan data. However, it is worth noting that a single Z-scan experiment does not allow one to separate contributions of different mechanisms of the optical nonlinearity to n_2 and β. However, this task can be solved by performing several measurements with different laser sources and detection techniques.

The main advantage of Z-scan technique is the ability to obtain the nonlinear optical characteristics of the samples by measuring only the optical power in the far field. In addition, the nonlinear refraction and the nonlinear absorption can be separated in a single measurement cycle [80] by using so-called closed- and open-aperture Z-scan configurations, respectively [81]. The standard open-aperture Z-scan, which is used for the nonlinear absorption coefficient measurements, is shown in Fig. 3.4.
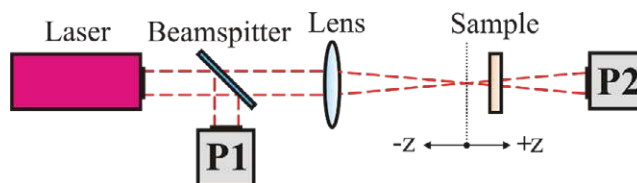

Figure 3.4. *Scheme of a standard open-aperture Z-scan setup in which the transmittance coefficient of the sample (P2/P1) is measured as a function of sample position z. z=0 corresponds to the position of the focal point in the centre of the sample.*

In this setup, the transmittance of the sample through the aperture is measured as a function of the sample position relative to the focal point of the lens, $z = 0$ [4] (see also [82]). The scanning distance depends on the pulse parameters and the sample thickness L. Although in theory, the scanning in the range of $\pm Z_0$, where $Z_0 = \pi w_0^2 / \lambda$ is the Rayleigh length (w_0 is the beam waist radius and λ is the wavelength) is sufficient, for thick samples ($L \leq Z_0$) the range $\geq \pm 5 Z_0$ is preferable [4]. This significantly simplifies the interpretation of the results obtained for the samples with rough surface or when the optical beam imperfections introduce noise into the measurement system. In many practical cases when significant fluctuations of a laser power during a scan occur, a reference detector is introduced in the system (P1 in Fig. 3.4). The position of the aperture in the closed-aperture experiments may vary, however the aperture should be placed between the lens and the detector on the distance from the lens much longer than Z_0. Usually this distance varies from $20 Z_0$ to $100 Z_0$ [4]. In the closed-aperture configuration, the diameter of the aperture should provide the transmittance S of the optical system in the linear regime (i.e. when the sample is placed far from the focal point) in the preferable range of $0.1 < S < 0.5$ [4]. In the open-aperture configuration, i.e. at $S=1$, all incident light passes through the aperture. This makes the method insensitive to any nonlinear distortions of the beam caused by the nonlinear refraction. However Z-scan with $S=1$ is mainly intended for the nonlinear absorption measurements.

3.2.1.1 Nonlinear refractive index in transparent media

The typical result of the closed-aperture Z-scan measurements with a thin sample exhibiting the nonlinear refraction is shown in Fig. 3.5 (solid curve). The valley (peak) followed by the peak (valley) in the normalized transmittance when the sample is scanning from the negative to positive z, is a signature of the self-focusing (self-defocusing) effect, i.e. the positive (negative) light-induced change in the refractive index.
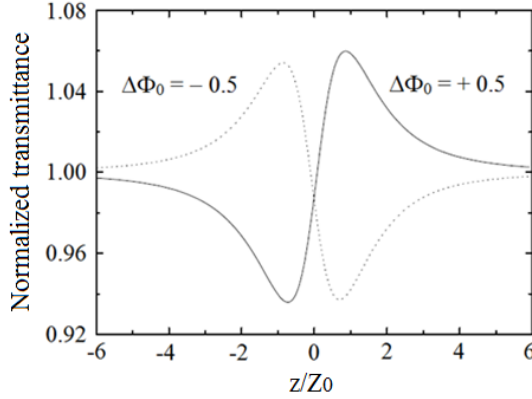
Figure 3.5. The normalized transmittance of the sample with positive (solid curve) and negative (dashed curve) nonlinear refractive index as a function of z divided to the Rayleigh length Z_0. Normalization is performed so that the transmittance of the sample away from the focus where the nonlinearity is not present is equal to 1. Picture has taken with permission of the publisher from [4].

In the closed-aperture Z-scan experiment, the nonlinear refractive index of the medium can be obtained from the difference between the maximum T_p and the minimum T_v of the normalized transmittance, $\Delta T_{pv} = T_p - T_v$. Then for the third-order nonlinear refraction in the absence of the nonlinear absorption, the ΔT_{pv} can be presented in the following form [4]:

$$\Delta T_{pv} = 0{,}406\,(1 - S)^{0.27}\Delta\Phi_0\,, \qquad (3.1)$$

where

$$\Delta\Phi_0 = \frac{2\pi}{\lambda}n_2 I_0 L_{eff}, \qquad (3.2)$$

where $\Delta\Phi_0$ is the on-axis peak nonlinear phase shift with the sample at focus ($z = 0$), n_2 is the third-order nonlinear refractive index, I_0 is the light intensity in the focus, $L_{eff} = [1- \exp(-\alpha_0 L)]/\alpha_0$ is the effective length of the sample, α_0 is the absorption coefficient. The sign of $\Delta\Phi_0$, and consequently, n_2 are determined by the relative position of the maximum and the minimum [4], as it shown in Fig. 3.5.

It is known that in the actual experimental conditions the precise definition of the laser intensity in the focal plane is a challenging task [81]. In this respect, an interesting feature of $T(z)$ dependence obtained from the closed-aperture Z-scan experiments should be mentioned. Specifically, if the nonlinear refraction is caused by the third-order nonlinearity and the sample thickness L is much less that the Z_0, then the distance between the maximum and the minimum of $T(z)$ dependence is given by the following relation [80]:

$$\Delta z \cong 1.7Z_0. \tag{3.3}$$

Therefore, the analyses of the normalized transmittance curve allows one to determine the spatial parameters of the focused beam.

3.2.1.2 Nonlinear absorption coefficient

The nonlinear absorption coefficient β can be determined from the open-aperture Z-scan measurements. For small third-order nonlinear losses, i.e. at $\Delta\alpha L = \beta I L_{eff} \ll 1$ (where $\Delta\alpha$ is the change in absorption coefficient) and the response time much less than the pulse duration, the transmittance as a function of the sample position z is given by the following equation for the Gaussian pulse [4]:

$$T(z) = 1 - \frac{q_0}{2\sqrt{2}} \frac{1}{\left[1 + \frac{z^2}{Z_0^2}\right]}, \tag{3.4}$$

where $q_0 = \beta I_0 L_{eff}$ ($|q_0| \ll 1$). If the response time is much higher than the pulse duration, the factor $2\sqrt{2}$ is replaced by 2 [4]. Thus the open-aperture Z-scan data returns to the nonlinear absorption coefficient β.

3.2.1.3 Simultaneous measurements of the nonlinear refractive index and nonlinear absorption coefficient

The nonlinear absorption coefficient in the presence of the nonlinear refraction can be also determined from the closed-aperture measurements. This can be done by using the following equation for the sample transmittance [83]:

$$T(x) = 1 - \frac{4x}{(x^2+9)(x^2+1)}\Delta\Phi_0 - \frac{2(x^2+3)}{(x^2+9)(x^2+1)}\Delta\Psi_0, \quad (3.5)$$

where $x = z/Z_0$ and $\Delta\Phi_0$ и $\Delta\Psi_0$ are parameters defining the nonlinear phase shift near the focus due to the nonlinear refraction and absorption, respectively:

$$\Delta\Phi_0 = kn_2I_0L_{\text{eff}}, \quad (3.6)$$

$$\Delta\Psi_0 = \frac{1}{2}\beta I_0L_{\text{eff}}. \quad (3.7)$$

By introducing $\varrho = \beta/2kn_2$, Eq. (3.5) can be presented in the following form:

$$T = 1 - \frac{2(\varrho x^2 + 2x + 3\varrho)}{(x^2+9)(x^2+1)}\Delta\Phi_0. \quad (3.8)$$

The best fit of the closed-aperture Z-scan data by the above equation gives ϱ and $\Delta\Phi_0$ allowing one to obtain both nonlinear absorption coefficient β and the nonlinear refractive index n_2.

Equation (3.8) can be also employed to get n_2 and β from the two separate measurements. Specifically, β can be measured in the open-aperture Z-scan experiment (i.e. without aperture). This allows one to obtain $\Delta\Psi_0$ from Eq. (3.7), while measured transmittance in the closed-aperture configuration and Eq. (3.5) give n_2 [84].

Another method to determine n_2 and β in the Z-scan experiment implies measurements with and without aperture, i.e. sequential measurements in the closed- and open-aperture configurations. By dividing the normalized transmittance in the

closed-aperture experiment on the normalized transmittance in the open-aperture one can arrive at value of the nonlinear refraction index. However using of this approach implies that the nonlinear refraction rather than the nonlinear absorption is major mechanism of the nonlinearity [80], while non-zero $\Delta\alpha$ gives an minor additive correction to the transmittance in the closed-aperture configuration. Figure 3.6 shows data obtained in such an experiment [4].
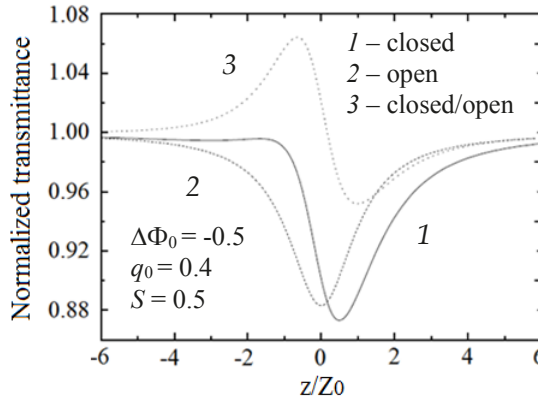
Figure 3.6. *The normalized transmittance measured by a Z-scan with aperture (1), with aperture removed (2) and their ratio (3) as a function of z divided to the Rayleigh length. Picture has taken with permission of publisher from [4].*

3.2.2 Z-scan technique extended to register nonlinear light scattering

Z-scans with different pulse durations, pulse repetition rates, geometries of experiments can be useful in determining the impacts of the nonlinear refraction and the nonlinear absorption in the OL process in a particular medium. However, this experimental parameters variation may be not sufficient in determining the contribution of the nonlinear light scattering in the course of conventional Z-scan measurements. For this purpose Z-scan technique extended to register nonlinear light scattering was developed.

The modified Z-scan allows one to measure simultaneously the incident, transmitted and the scattered light pulses (see

Fig. 3.7). Specifically the signal detector *1* and the cell containing suspension (sample) are mounted directly on the positioning stage *3* so that, in the course of Z-scan measurements, the active area of the sensor is always opposite to the lateral side of the cell.
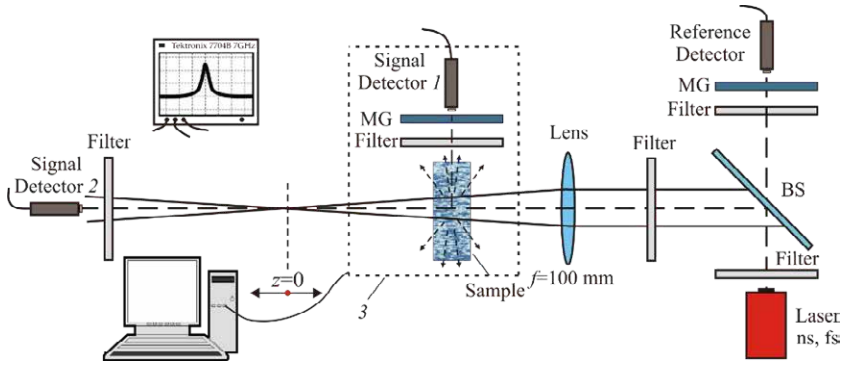
Figure 3.7. Optical scheme of the experimental setup for nonlinear light scattering and pulse temporal profile measurements in the course of Z-scan including laser, reference and signal 1 and 2 detectors, BS (beamsplitter), focusing lens with a focal length of 100 mm, cell with suspension (sample), 3-positional stage, neutral filters, MG (matte glasses, personal computer and digital oscilloscope.

This proposed setup complemented with digital oscilloscope Tektronix 7704B with a bandwidth of 7 GHz significantly simplifies registering of the scattered photons in the course of Z-scan measurements and enables registration the energy and the temporal profile of the incident, transmitted and the scattered laser pulses simultaneously. Such computerized Z-scan approach allowed us to reveal the effect of the nonlinear light scattering on the OL in suspensions of CNT and ND.

3.2.3 Nonlinear transmittance measurement technique

In the optical limiting and nonlinear light scattering experiments it is often important to control the incident light intensity. This is necessary to ensure that the incident light power is below the samples damaging threshold. Besides Z-scan technique, this can be also done by a use of a polarizer and a light polarization

analyzer. Polarizer is a device that is used to produce a polarized light, while analyzer is a device used to study the polarized light.

Let us assume that polarizer and analyzer are set one after another so that their optical axises OA_1 and OA_2, respectively, form an angle α between each other (see Fig. 3.8).
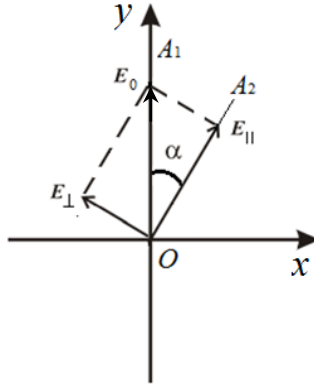
Figure 3.8. *The projection pattern of the electric field vectors.*

Polarizer standing in front of the analyzer will pass light with I_0 intensity with an electric field vector E_0 parallel its axis OA_1. Vector E_0 can be presented as a sum of $E_0 = E_\| + E_\perp$, where $E_\|$ is a vector parallel OA_2 axis, and $E_\perp$ is a vector perpendicular OA_2 axis. The perpendicular component will be blocked by the polarization analyzer. Therefore light with an electric field vector $E \equiv E_\|$ and length of $E = E_0 \cos\alpha$ will pass through the polarizer and analyzer. Its intensity can be presented by the Malus law:

$$I = I_0 \cos^2 \alpha. \tag{3.9}$$

According to Malus law, the change in the angle between polarizer and analyzer leads in changing the light intensity passing through both of them. This method of changing the incident on the sample laser pulse energy is often used in the transmittance measurements under the OL experiments and called nonlinear transmittance measurements.

The nonlinear transmittance measurements along with the Z-scan technique are often used in experiments where changing the incident on a sample light intensity is required. In Z-scan, the intensity is changed due to beam cross section change because of sample moving (scanning) along the focused beam, whilst in the nonlinear transmittance measurements the sample is usually fixed in the beam waist and the laser pulse intensity change results from varying the angle between polarizer and analyzer.

3.3   LASER SOURCES

In the experiments reported here, laser systems with excitation with nanosecond and femtosecond laser pulses were used. The detailed description of the employed laser systems is presented below.

3.3.1 Nanosecond   Nd³⁺: YAG   pulsed   laser   for   OL measurements in visible and near-infrared spectral regions

For the OL and the nonlinear light scattering study in the visible and near-infrared spectral ranges single-frequency Nd^{3+}: YAG laser with passive Q-switching by a $LiF(F_2^-)$ crystal with frequency converter on a KTP crystal was employed [85]. The laser used is a simple and efficient source of a single-mode laser radiation based on the active element of the YAG: Nd^{3+} - crystal with possibility of a smooth change of the energy generation. The optical scheme of the employed laser is presented in Fig. 3.9.

Essentially the laser consists of single mode optical pulse generator and double light amplification on one active element. The laser resonator is limited by the two totally reflecting mirrors *1* and *2* and consists of quarter-wave plate *3*, aperture *4*, birefringent prism (BP) *5*, passive Q-switch *6*, active element *7* and aperture *8* all placed on one optical axis. Quarter-wave plate allows one smoothly change the direction of radiation polarization when beam passes *5-3-1-3-5*. In this case, the BP plays a role of an output laser mirror. At the same time the laser

operating is provided by three resonators formed by BP, mirrors *1* and *2*; mirrors *1* and *2*; BP and mirror *2*. In conjunction with these resonators passive Q-switch is used to provide a single-frequency lasing. Birefringent prism provides spatial separation of "ordinary" I and "extraordinary" II-rays (see Fig. 3.9). Single transverse mode extracting is provided by apertures *4* and *8*, which together with a helium-neon laser *11* serve to align the cavity.
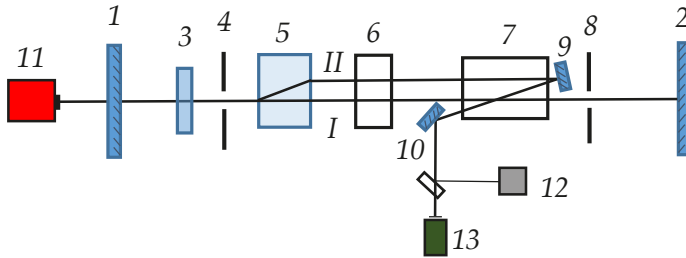
Figure 3.9. *Laser resonator optical scheme with 1,2,9,10 - totally reflecting mirrors, 3 – quarter-wave plate, 4,8 – apertures, 5 - birefringent prism (BP), 6 - passive Q-switch, 7 - active element, 11 – He-Ne laser, 12 – pulse energy meter, 13 – avalanche photodiode.*

The light pulse is formed on the optical axis of the resonator, and its output is carried by an "extraordinary" beam. The output beam sequentially passes passive *Q*-switch *6*, active element *7*, totally reflecting mirror *9*, then again passes through the active element and gets on totally reflecting mirror *10*. So, the output pulse twice passes through an active element achieving multiple gain and increasing the efficiency of the laser [85].

### 3.3.2 Nanosecond parametrical amplifier for OL measurements in near and mid-infrared spectral ranges

In order to study the effects of the nonlinear light scattering in the near- and mid-infrared spectral ranges, we employed the Laser Vision (USA) optical parametrical converter. The system presents an integral, multistage nonlinear device designed for converting radiation produced by Q-switched Nd^{3+}: YAG laser into

frequency tunable infrared radiation. Using an optical parametric oscillator (OPO) and an optical parametric amplifier (OPA) pumped by 532 and 1064 nm, respectively, the system is able to output radiation in the wavelength ranges of 710 - 885 and 1350 – 5000 nm using a set of nonlinear crystals.

The parametric converter uses angle-tuning between the direction of propagation and optical axis of the crystals to achieve phase-matching for the desired conversion process. By rotating the crystals in the extraordinary plane with respect to the incoming beams, the refractive index experienced by light polarized in this plane is changed. The nonlinear crystals rotations are controlled by a personal computer. In both the 532 and 1064 nm stages, crystal pairs of the same length are used and counter-rotated to compensate the beam displacement. The 532 nm OPO stage employs KTP crystals, while the 1064 nm OPA stage because of required transparency in the near- and mid-infrared spectral range employs KTA crystals. A single pair of crystals is used in the OPO stage, whilst OPA consists of four KTA crystals. The optical scheme of the Laser Vision parametric converter is presented in Fig. 3.10. The horizontally polarized pump beam enters the beamsplitter *1* and splits into two beams.
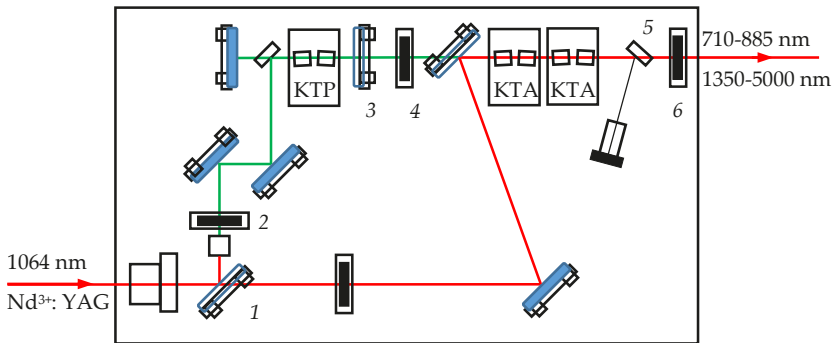
Figure 3.10. Overview of the Laser Vision parametric converter including beamsplitter 1, half-wave plates 2 and 4, reflector 3, dichroic mirror 5, Brewster 'stack of plates' polarizer 6. The parametrical converter is pumped with the fundamental pulse of Nd³⁺: YAG laser and performs an output radiation is the ranges of 710-885 and 1350-5000 nm.

The former enters KTP crystals, whilst the latter passes through the time-delay before combining with the idler of the former on the OPA.The combined beams enter the OPA stage with KTA crystals and produce tunable near- and mid-infrared radiation.

The half-wave plate *2* before the harmonic generator (placed between *1* and *2*) allows smoothly control the 532 nm intensity and therefore the efficiency of the conversion. The reflector *3* passes the 532 nm light on the OPA stage, while reflects the residual the 1064 nm light. Variation by the half-wave plate *4* the polarization plane of the visible light allows keep rotation the KTA crystals in the horizontal plane, which in turn allows save the reflection from KTA crystals surfaces within admissible. Following the 1064 nm OPA is dichroic mirror *5* for removing the residual 1064 nm pump from the co-propagating signal and idler waves. A separate Brewster 'stack of plates' polarizer *6* is intended for isolating either the vertically polarized idler or the horizontally signal wave from the combined output.

Table 3.2. Parametric amplifier specifications

Parameter	Value	Comment
Tuning range	710÷885 nm, 1.35÷5.0 μm	tuning by set of nonlinear crystals
Pump	550 mJ at 1064 nm	horizontally polarized
Pulse energy	12 mJ	1.5÷3.5 μm
	4 mJ	4.0 μm
	0.5 mJ	4.9 μm
Pulse repetition rate	1÷10 Hz	tuning

Table 3.3. Parametric amplifier specifications

Spectral range	Crystal sets	
	Stage №1	Stage №2
710÷885 nm	532 KTP	–
1350÷5000 nm	532 KTP	1064 KTA

Table 3.2 summarizes the parameters of the optical parametric amplifier. Table 3.2 shows that the pulse repetition rate can be set in the range of $1 \div 10$ Hz and the output light wavelength can be varied in the ranges of $710 \div 885$ nm and $1.35 \div 5.0$ micron. This variation is provided by three pairs of crystals: one pair on 532 nm and two pairs on 1064 nm stage. Table 3.3 shows the spectral ranges obtained by controlling particular crystals pairs.

3.3.3 Femtosecond Ti: Sapphire pulsed laser for nonlinear absorption measurements in visible and near-infrared spectral regions

In addition to the nanosecond domain, the nonlinear optical response of the ND suspensions was examined under the femtosecond laser excitation.

The femtosecond laser pulses were produced by Quantronix Integra-C laser system (Excel Technology Inc, Germany). Integra-C is a Ti: Sapphire laser system with a fiber oscillator, an amplifier and pump laser integrated into a single box. This system is suitable to amplify the pulse energy of sub-nJ pulse generated by an oscillator to a level of a few mJ using the chirped pulse amplification technique [86] (see Fig. 3.11).
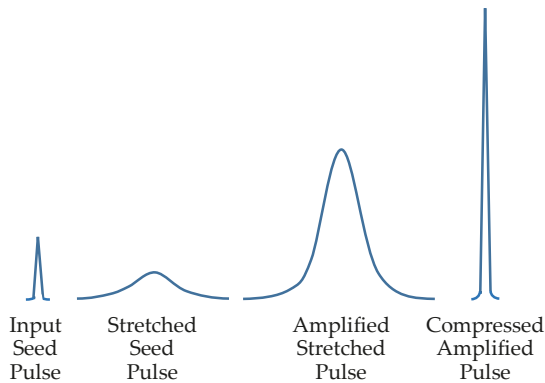
Figure 3.11. The principle of the chirped pulse amplification technique.

In this technique, a generated by mode-locked laser broadband pulse is stretched thus significantly reducing its intensity. The obtained low intensity pulse is then can be amplified because it cannot damage the optical system. Following amplification, the pulse is recompressed to near its original duration about 120 fs thus dramatically increasing its peak power.

As an oscillator, Integra-C employs Quantronix Q-Light ultrafast fiber oscillator with built-in pump laser. The laser is passively mode-locked by a saturable absorber and the gain medium of the laser is the high-gain Er-doped fiber. The Q-Light delivers 200 fs pulses at 1580 nm with more than 5 mW output or 80 mW with amplification. The frequency-doubling of the Q-Light generates sub-100 fs pulse with more than 10 mW output. As a pump laser, Integra-C employs Darwin diode-pumped, Q-switched second harmonic Nd: YLF laser that employ Nd: YLF crystal as the laser gain medium. This laser have more energy per pulse than Nd: YAG laser and exhibit better amplitude and beam pointing stability due to the YLF's much weaker thermal focusing properties.

Integra-C produce femtosecond laser pulses with the central wavelength of 795±10 nm and operate at the repetition rate of 1 kHz.

3.3.4 Femtosecond parametrical amplifier for nonlinear absorption measurements in infrared spectral range

The nonlinear optical measurements in the infrared spectrum range were performed with operating CDP 2017 (CDP systems, Russia) optical parametrical amplifier (OPA) pumped with fundamental pulse of Ti: Sapphire laser.

In the employed OPA system, the parametrical amplification is achieved in BBO (beta barium borate) crystal when spectrally selected part of femtosecond white light continuum is used as a seed pulse. Parametric amplification is realized using one nonlinear crystal and two - pass geometry presented in Fig. 3.12. White light continuum is generated by focusing of small fraction of pumping 800 nm beam into a sapphire plate (SP, see Fig. 3.12).

Continuum is collimated into BBO nonlinear crystal (BBO, see Fig. 3.12) in collinear geometry with the first pass (M9-M10-M11-M14) of the pumping beam. Assuming that the optical delay between pump and seed pulses is properly adjusted (M3-M4 stage), parametric amplification will take place for the wavelength components that satisfy phase matching condition for angle tuned nonlinear crystal.

To form the second amplifier stage, parametric radiation from the first amplifier stage is reflected back into the nonlinear crystal in a collinear manner with the second pass (M12-M13-M14-M11) of the pump radiation. A second delay line placed in M6 stage achieves time matching between the second pass pump and parametric signal (signal and idler waves).
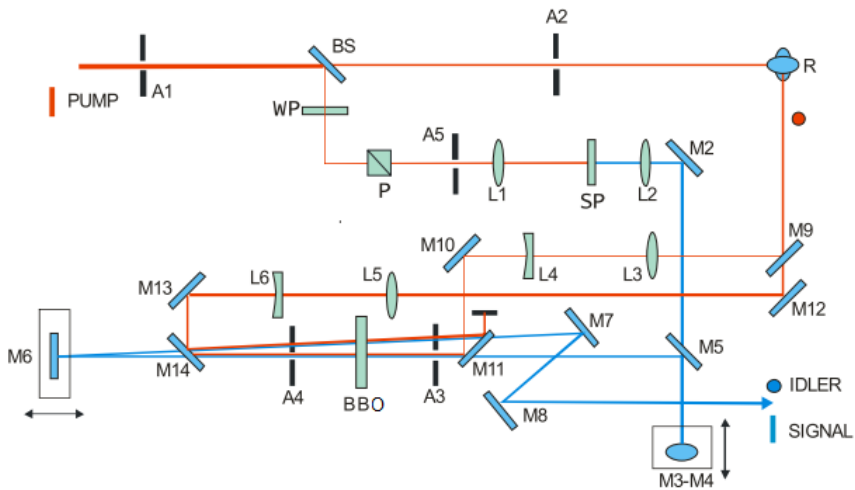
Figure 3.12. Overview of the CDP 2017 femtosecond optical parametrical amplifier.

Wavelengths of the signal and idler waves are tuned by rotating BBO crystal and adjusting both delay lines to optimize the output power. The employed OPA system provides femtosecond laser pulses continuously tunable in 1100-2500 nm spectral range.

4 Nanosecond nonlinear light scattering in aqueous multiwalled carbon nanotube suspensions

This Chapter presents the results on the nanosecond nonlinear light scattering and optical limiting in aqueous suspensions of multiwalled carbon nanotubes. The influence of the nonlinear refraction, the nonlinear absorption and the nonlinear scattering on the OL performance is analyzed. The effects of the nonlinear light scattering on the pulse temporal profile of the transmitted pulse are described. The dependence of the scattered pulses energy on the incident light intensity is presented. The application of the nonlinear light scattering in nanocarbon suspensions for adjustment of laser pulse duration is showed.

4.1 NONLINEAR LIGHT SCATTERING IN AQUEOUS CNT SUSPENSIONS

Despite a large number of reports on the OL in suspensions of nanocarbon materials, very few experiments aimed at correlation between the reduction on the transmittance and the increase of the scattering cross section. In addition, to the best of our knowledge, there are no experimental data on the amplitude and the temporal profile of the nonlinear scattered light pulses

in the course of the OL measurements. In this section, we present the results of the nonlinear light scattering study in aqueous CNT suspensions.

In the experiments, we studied suspensions of multiwalled carbon nanotubes prepared as described in 3.1.1. Most of the particles were 15-20 nm in diameter and 200 nm in length.

In the nonlinear light scattering measurements, we employed Q-switched Nd^{3+}: YAG laser operating at the repetition rate of 1 Hz with laser pulse duration of 18 ns. The experiments were performed at the wavelength of 1064 nm. The incident laser beam was focused into the edge of the cell with CNT suspension by a lens with a focal length of 100 mm. Measured by the scanning-knife edge method (see e.g., [87]) the diameter of the beam waist was $2w_0 = 100$ μm. The initial transmittance coefficient of the cell containing CNT suspension at the wavelength of 1064 nm was 45 %. The measurements were performed with the incident laser pulse energy of $E_{in} = 0.3$ mJ using Z-scan setup discussed in 3.2.2 section.

Figure 4.1 presents the measured transmittance T and the energy of the scattered light pulses E_s as functions of sample position z. $z = 0$ corresponds to the position the focal point at the center of the cell. One can see from Fig. 4.1 that when z approaches to zero the transmittance of the suspension T is remarkably decreases (Fig. 4.1, a). At the same time, the energy of the scattered pulses E_s increases. This implies that the higher the energy of the scattered pulses, the lower the transmittance. At low input intensity ($|z| > 15$ mm), the energy of the scattered pulses does not depend on z and does not vanishing, remaining roughly constant. This value originates from the linear scattering in the suspension that depends on the nanoparticle size and concentration.

It is clear from Fig. 4.1 that in CNT suspension, the nonlinear scattering strongly contributes the OL. The absence of distinct peaks in the transmittance curve (see Fig. 4.1, a), as well as its relative symmetric with respect to the focal point $z = 0$, gives an indication of a minor contribution of the nonlinear refraction to OL.

It is of interest to analyze the contribution of another nonlinear mechanism that causes in decrease in the transmittance, namely the nonlinear absorption.
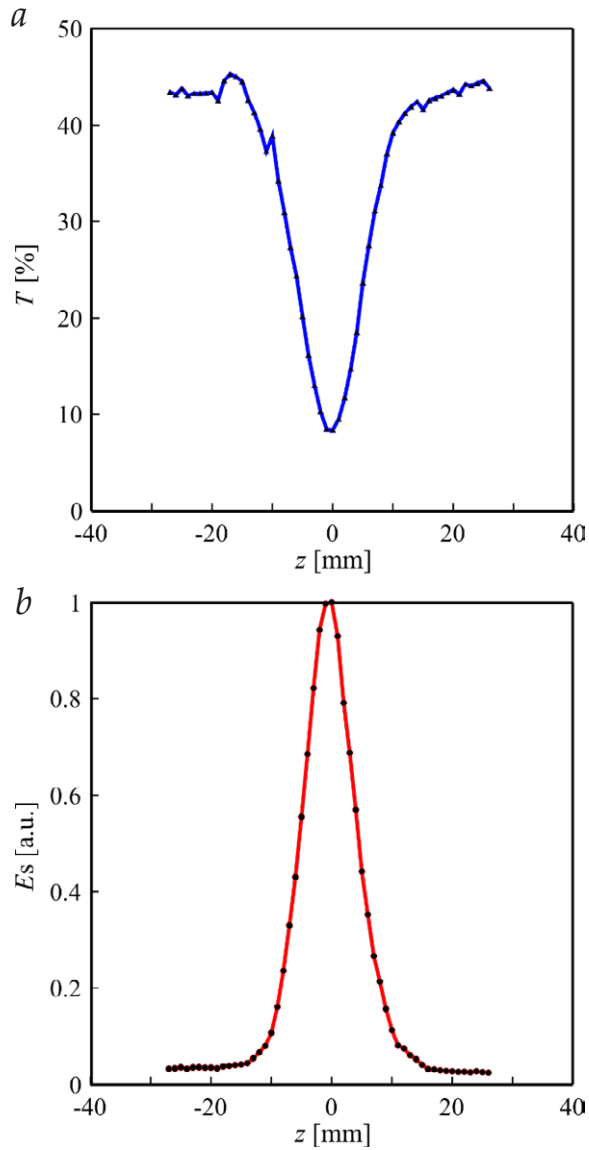
Figure 4.1. *Optical transmittance T and the energy of 90 degree scattered light pulses Es measured as a function of z in the course of Z-scan measurements. z=0 corresponds to the position the focal point at the centre of the cell. Measurements were performed at the incident pulse energy of 0.3 mJ.*

From the experimental data presented in Fig. 4.1, one can construct the $T (Es)$ dependence. For this purpose beforehand, one should subtract an average value of the linear scattering from all the values of the $Es (z)$ dependence. Dependence is shown as black dots in Fig. 4.2. Lines *1* and *2* represent linear and quadratic fitting of the data, respectively. The linear fitting is poorly represents the experimental data, whilst the quadratic relation provides a good approximation.
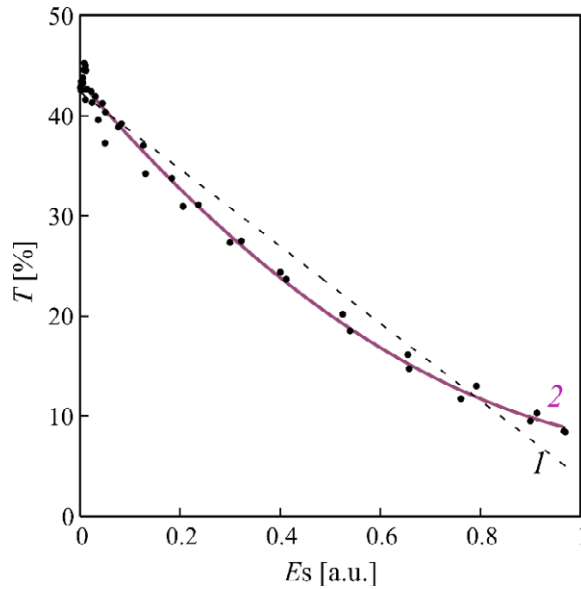
Figure 4.2. *Transmittance T of the multiwalled carbon nanotube suspension as a function of 90 degree scattered pulse energy Es. The data points are derived from the experimental data in Figure 4.1. Curves 1 and 2 represents the result of fitting with linear and quadratic equations, respectively.*

Thus one may conclude that the reduction of the intensity of the transmitted light is not only due to the nonlinear light scattering, but also due to the nonlinear absorption. The nonlinear absorption contribution in the OL process can be analyzed using the data presented in Fig. 4.1. These data one can represent in the form of $T (I)$ and $Es (I)$, where $I (z)$ is the intensity of incident light pulses which is given by:

$$I(z) = E_{in}/\tau S(z). \hspace{3cm} (4.1)$$

Here E_{in} is the incident laser pulse energy and τ is the laser pulse duration. S is the cross section of the Gaussian laser beam when sample is shifted at distance z from the focal point and given by:

$$S(z) = \pi w_0^2 \left[1 + \left(\frac{\lambda z}{\pi w_0^2} \right)^2 \right], \hspace{2cm} (4.2)$$

where w_0 is the beam waist radius.

By taking into account the energy balance, we found that the nonlinear absorption contribution to the OL is about 10%.

4.2 EFFECTS OF NONLINEAR LIGHT SCATTERING ON THE PULSE TEMPORAL PROFILE IN CNT SUSPENSIONS

As the nonlinear light scattering have been found significantly dominating in the OL process in CNT suspensions, it is of interest to analyze its effect on the pulse temporal profile. Figure 4.3 shows the experimentally measured shapes of the incident, transmitted and 90 degree scattered light pulses for various values of z at the incident pulse energy of 1.5 mJ. Curve *1* in Fig. 4.3 represents a laser pulse transmitted through the suspension in the absence of OL. For convenience of the time delay representation, the pulses in Fig. 4.3, *b* are normalized. By comparing the data in Figs. 4.1, *a* and 4.3, *a* one conclude that the reduction of the transmittance T with decreasing $|z|$ is arises from the reduction in the relative width of the transmitted (leading) part of the laser pulse. The smaller the $|z|$, the narrower the part of the pulse passes through the suspension. Obviously, the rest (trailing part) of the pulse is either scattered or absorbed in the suspension. Therefore, the transmitted pulse peak passes ahead the incident pulse peak and the time delay $\Delta t_{in\text{-}out}$ between them increases as the cell approaches the beam waist (Fig. 4.4).
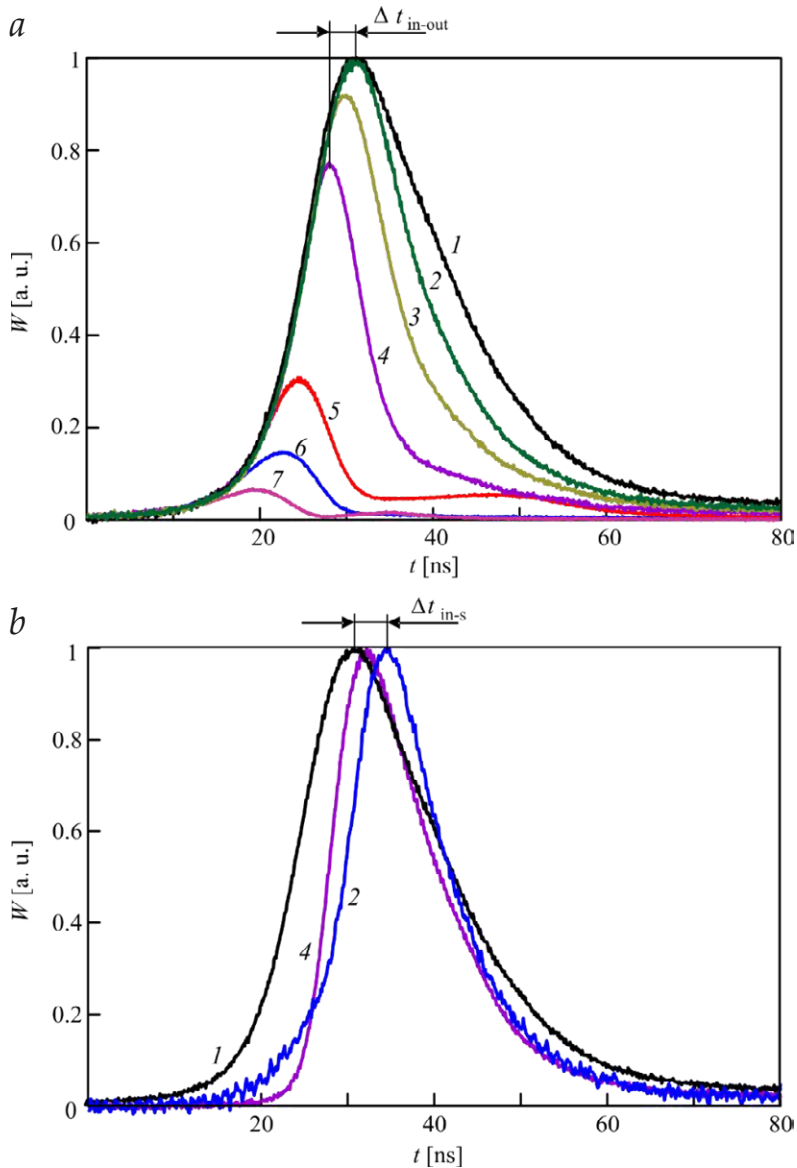
Figure 4.3. *Shapes of the transmitted (a) and scattered (b) light pulses at the incident pulse energy of 1.5 mJ for the cell position z=32 (2), z=24 (3), z=17 (4), z=7 (5), z=4 (6) and z=0 mm (7); 1 represents the incident laser pulse shape.*

It should be noted that the full width at half maximum (FWHM) of the transmitted laser pulse varies with *z* (Fig. 4.5, inset, curve *1*) and has a maximum when *z* = 0. The reduction in

τ_{hw}^{out} initiates from the cutting off the trailing part of the pulse (Fig. 4.5). In addition, the rise time (10%-90%) τ_{rise}^{out} of the transmitted pulse varies little (Figure 4.5, curve 2 in inset) with a slight dip around the focal point.
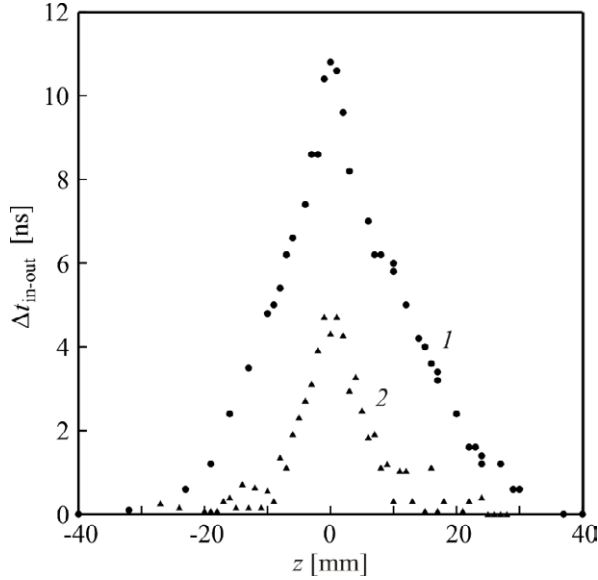

Figure 4.4. *Time-delay between the incident and transmitted pulse peaks as a function of z at incident pulse energies of 1.5 mJ (1), and 0.3 mJ (2).*

Comparison of the transmitted pulse shapes near the beam waist at the energies of 0.3 mJ (Fig. 4.5) and 1.5 mJ (Fig. 4.3, *a*) shows that at the energy of 1.5 mJ, the trailing part of the transmitted pulse has a pedestal with a poorly defined second peak (Fig. 4.3, *a* curves 5-7), while at the energy of 0.3 mJ there is no any pedestal (Fig. 4.5, *a* curves 2-7). This can be relevant to the relaxation processes that may occur in the focal volume where the high power laser beam interacts with the suspension.

The experimental data in Fig. 4.3, *b* obtained at the incident pulse energy of 1.5 mJ demonstrates that the scattered pulse shape differs from the transmitted pulse. When the cell with suspension is away from the beam waist, e.g. at $z = 32$ mm, the peak of the 90 degree scattered pulse with a 13 ns duration delays the incident peak by $\Delta t_{in-s} = 3.2$ ns (Fig. 4.3, *b*, curve 2). For the

incident pulse duration of 18 ns (Fig. 4.3, *b*, curve *1*) such a delay is quite significant. Therefore, the scattered light pulses resulting in OL in studied suspension have shorter pulse duration and delays from the incident pulse. Consequently, the appearance and the raising of the scattered pulse occurs with a time delay from the incident pulse confirming the thermally induced nonlinear scattering mechanism.
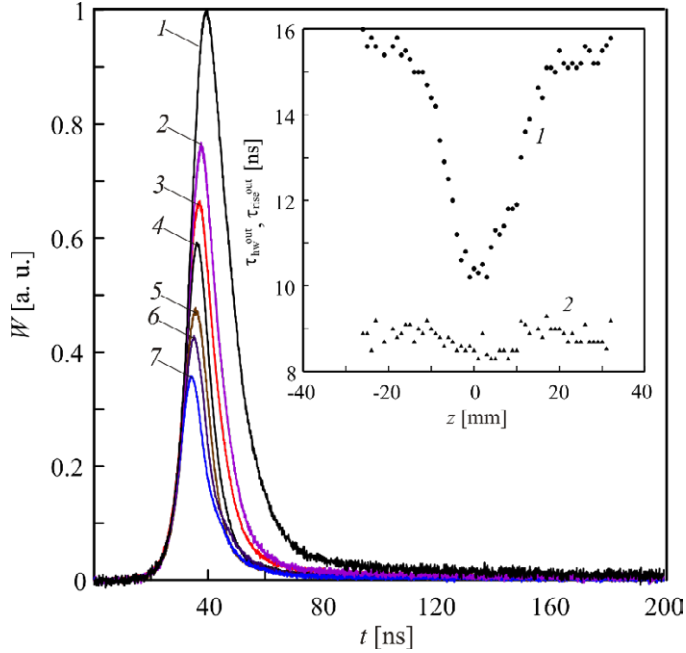
Figure 4.5. Shape of the incident 1 and the transmitted 2-7 laser pulses; z=6 (2), z=5 (3), z=4 (4), z=2 (5), z=1 (6) and z=0 mm (7). The inset shows the duration 1 and the rise time 2 of the transmitted laser pulses as functions of z at the incident pulse energy of 0.3 mJ.

4.3 DEPENDENCE OF SCATTERED LIGHT PULSE ON THE INCIDENT INTENSITY

Figure 4.6 represents the amplitude A, rise time τ_{rise}^{S} (10-90%), fall time τ_{fall}^{S} (90-10%), pulse duration τ_{HW}^{S}, and delay time Δt_{in-s} as functions of sample position z for the 90 degree scattered pulse. The temporal profile of the scattered pulse was measured at the

incident pulse energy of 1.5 mJ. As clearly seen from the figure at the focal point where the intensity of the incident light pulses is maximum the amplitude of the scattered light pulses A is also maximum (Fig. 4.6, curve 1). With decreasing the incident light intensity, i.e. increasing $|z|$, the amplitude of the scattered light pulses drops sharply as one can see from curve 1 in Fig. 4.6.
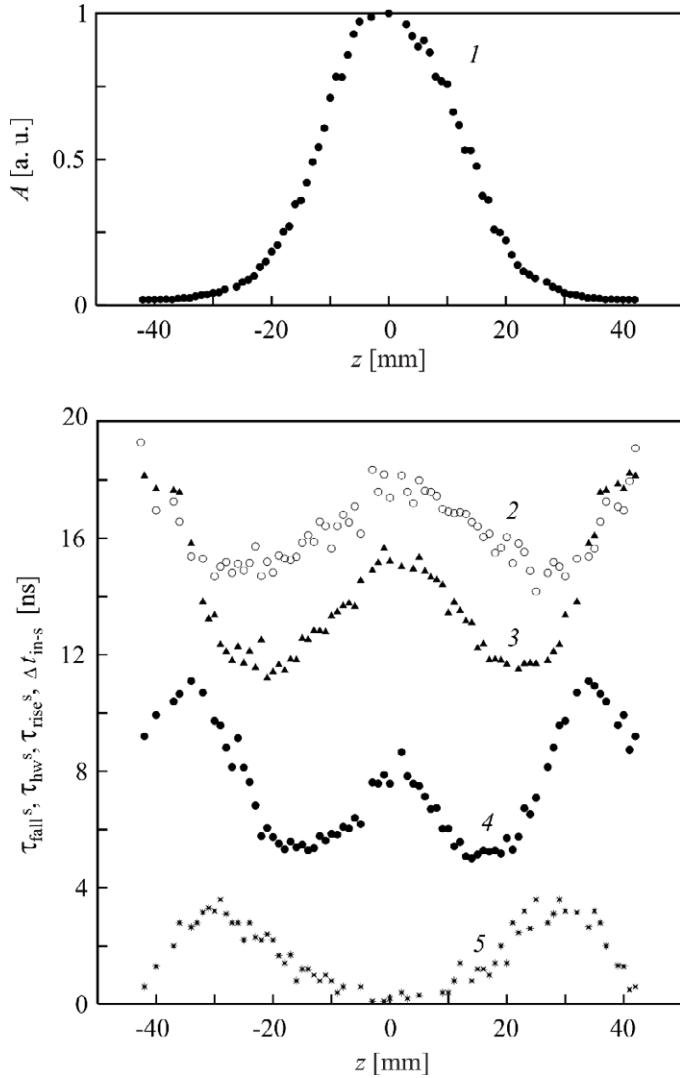
Figure 4.6. The amplitude A (1), fall time τ^S_{fall} (2), pulse duration τ^S_{HW} (3), rise time τ^S_{rise} (4), and the time delay of the scattered pulse relative to the incident pulse peak $\Delta t_{in\text{-}s}$ (5) as functions of sample position z. The measurements were performed at the incident pulse energy of 1.5 mJ.

All this well correlates with the data of the transmittance variation in CNT suspensions with z obtained in this study (see e.g. Fig. 4.3, *a*), and earlier (see e.g. [82]). Specifically this data demonstrate that if the studied suspension exhibits OL behavior, its transmittance drops significantly, as z approaches zero. Therefore, such significant transmittance decrease can be interpreted by a considerable increase of the incident laser pulse power conversion efficiency to the pulse power scattered in all directions including right angle to the z-axis.

It also follows from Fig. 4.6 that the pulse duration τ_{HW}^{S} *(3)*, rise time τ_{rise}^{S} *(4)*, and fall time τ_{fall}^{S} *(2)* of the scattered pulse depend significantly on z with a maximum at $z = 0$. The increasing the magnitude of z, or reducing the incident pulse intensity results in gradually reducing the τ_{HW}^{S} to a minimum $z_{opt} \sim \pm 23$ mm. At the same time curve *1* in Fig. 4.6 shows that at $z = z_{opt}$, the scattered pulse amplitude about 10 times lower than that at $z = 0$. With further increasing $|z|$ the scattered pulse duration τ_{hw}^{s} increases achieving the incident pulse duration. The rise time and fall time curves also show essentially nonmonotonous behavior.

It is also interesting to analyze the variation of Δt_{in-s} with z (Fig. 4.6, curve *5*). Near $z = 0$ there is no time delay between the incident and the scattered pulses. With increasing $|z|$, Δt_{in-s} gradually increases and this increase as one can see from Fig. 4.6 is accompanied by a decrease in the scattered pulse amplitude and duration. At $|z| \sim z_{cr}$ ($z_{cr} > z_{opt}$), the Δt_{in-s} riches a maximum before gradually falling to zero. Concurrently the amplitude A becomes very small. Obviously, at large $|z|$ where the incident pulse intensity is low and no OL, the scattered pulse shape is determined by linear scattering and coincides with the input pulse shape. Therefore at large $|z|$ the Δt_{in-s} must approach zero and the scattered pulse parameters τ_{rise}^{S}, τ_{fall}^{S} and τ_{HW}^{S} must coincide with those of the incident laser pulse as it observed in the experiment.

Similar measurements were performed at other laser pulse energies. The obtained curves are similar in shape as in Fig. 4.6 but at lower energies the variation in A, τ_{rise}^{S}, τ_{fall}^{S}, τ_{HW}^{S}, and Δt_{in-s} take place in the narrower z ranges, that correlates with the experimental data presented in Fig. 4.4. This confirms that the

scattered pulse temporal profile depends on the incident pulse intensity.
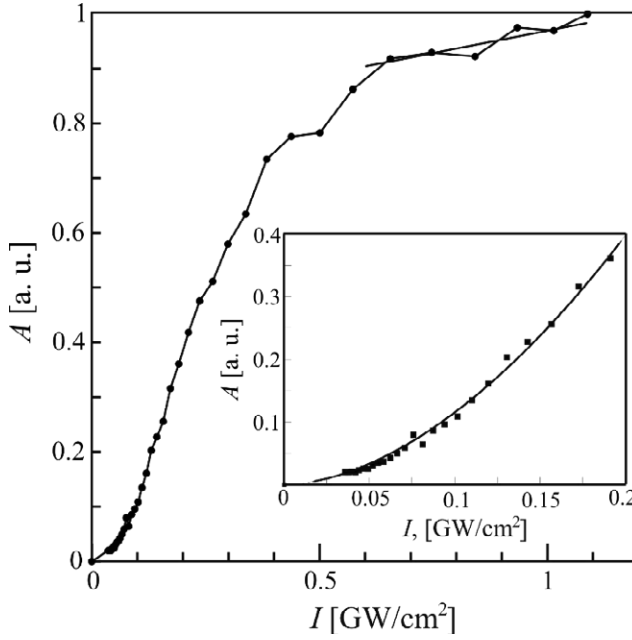
Figure 4.7. *The amplitude A of the scattered light pulses as a function of incident pulse intensity I. Straight-line represents the results of fitting for I > 600 MW/cm². Inset shows quadratic fit for I < 200 MW/cm².*

The experimental data in Fig. 4.6 and the relation for S (z) (4.2) can be used to evaluate the scattered pulse temporal profile dependence on the incident light intensity I presented in Figs. 4.7 and 4.8. As one can see from Fig. 4.7, the scattered pulse amplitude follows a power law at low intensities (see inset, solid curve), whereas remains a linear at high intensities ($I > 0.6$ GW/cm²). Figure 4.8 shows that the scattered pulse parameters τ^S_{fall}, τ^S_{HW}, τ^S_{rise}, and Δt_{in-s} are intricate functions of the incident light intensity. In particular, Fig. 4.8 shows the time delay between the incident and the scattered light pulses Δt_{in-s} is a nonmonotonous function of the intensity I and has a maximum at $I \sim 60$ MW/cm². The scattered pulse duration τ^S_{HW}, presented in Fig. 4.8 is also essentially a nonmonotonous function and has a

pronounced minimum at $I \sim 100$ MW/cm². At this intensity the scattered pulse duration is 1.5 times shorter that the incident one.
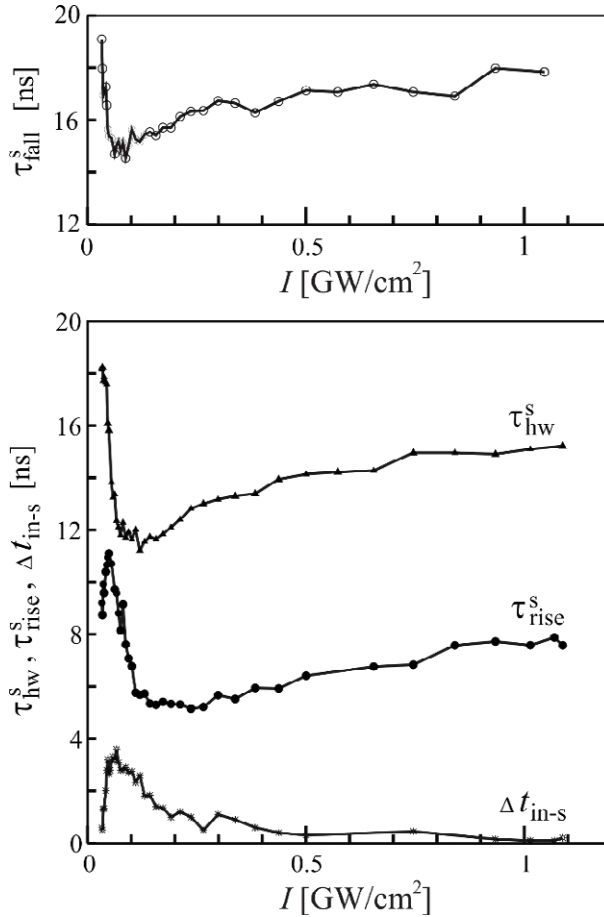
Figure 4.8. Fall time τ_{fall}^s, pulse duration τ_{HW}^s, rise time τ_{rise}^s, and time delay Δt_{in-s} of the 90 degree scattered light pulse as functions of the incident laser pulse intensity I.

The experimentally observed dependence of the pulse duration and the time delay on z, i.e. on the incident light intensity can be explained in terms of the thermally induced nonlinear light scattering. Indeed, in nanosecond domain, the heating and subsequent sublimation of carbon nanoparticles in the beam waist region are essentially immediate, which leads to instantaneous increase of the nonlinear scattering. As a result,

there is no time delay between the peaks of the incident and the scattered pulses and the scattered pulse duration is close to the incident. At the lower intensities, a finite time is needed to heat the carbon nanoparticles up to the evaporation and sublimation temperature. This leads to a time delay and to decrease of the pulse duration as it observed in the experiments. It should be noted that an additional evidence of the thermally induced nonlinear light scattering mechanism, is provided by the intense gas bubbles formation in the focal volume, which was observed in the experiments [26,88].

4.4 APPLICATION OF NONLINEAR LIGHT SCATTERING IN CNT SUSPENSIONS FOR ADJUSTMENT OF LASER PULSE DURATION

The passive Q-switched lasers with nanosecond pulses are often used in the different fields of experimental physics. An adjustment of the pulse duration of such lasers is possible by introduction the additional losses into the laser cavity by the electro-optic switches, the nonlinear absorbers [89] or by variation of a length and configuration of resonators [85]. A shortening of the powerful nanosecond laser pulses can be carried outside of the resonators using a stimulated Brillouin scattering or a stimulated Raman scattering in compressed gases [90,91]. However, the stimulation of these types of scattering in gases can be excited only at high power density and the duration of obtained light pulses are not regulated and is mainly determined by the length of the gas cells.

In section 4.2, we have shown that the nonlinear light scattering on vapor bubbles that are formed due to the transfer of absorbed energy from carbon nanoparticles to surrounding liquid, leads to a shortening of the transmitted laser pulses. In this section we demonstrate the possibility of a smoothly adjustment the duration of nanosecond laser pulses by CNT suspensions.

The experiments were performed with 1064 nm nanosecond laser pulses at a repetition rate of 1 Hz and pulse duration of 16 ns.

The initial transmittance coefficient of the cell with multiwalled CNT suspension at 1064 nm was 45%. The OL was studied using an extended Z-scan setup. The shapes of the incident and the transmitted through the suspension laser pulses were registrated using fast-response photodetectors (SIR5-FC, ThorLabs) with a pulse rise time below 70 ps. A digital Tektronix 7704B oscilloscope measured the photoelectric pulse response. The energy of the incident light pulses was fixed at $E_{in}= 0.3$ mJ. Figure 4.9 shows the shapes of the laser pulses transmitted through the CNT suspension measured for different sample positions z. Curve 4 in the figure corresponds to the shape of the incident laser pulse with a duration of 16 ns at a half maximum linear attenuated by the suspension.
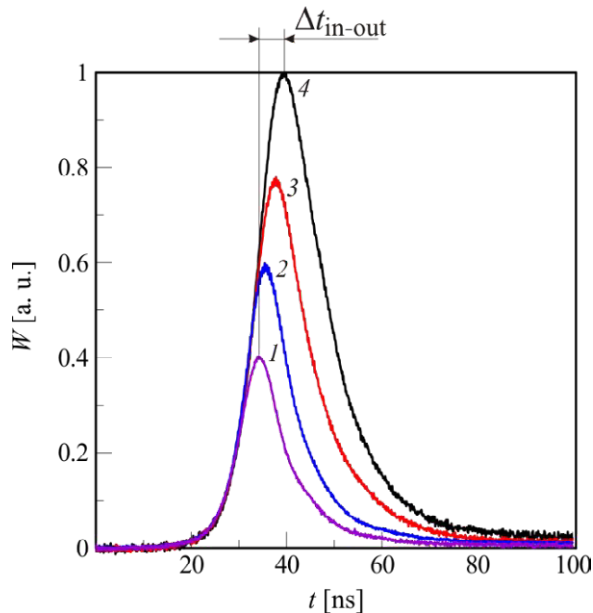
Figure 4.9. *The shapes of the laser pulses transmitted through the CNT suspension in the course of Z-scan measurements for sample positions z = 0 (1), 5 (2) and 11 mm (3). Curve 4 represents the shape of the incident laser pulse. Measurements were performed at the incident pulse energy of 0.3 mJ.*

One can see from the figure that the full width at a half maximum of the transmitted laser pulse depends on z and has a

minimum when the cell approaches the focal point. Such a reduction of the pulse duration is because of the cutting off the trailing part of the pulse as a result of the nonlinear light scattering. Therefore, the peak of the incident pulse is relatively delayed with respect to the transmitted pulse peak, and when the cell approaches the focal point the time delay between them $\Delta t_{\text{in-out}}$ increases (Fig. 4.10).
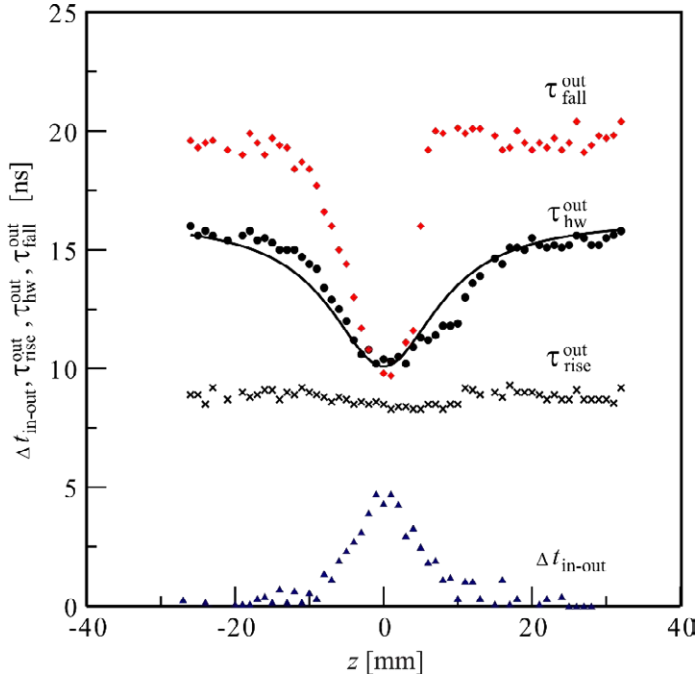
Figure 4.10. *The experimentally measured fall time τ_{fall}^{out}, pulse duration τ_{HW}^{out} (solid curve represents the result of fitting with Eq. (4.4)), rise time τ_{rise}^{out}, and time delay $\Delta t_{\text{in-out}}$ of the transmitted pulse relative to the incident pulse as a function of z.*

According to Fig. 4.10, the minimum duration of the transmitted through the CNT suspension laser pulses is achieved in the beam waist and riches 10 ns. So at $z = 0$, the duration of the transmitted pulses decreases by 1.6 times in comparison with the duration of the incident pulses. Figure 4.10 also represent the rise time τ_{rise}^{out}, and the fall time τ_{fall}^{out} plotted as functions of z. At $|z| \to 0$ the former remains constant, whereas the latter is rapidly

decreases. Nevertheless at $z = 0$, the rise time and the fall time of the laser pulses transmitted through the suspension are approximately equal to each other. Accordingly, the passively Q-switched laser pulses with an extended tail after passing the CNT suspension placed in the focal point become symmetrical with respect to the temporal position of the pulse peak.

It should be noted that the decrease of the pulse duration with a decrease of $|z|$ is accompanied by a corresponding decrease of the amplitude A_{out} of the transmitted light pulses (see Fig. 4.11). This means that the shortening the pulses during the OL in the CNT suspension (in contrast to compression during stimulated Brillouin and stimulated Raman scattering [90,91]) is accompanied by a corresponding decrease in the pulse power.
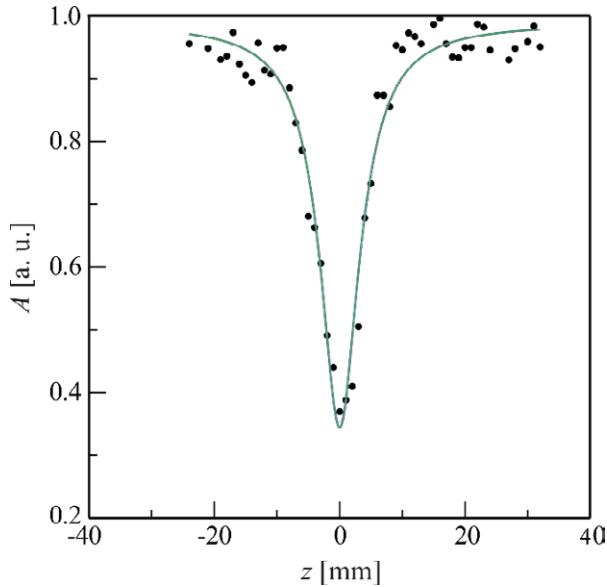
Figure 4.11. *The amplitude A of the transmitted light pulses as a function of sample position z. Dots correspond to the experimental data, whereas solid curve represents the result of fitting with Eq. (4.3).*

It is of importance to find out an analytical equation describing the dependence presented in Fig. 4.11. In the first approximation, an equation describing the transmittance of a nonlinear medium

in the OL measurements with Z-scan (see e.g., [92]) can be applied. In our case, it can be written as follows:

$$A_{\text{out}}(z) = A_{\text{in}} \frac{\ln(1 + \frac{E_{\text{in}}q}{1 + x^2})}{\frac{E_{\text{in}}q}{1 + x^2}}. \tag{4.3}$$

Here A_{in} is the amplitude of the incident light pulses (in rel. units), $x = z/Z_0$, $q = \sigma/(w_0 \times \hbar\omega)$, where σ is the nonlinear scattering cross section, w_0 is the laser beam waist radius, $\hbar$ is Planck's constant, ω is laser radiation circular frequency. The experimental data approximation with Eq. (4.3) (see Fig. 4.11) yields in $A_{\text{in}} = 0.99$, $q = 2$ mJ^{-1}, and $Z_0 = 5.3$ mm. It is clearly seen from the Fig. 4.11, that the described Eq. (4.3) with defined coefficients properly expresses the experimental results.

In order to approximate the experimental data of the transmitted pulse duration presented in Fig. 4.10, the following similar function with three fitting parameters $\tau_{\text{HW}}^{\text{out}}$, q, and Z_0 can be employed:

$$\tau_{\text{hW}}^{\text{out}}(z) = \tau_{\text{hW}}^{\text{in}} \frac{\ln(1 + \frac{E_{\text{in}}q}{1 + x^2})}{\frac{E_{\text{in}}q}{1 + x^2}}. \tag{4.4}$$

The result of the fitting yields in $\tau_{\text{HW}}^{\text{out}} = 16.3$ ns, $q = 1.4$ mJ^{-1}, and $Z_0 = 6.6$ mm. Equation (4.4) with evaluated coefficients can approximately determine the duration of the laser pulses as a function of z for a given pulse energy E_{in}. The fitting of the experimental data obtained for the transmitted pulse duration with the defined Eq. (4.4.), and presented as a solid curve in Fig. 4.10, clearly indicates a good agreement between the experiment and calculations.

CONCLUSIONS OF CHAPTER 4

In conclusion, we observed the OL of the nanosecond laser pulses at 1064 nm in the stable aqueous suspensions of multiwalled CNT. We have found that the reduction of the transmitted laser pulse energy through the CNT suspension is originated from to the nonlinear absorption and an increase of the scattered laser pulse energy. The contribution of the nonlinear absorption on the OL is about 10%, while the contribution of the nonlinear refraction is negligible.

Using Z-scan technique extended to register nonlinear scattered pulses it was experimentally shown that in the OL regime the transmitted pulse peak leads the peak of the incident pulse and the nonlinear light scattering cuts off the trailing part of the pulse. It was demonstrated that at the wavelength of 1064 nm the 90 degree scattered pulse temporal profile (amplitude, pulse duration, rise time, fall time, and time delay) is an intricate function of the incident light intensity because of the transition from the linear scattering at low incident intensities to the thermally induced nonlinear light scattering at high intensities.

The possibility of smoothly controlling the duration of the nanosecond laser pulses with carbon nanotube suspension was experimentally demonstrated. The shortening the duration of *Q*-switched laser pulses with an extended tail is a result of the nonlinear light scattering and is accompanied by the pulse time profile symmetrization.

5 Effects of nonlinear light scattering and saturable absorption in ND suspensions

This chapter presents the results of the nanosecond nonlinear light scattering and femtosecond saturable absorption investigation in aqueous ND suspensions. In the experiment, we aimed at revealing the correlation between the reduction of the transmittance and the enhancement of the light scattering when light intensity increases. We visualize contributions of the nonlinear absorption and the nonlinear refraction to the OL and study how the size and the concentration of the ND clusters and polarization of the light beam influence on the OL efficiency and the nonlinear light scattering. We also demonstrate that for the nanosecond pulses, aqueous ND suspensions can be employed as the high performance nonlinear optical filters for the telecommunication window. In contrary, for the femtosecond light pulses, the ND suspensions can be employed as saturable absorbers.

5.1   NONLINEAR LIGHT SCATTERING IN ND SUSPENSIONS

The nonlinear response of the ND suspensions has been studied much less in comparison with the other nanocarbons. This probably because the loss of the colloidal stability of the ND suspensions is rapidly decreases with heating [39]. However this difficulty can be overcome by modifying the surface of the

detonation ND [37,70]. This achievement in material science allows us to study the OL and the nonlinear light scattering in the ND suspensions. Results of this study are presented in this chapter.

In the experiments, we employed the ND clusters with an average size of 50 nm dispersed in distilled water with mass concentration of 3%. The initial transmission coefficient T_0 of a 1.01 mm thickness sample in a silica cell at the wavelength of 1064 nm was 61% (relative to air).

The nonlinear optical response of the ND suspensions was studied with the nanosecond excitation on the fundamental wavelength of Nd^{3+}: YAG laser, operating at a repetition rate of 1 Hz. The nanosecond OL measurements in the ND suspension were carried out using an open-aperture Z-scan configuration extended to register the energy of the scattered pulses shown in Fig. 3.7. The incident laser pulses were focused into the edge of the sample by a lens with the focal length of 100 mm. The diameter of the beam waist at $1/e^2$ intensity level was 100 μm.

The simultaneously recorded the energy of the incident (E_{in}), transmitted (E_{out}), and the scattered (E_s) light pulses allowed to reveal the effect of the nonlinear light scattering on the transmittance T of the ND suspension. Figure 5.1, *a* shows the experimentally measured T and E_s as functions of sample position z with respect to the focal point for the incident laser pulse energy of 0.7 mJ. It is clearly seen, that with z approaching zero the transmittance drops sharply (Fig. 5.1, *a*, curve *1*), whereas the nonlinear scattering increases (curve *2*), i.e. the stronger the scattering, the lower the transmittance. However, at a distance of about 10 mm a shoulder in the transmittance curve is appears. This local transmittance change is weak and is within the experimental error. This is confirmed by the lack of any shoulders in the same neighborhood in the scattered energy.

Since the nonzero E_s for $|z| < 10$ can be attributed to the contribution of the linear light scattering, we can separate contributions of the linear E_{rs} and nonlinear scattering to the measured energy of the scattered light pulse:

$$E_s = E_{rs} + E_{nls},\qquad\qquad (5.1)$$

where E_{nls} originates from the nonlinear light scattering. One may expect that for a given incident pulse energy, the linear scattering component is z independent, while the dependence of E_{nls} of the sample position in the Z-scan experiment is due to a change in the cross sectional area σz of the laser beam and, accordingly, resulting in the input fluence change $W_z = E_{in}/\sigma z$.
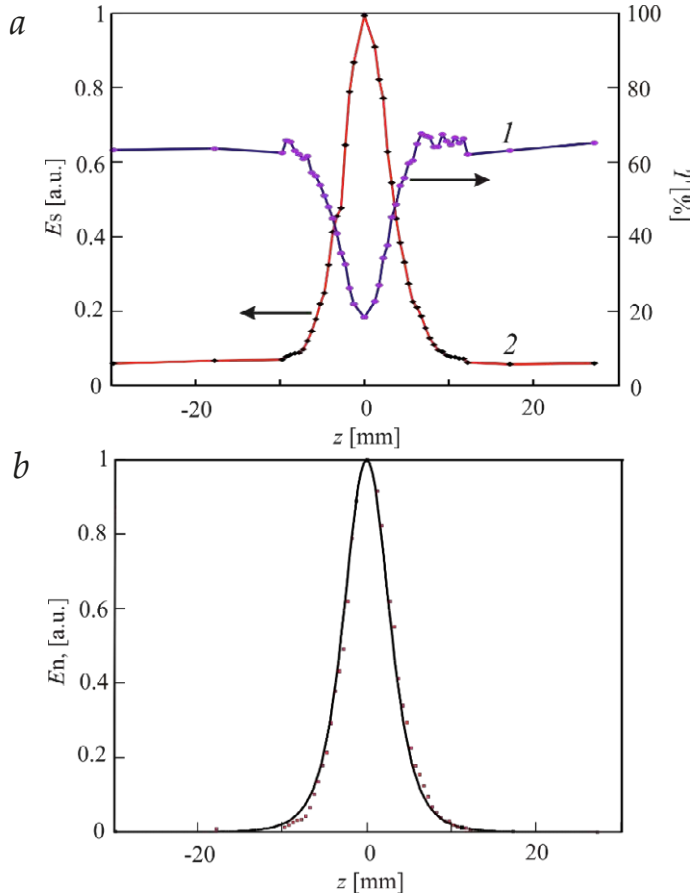
Figure 5.1. (a) Transmittance T of the ND suspension 1, and the energy of scattered at right angle light pulses Es normalized on maximum 2 as functions of sample position z. Red squares in figure (b) represent the experimental data of the energy of the nonlinear scattered light pulse normalized on its maximum at z=0, i.e. $E_n(z) = E_{nls}(z)/E_{nls}^0$ as a function of z. Solid line in (b) represents the results of fitting the experimental data with equation $E_n = \left[1 + \left(\frac{\lambda z}{\pi w_0^2}\right)^2\right]^{-m}$ with fitting parameters $w_0 = 0.045$ mm and $m = 2.87$.

In order to determine the dependence of E_{nls} on W_z from the experimental data (Fig. 5.1, *a*, curve 2), we have plotted the following relationship (Fig. 5.1, *b*, red squares):

$$E_n(z) = E_{nls}(z)/E_{nls}^0, \tag{5.2}$$

where E_{nls}^0 is the energy of radiation pulses scattered at the right angle for the sample position $z = 0$. The obtained experimental data can be approximated with the function that describes the relative laser pulse fluence dependence on the coordinate z in m power (parameter m to be determined). For this reason, we can recall Eq. (4.2), i.e. the equation describing the Gaussian beam radius w as a function of z (see, e.g., [16]):

$$w(z) = w_0 \left[1 + \left(\frac{\lambda z}{\pi w_0^2} \right)^2 \right]^{\frac{1}{2}}, \tag{5.3}$$

where w_0 is the Gaussian beam waist radius. From this formula, we obtain the following relation:

$$\frac{W_z}{W_0} = \frac{\sigma_0}{\sigma_z} = \left[1 + \left(\frac{\lambda z}{\pi w_0^2} \right)^2 \right]^{-1}, \tag{5.4}$$

where σ_0 and W_0 are the beam cross sectional area and the input fluence in the beam waist, respectively. As a result, the fitting function is as follows:

$$E_n = \left[1 + \left(\frac{\lambda z}{\pi w_0^2} \right)^2 \right]^{-m}, \tag{5.5}$$

where w_0 and m are the fitting parameters to be determined. The fitting showed that Eq. (5.5) with fitting parameters $w_0 = 0.045$ mm and $m = 2.87$ well approximate the experimental data presented in Fig. 5.1, *b* (solid curve). Interestingly, that the defined w_0 value coincides with the experimentally measured beam waist radius within an experimental error. Thus, Z-scan

experiments at the fixed input energy and the pulse duration yield the following relations:

$$E_n = \left(\frac{\sigma_0}{\sigma_z}\right)^{2.87} = \left(\frac{W_z}{W_0}\right)^{2.87}. \qquad (5.6)$$

Alternatively, the dependence of E_s on the incident pulse energy E_{in} can be experimentally determined at fixed values of the pulse duration and the laser beam radius. In these experiments, the cell with ND suspension is positioned at the beam waist and the energy of incident laser pulses is varied using calibrated neutral filters. The corresponding experimental dependence is plotted in Fig. 5.2 (black squares).

Recalling Eq. (5.1) and taking into account that E_{rs} is proportional to E_{in}, the experimental data of E_s (E_{in}) presented in Fig. 5.2 (black squares) can be approximated as follows:

$$E_s = k_1 E_{in} + k_2 (E_{in})^l, \qquad (5.7)$$

where k_1, k_2, and l are fitting parameters. It is clearly seen from Fig. 5.2 (solid curve), that Eq. (5.7) with the defined fitting parameters k_1 and k_2 and $l = 2.13$ well describes the experimental data. In the view of this result and considering Eq. (5.6), one can conclude that the following nonlinear law can describe the energy of the scattered at a right angle light pulses:

$$E_s = \alpha E_{in} + \beta \left(\frac{E_{in}}{\sigma}\right)^p, \qquad (5.8)$$

where α is a dimensionless coefficient, β is a coefficient with dimension [cm^2/J], σ is the laser beam cross sectional area, and p is the index of nonlinearity. The average value of p for the given ND suspension that was determined using the two independent approaches described above, corresponds to 2.5. One can assume that the energy of radiation scattered at a solid angle of 4π also obeys a similar law.
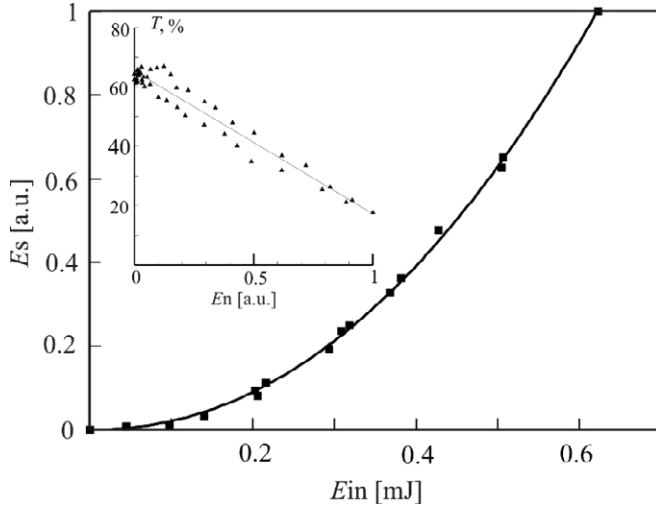
Figure 5.2. *The energy of the scattered light pulses Es normalized on the maximum as a function of the incident pulse energy Ein. Squares represent the experimental data while solid curve presents the result of fitting with equation $E_s = k_1 E_{in} + k_2 (E_{in})^l$, where k_1, k_2, and l are the fitting parameters The inset shows the experimental data (triangles) on the ND transmittance T as a function of the energy of the nonlinear scattered light pulses normalized on its maximum at z=0, i.e. $E_n(z) = E_{nls}(z)/E_{nls}^0$. Solid line in the inset represents the result of fitting with the following equation: $T = T_0 - kE_n$, where k is a fitting parameter.*

It should be noticed that Eq. (5.8) was obtained for the fixed pulse duration (τ=17 ns), therefore one can conclude that replacing E_{in} with the power of the incident pulse would be incorrect. In addition, it should be noticed that the OL and, hence, the nonlinear light scattering in ND suspension (as well as, e.g., in suspensions of carbon black and CNTs) will probably decrease for subnanosecond and picosecond laser pulses [6,13].

It is of interest to analyze the experimental data presented in Fig. 5.1 to elucidate the relationship concerning the nonlinear light scattering and the optical limiting. Let us consider the energy balance for laser pulses at the input and output of the cell in the absence of OL, which can be written as follows:

$$E_{in} = E_{out} + E_{ab} + E_r + E_{rs}^{4\pi}, \tag{5.9}$$

83

where E_{ab}, E_r, and $E_{rs}^{4\pi}$ are the energies absorbed in suspension, reflected from the cell walls, and scattered (Rayleigh scattering) on the ND particles, respectively. Therefore the initial transmission coefficient of the cell with ND suspension can be expressed as follows:

$$T_0 = \frac{E_{in} - E_{ab} - E_r - E_{rs}^{4\pi}}{E_{in}}.$$ (5.10)

Assuming that OL is caused by the nonlinear scattering only, the transmittance coefficient T measured in the course of Z-scan can be written in the following form:

$$T = T_0 - \frac{E_{nls}^{4\pi}}{E_{in}},$$ (5.11)

where $E_{nls}^{4\pi}$ is the pulse energy (dependent on W_z) scattered in a solid angle 4π under the OL conditions. Evidently, the experimentally obtained in arbitrary units the relative energy of the laser pulses scattered at a right angle E_n is directly proportional to $E_{nls}^{4\pi}$. Hence, Eq. (5.11) can be rewritten as follows:

$$T = T_0 - kE_n,$$ (5.12)

where k is a proportional factor.

The inset in Fig. 5.2 presents the experimental dependence of $T(E_n)$ (triangles) obtained from corresponding $T(z)$ and $E_n(z)$ dependences (refer to Fig. 5.1) and a solid line, which represents a linear approximation with Eq. (5.12). The appropriate correlation indicates that the optical limiting in the ND suspension originates from the nonlinear light scattering.

5.2 SIZE EFFECT ON THE OPTICAL LIMITING THRESHOLD IN ND SUSPENSIONS

In order to investigate the dependence of the OL threshold on the size of the ND clusters, we studied the OL in 0.03 wt. % aqueous ND suspensions with the average cluster size of 50, 110 and 320 nm, which will be hereafter referred to as S, M, and L samples. The thickness of all the samples was 1.06 mm. Figure 5.3 shows the wavelength dependence of the optical density of these samples in the spectrum range of 250 - 850 nm. One can observe that the bigger the ND cluster size, the higher the optical density. This is mainly because of stronger scattering from the particles of bigger sizes. At the wavelength of 532 nm, the transmittances of the S, M, and L samples are 0.87, 0.73 and 0.54, respectively.
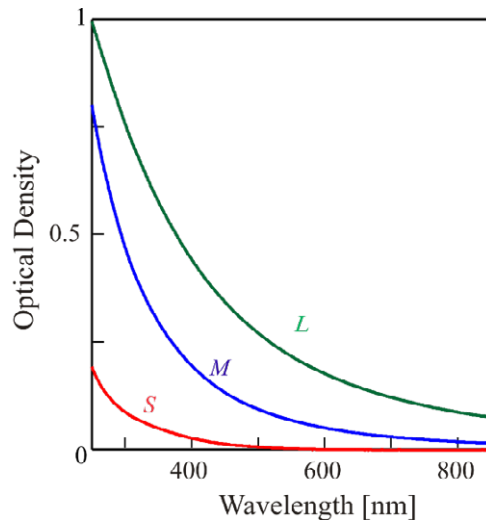
Figure 5.3. Optical density of the ND aqueous suspensions of thickness of 1.01 mm with the average particle size of 320 nm (L), 110 nm (M) and 50 nm (S) as a function of the wavelength. Optical density is measured relative to distilled water.

In the OL experiment (see Fig. 5.4), we employed TEM$_{00}$ mode (M^2=1) of a single-frequency Nd^{3+}:YAG laser with passive Q-switching by an LiF(F$_2^-$) crystal with the frequency converter on the KTP crystal [85]. The pulse duration and the repetition rate

of the 532 nm pulses were 17 ns and 1 Hz, respectively. The vertically polarized laser beam was focused into the edge of the sample by the lens with the focal length of 100 mm. The measured by the scanning knife edge method the diameter of the beam waist was 70±3 µm at $1/e^2$ intensity level. The incident fluence was controlled by rotating the half-wave plate.

The OL in ND suspensions were investigated by the nonlinear transmittance and Z-scan techniques. The energies of the incident, transmitted and the scattered at 90 degree pulses were detected simultaneously by the photodetectors (detectors *A*, *B* and *C*, respectively, in Fig. 5.4). In order to block radiation scattered from interior and exterior walls of the cell two slit-like apertures were used. The first aperture was placed directly on the lateral side of the cell, whilst the second one was at some distance from it. The short focus lens between the detector *C* and the second aperture allowed us to collect light scattered at 90 degree in the focal region. In the Z-scan measurements, the sample and the detector *C* were moved along the beam axis enabling simultaneous measurements of the transmitted and the scattered at 90 degree energy as a function of sample position.
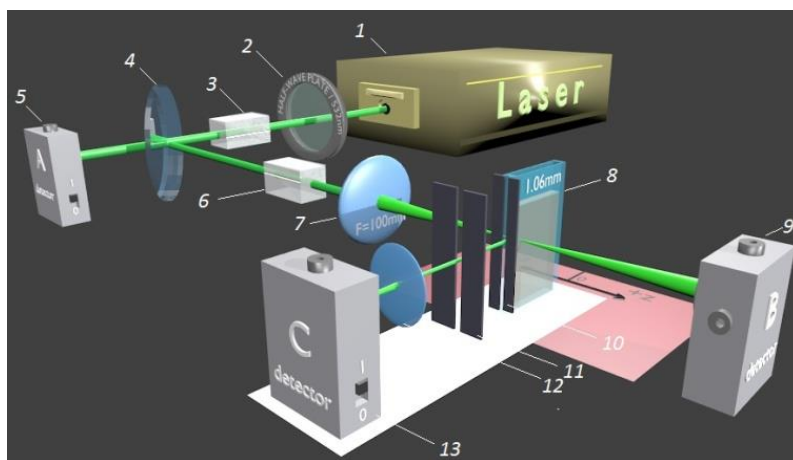
Figure 5.4. *Sketch of the open-aperture Z-scan setup including 1-laser, 2-half-wave plate, 3-Glan-Thompson polarizer, 4-mirror, 5-reference detector A, 6-Glan-Thompson polarizer, 7-focusing lens (F=100mm), 8-sample, 9-signal detector B, 10,11-slit-like apertures, 12-short focusing lens, 13-signal detector C.*

In the nonlinear transmission measurements, we varied the incident fluence by rotating the half-wave plate from 0 to 45° (see Fig. 5.4). Figures 5.5, *a,b* show output fluence (W_{out}) and energy of the scattered pulse (E_s), respectively, as a function of the input fluence (W_{in}) for *L*, *M* and *S* samples. Data for distilled water is shown in Fig. 5.5, *a* for comparison. One can see from Fig. 5.5, *a* that in distilled water, W_{in}/W_{out} = const, while in the ND suspensions, the increasing of W_{in} results in OL, i.e. $W_{out} \rightarrow$ const at $W_{in} \rightarrow \infty$. The dependence of the output fluence (W_{out}) on input fluence (W_{in}) shown in Fig. 5.5, *a* can be approximated by the following function:

$$W_{\text{out}} = T_0 W_t \left[1 - exp\left\{ -\frac{W_{\text{in}}}{W_t} \right\} \right],$$
(5.13)

where T_0 is the linear transmittance. Fitting for the *S*, *M* and *L* samples returns $T_0 = 0.91$, $W_t = 2.57$ J/cm², $T_0 = 0.74$, $W_t = 0.88$ J/cm² and $T_0 = 0.55$, $W_t = 0.68$ J/cm², respectively. The fitting results are presented as solid lines in Fig. 5.5, *a*. It is worth noting that the fitting results well correspond to the measured linear transmittance for the *S*, *M* and *L* samples (0.87, 0.73 and 0.54 at 532 nm, respectively).

Equation (5.13) allows us to calculate the saturation level $W_{out,sat} = T_0 W_t$ of the output fluence for the *S*, *M* and *L* samples as 2.3, 0.7 and 0.3 J/cm², correspondingly. Sample *S*, containing the smaller particles has the highest value of the output saturation fluence.

The OL threshold, which is defined as the input fluence $W_{in,th}$, when the transmittance is halved [4,12,32,33], i.e. $W_{out,th}/W_{in,th} = T_0/2$ returns to 1.1, 1.2 and 4.5 J/cm² for *L*, *M* and *S* samples, respectively. At higher input fluences the transmittance (see inset to Fig. 5.5, *a*) rapidly decreases due to strong optical nonlinearity of the ND suspensions.

It is clear from Fig. 5.5, *a,b* that in all studied samples, the OL at 532 nm is accompanied by the nonlinear light scattering, which may be caused by the formation of microplasma in the focal area [62]. It is worth noting that in contrast to the OL in carbon

black [93] and CNT suspensions [5], we observed no vapor bubbles in our experiments.
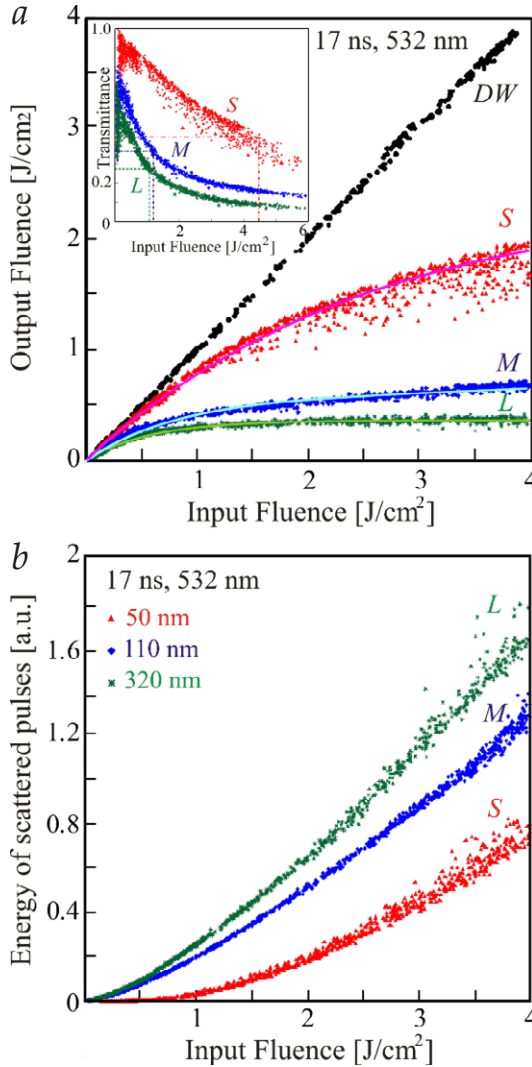
Figure 5.5. *The output fluence (a) and the energy of scattered pulses (b) as functions of input fluence for 320 nm (L), 110 nm (M) and 50 nm (S) samples. Solid lines correspond the result of fitting with Eq. (5.13). The inset in (a) represents the transmittance dependence of the studied ND samples on the input fluence. Black points in (a) show results of the measurements with distilled water. The measurements were performed at the wavelength of 532 nm with 17 ns laser pulses.*

Figure 5.6 shows the energy of normalized scattered pulses as a function of the input fluence (W_{in}) in the linear and logarithmic (inset) scales for the samples with cluster size 110 nm and 320 nm.
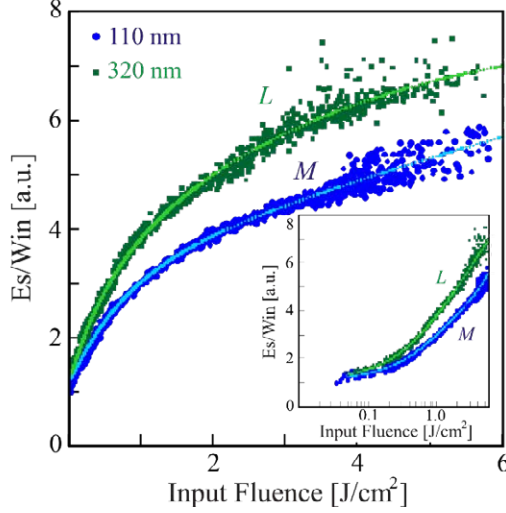
Figure 5.6. *The energy of scattered pulses normalized on input fluence in linear and logarithmetic (inset) scale of abscises axes for L and M samples as a function of the input fluence.*

The experimental data are fitted by the following bi-exponential function:

$$\frac{E_S}{W_{in}} = B\left\{1 + A_{s1}\left[1 - exp\left\{-\frac{W_{in}}{W_{s1}}\right\}\right]\right.$$
$$\left. + A_{s2}\left[1 - exp\left\{-\frac{W_{in}}{W_{s2}}\right\}\right]\right\}, \qquad (5.14, a)$$

where $A_{s1} = 1.95$, $A_{s2} = 11.27$, $W_{s1} = 0.78$ J/cm², $W_{s2} = 22.73$ J/cm², and $A_{s1} = 1.51$, $A_{s2} = 5.19$, $W_{s1} = 0.492$ J/cm², $W_{s2} = 3.33$ J/cm² for M and L samples, respectively. When $W_{in} \to 0$, Eq. (5.14, a) returns to

$$E_s = BW_{in}, \qquad (5.14, b)$$

where B is proportional to the linear scattering cross section at 90°. By comparing results for M and L samples, one can obtain $B_L/B_M = 1.35$, i.e. the bigger the cluster size, the bigger the linear scattering cross section. At high input fluence, $W_{in} \gg W_{S1}, W_{S2}$, the energy of the scattered pulse is also a linear function of W_{in},

$$E_s = B(1 + A_{s1} + A_{s2})W_{in}. \qquad (5.14, c)$$

However nonlinear scattering results in the increase of the slope.

The bi-exponential dependence of the scattering cross section on the input fluence indicates that several mechanisms of the nonlinearity are responsible for the observed effect. The fitting presented in the Figs. 5.5 and 5.6, show that the A_{s1} and W_{s1} show a moderate dependence on the size of the cluster. This experimental finding may indicate that the first mechanism of the nonlinearity is associated with material, rather than the size of the cluster. In contrast, W_{s2} for the M sample is much higher than that for the L sample, i.e. the second mechanism of the nonlinear scattering is more important for the large ND clusters. In our experimental conditions, $W_{in} \ll W_{s2}$ for the M sample. That is for the ND clusters with the size of 110 nm, the first mechanism dominate the nonlinear scattering, while the second mechanism manifests itself only for the ND clusters with the size of 320 nm. Importantly however that at the input fluence range $W_{in} < 6$ J/cm², we did not achieve saturation regime described by Eq. (5.14, c).

In order to reveal the nonlinear refraction contribution to the OL in ND suspensions, we employed the closed-aperture configuration of Z-scan technique. The sample M was placed in the vicinity of the focal point of the lens with the focus distance of 100 mm. The 2.2 mm aperture with transmittance of 30% ($S = 0.3$) was placed between the signal detector B and the focusing lens at the distance of 360 mm (~ 50 Z_0, Z_0 – Rayleigh length) from the beam waist. The measurements were carried out at the laser pulse energy of 30 µJ, i.e. the incident fluence of 0.78 J/cm², that is well below the damage threshold of nanocarbon suspensions in the nanosecond regime [5,94]. The measured

transmittance as a function of the sample position with respect to the focal point is shown in Fig. 5.7, *a*. One can see that when the sample was placed at the focal point ($z = 0$), the normalized transmittance decreases by less than 20%. At $|z| < 20$ mm the transmittance remains an even function of the coordinate z indicating that the nonlinear refraction is negligible [95–97]. It is worth noting that the same result has been obtained for the OL in CNT suspensions [22]. It must be pointed out that at $z > +30$ mm (the sample is closer to the aperture) the transmittance is slightly higher than that at $z < -30$ mm (the sample is closer to the lens) because of the linear scattering in the ND suspension.
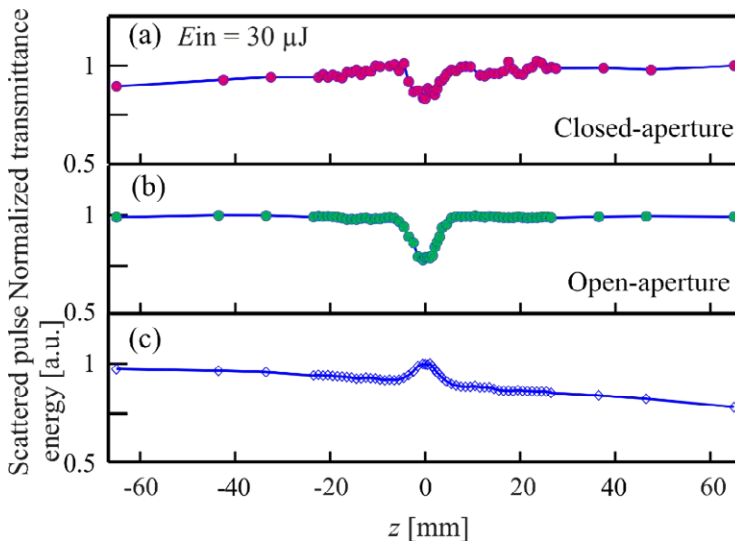
Figure 5.7. *The normalized M sample (110 nm ND clusters) transmittance in the closed- (a) and open-aperture (b) Z – scan experiments, as well as the energy of the scattered pulses (c) as functions of sample position z. Each experimental point was obtained by averaging over 30 laser pulses. The measurements were performed for the 30μJ pulse energy.*

Figures 5.7, *b,c* represent the transmittance (*b*) and the energy of the scattered pulses (*c*) of the *M* sample measured at the same input pulse energy of $E_{in}=30$ μJ in the open-aperture Z-scan experiment. It can be seen that although transmittance dip at $z = 0$

does not exceed 25%, the peak of the nonlinear scattering is also observed indicating that OL originates from the nonlinear scattering.

In order to estimate the contribution of the nonlinear absorption to the OL at high input energy we employed the open-aperture Z-scan configuration at $E_{in} = 160$ µJ. In the experiment, the energies of the transmitted (E_{out}) and scattered at 90° pulses (E_s) were measured simultaneously. The measured transmittance $T(z) = E_{out}/E_{in}$ and relative number of the scattered photons $Q(z) = E_s/E_{in}$ for the M sample are shown in Fig. 5.8 as functions of z. It is clear from Fig. 5.8, a that $T(z)$ has a minimum at $z = 0$, resembling the results of the closed-aperture Z-scan measurements at $E_{in} = 30$ µJ (see Fig. 5.7, a). In the open-aperture arrangement, the transmittance for the M sample is well approximated by the following function:

$$T(z) = T_0 - a \, exp\left[-\frac{1}{2\left(\frac{z}{b}\right)^c}\right],\qquad(5.15)$$

where $T_0 = 0.74$ is the linear transmittance, $a = 0.62$, $b = 4.08$ mm, and $c = 2.41$ are fitting factors (solid line in Fig. 5.8, a).

Both linear and nonlinear scattering influences the transmittance in the Z-scan experiment. However, the relative number of photons coming from the linear Rayleigh and Mie scattering at solid angle 4π does not depend on the incident fluence and, hence, on the sample position z, while the relative number of photons coming from the nonlinear scattering does. That is $Q(z)$ can be presented in the following form:

$$Q(z) = Q_l + Q_n(z),\qquad(5.16)$$

where Q_l and $Q_n(z)$ describes the linear and nonlinear scattering, respectively. $Q_n(z)$ can be obtained by subtracting the z-independent background Q_l from the measured $Q(z)$. It can be seen from Figs. 5.8, a and 5.8, b that in the ND suspensions, both the minimum transmittance and the maximum scattering occur

at $z = 0$, i.e. when the input fluence is maximum. This clearly indicates that the nonlinear scattering essentially influences the OL.
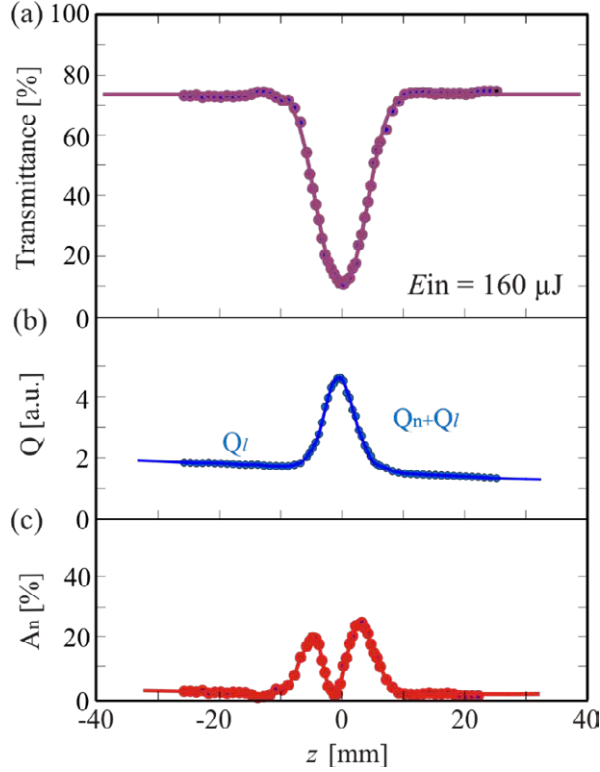
Figure 5.8. (a) The transmittance of the M sample (110 nm ND clusters) as a function of sample position z in the open-aperture Z – scan experiment. Solid line corresponds to fitting with Eq. (5.15) at a = 0.62, b = 4.08 mm, and c = 2.41. (b) The energy of the scattered pulses normalized to the energy of incident pulses Q (z) for the M sample. One can observe that contribution of the nonlinear scattering Qn (z) is maximum at the focal point. (c) Nonlinear absorption An (z) obtained from equation (5.19) at An (0) = 0.

In order to estimate the relative contribution of the nonlinear absorption and the nonlinear scattering one can employ the energy considerations. Specifically, the energy balance in the process of the light-matter interaction can be presented by the following equation:

$$T + A + S + R = 1, \qquad (5.17, a)$$

where T, A, S and R are relative (with respect to the incident pulse) number of photons in transmitted, absorbed, scattered and reflected pulses, respectively. One may expect that the relative number of the scattered in the 4π solid angle photons is proportional to the $Q(z)$:

$$S = k\big(Q_l + Q_n(z)\big), \qquad\qquad (5.17, b)$$

where k is a constant that depends on the geometry of the experiment. The relative number of reflected photons is mainly determined by Fresnel reflection coefficients, while

$$A(z) = A_l + A_n(z), \qquad\qquad (5.17, c)$$

where A_l and $A_n(z)$ are linear and nonlinear absorbance.

Since at $|z| > 10$ mm the nonlinear absorption and nonlinear scattering are negligible, the energy balance Eq. (5.17, a) reduces to the following:

$$T_0 + kQ_l + A_l + R = 1, \qquad\qquad (5.17, d)$$

where $T_0 = 0.74$ is a linear transmittance for the M sample (see Figure 5.17, a). By subtracting Eq. (5.17, d) from Eq. (5.17, a) we arrive at the following equation:

$$A_n(z = 0) + kQ_n(z = 0) = T_0 - T(z = 0). \qquad (5.18)$$

By using Eq. (5.17, a), Eq. (5.18) can be rewritten in the following form:

$$A_n(z) = T_0 - T(z) - \frac{T_0 - T(z = 0) - A_n(z = 0)}{Q_n(z = 0)} Q_n(z). \quad (5.19)$$

Our results on the OL originated pulse shaping in the CNT suspensions [26] and already presented in the sections 4.2-4.3, suggest that in the vicinity of $z = 0$ the number of nonlinear scattered photons essentially exceed the number of absorbed

photons. Therefore we can estimate $A_n(z)$ by assuming $A_n(z=0)=0$ in Eq. (5.19) and by using $T(z)$ and $Q(z)$ presented in Figs. 5.8, *a,b*, respectively. The calculated $A_n(z)$ is presented in Fig. 5.8, *c*. One can see that the nonlinear absorption of the *M* sample essentially depends on z reaching 25% at $z=4$ mm. Thus, the relative contribution of the nonlinear absorption and the nonlinear scattering essentially depends on the sample position, i.e. on the incident fluence.

In order to investigate the effect on the laser irradiation on the OL performance of ND, *L*, *M*, and *S* samples were exposed to 8000 laser focused pulses with energy (134 ± 20) μJ and a repetition rate of 1 Hz. In the experiment, the laser beam was focused to the same region of each cell for more than two hours, however no visible changes after this exposure were observed. Figure 5.9 presents the transmittance $T(z=0)$ and the energy of scattered pulses as functions of the number laser pulses. It is clearly seen from Fig. 5.9 that the nonlinear transmittance of the *L* sample after exposure to 8000 laser pulses remains the same within the experimental error. The transmittance of the *M* and *S* samples increases from its initial value up to 8 and 20%, respectively. In the *S* sample, the increase of the transmittance is accompanied by the decrease of the energy scattered at 90 degree (see curve *S* in Fig. 5.9, *b*). These experimental findings indicate that in *M* and *S* samples a laser modification of the ND clusters is taken place under the laser irradiation. Such a modification may be associated with the removing an amorphous carbon from the ND clusters via laser-induced chemical reaction of carbon with water ($C+H_2O \rightarrow CO+H_2$) [98], or with oxygen absorbed on the surface of nanodiamond particles ($C+O_2 \rightarrow CO_2$) [99]. These processes are suppressed in *L* sample, which contains bigger particles.

We have recently demonstrated [26,100] (refer to 4.4 section) that in CNT suspensions, the nonlinear scattering cuts off the tail of the incident pulse thus reducing the transmittance when the cell approaching the beam waist. Similar phenomenon we observed in the ND suspensions. Thus, stable aqueous suspensions of ND can also be used for a smooth adjustment of the nanosecond laser pulses duration.
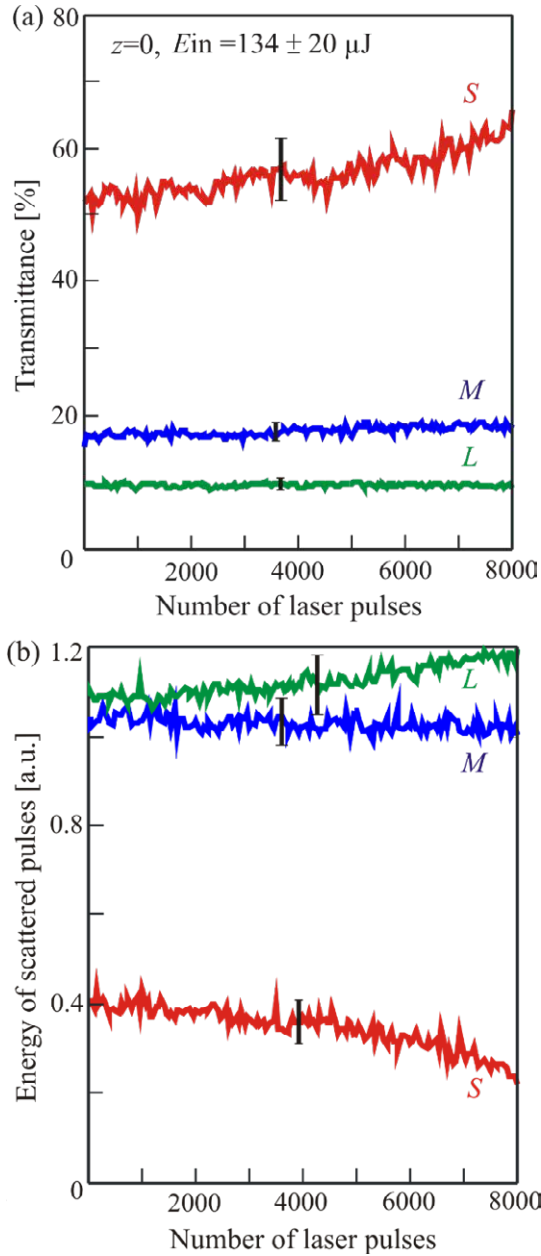
Figure 5.9. *The transmittance (a), and the energy of the scattered at 90 degree light pulses normalized to the energy of the incident pulses (b) as functions of the number of laser pulses. Each point was averaged over 50 laser pulses. Vertical lines show the standard deviation experimental data from the mean values. In the experiment, the studied samples are placed in the focal point and irradiated with the laser pulses with the energy of 134 ± 20 μJ.*

5.3 CONCENTRATION DEPENDENCE OF THE OPTICAL LIMITING AND NONLINEAR LIGHT SCATTERING IN AQUEOUS ND SUSPENSIONS

In this section, we discuss on the OL and the nonlinear light scattering in ND clusters suspended in water with mass concentrations of 3-0.01%.

Aqueous suspensions of detonation ND are stable up to concentrations of as high as 10-12% (hereafter, wt. %) [37], however in our experiments, we used suspensions with the maximum ND concentration of $C = 3\%$. At this concentration, the linear transmittance coefficient of the cell with a thickness of 1.01 mm is $T_0 = 61\%$ at the wavelength of 1064 nm. The same cell containing ND suspensions with concentrations of 1%, 0.1%, and 0.01%, which were obtained from 3 % suspension by adding distilled water, has linear transmittance coefficients of 78, 89, and 90%, respectively.

In the OL measurements, we employed a single-frequency Nd^{3+}: YAG laser with passive Q-switching with 17 ns pulse duration at the wavelength of 1064 nm. The diameter of the beam waist was 100±5 μm. The OL was studied by the developed open-aperture Z-scan technique. For the vertically polarized incident beam the maxima scattering is observed in the plane that is perpendicular to the electric field plane, i.e. in horizontally plane as one may expect for the Mie-Rayleigh scattering [57]. Therefore, the measurements of the energy and the temporal profile of the scattered horizontally light pulses at an angle of 90 degree with respect to the incident beam were carried out. As the light detector and the cell containing suspension are mounted on the positioning stage, therefore for the chosen angle of registration (90°) the active area of the sensor is always opposite to the lateral side of the cell. This significantly simplifies the registering of the scattered photons in the course of Z-scan measurements. Such an approach allowed us to reveal the effect of the nonlinear scattering on the optical limiting at different concentrations of ND clusters.

Figure 5.10 shows the transmittance T and the energy of the 90 degree scattered pulses E_s as functions of the sample position z. Measurements were performed at the incident pulse energy of 1.1 mJ for samples with ND concentrations of $C = 3\%$ (a), $C = 1\%$ (b), $C = 0.1\%$ (c), and $C = 0.01\%$ (d). One can see from Fig. 5.10 that when the intensity increases, the transmittance (squares) sharply decreases, while the energy of the scattered pulses (circles) increases.
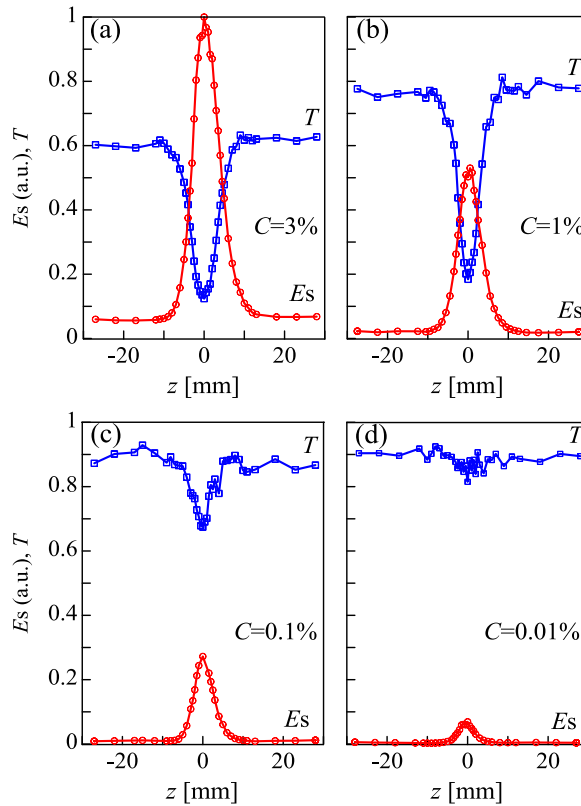
Figure 5.10. *The transmittance T (blue squares), and the energy of the laser pulses scattered at 90 degree Es (red circles) for the ND suspensions with concentrations of C = 3% (a), C = 1% (b), C = 0.1% (c) and C = 0.01% (d) as functions of the sample position z. z = 0 corresponds to the position the focal point at the center of the cell. The energy of the scattered light pulses normalized to the maximum value obtained for suspension with C = 3% at z = 0. Measurements were performed at the incident pulse energy of 1.1 mJ.*

This means that the higher the energy of the scattered pulses, the lower the transmittance. At the low input intensity ($|z|$ >15 mm), the energy of the scattered pulse does not depend on z being more than 20 times smaller than that at $z = 0$. This value originates from the linear scattering that depends on the size and concentration of the ND clusters. It is clearly seen from Fig. 5.10 that in ND suspensions, the nonlinear scattering contributes to the OL in a wide range of concentrations, however the lower the concentration, the weaker the nonlinear scattering. Specifically, the reduction of the concentration from 3% to 0.01% leads to the increase in the transmittance minimum from 12% to 82% and to ten times lower energy of the scattered pulse. Figure 5.11 shows the E_s at $z = 0$ as a function of ND clusters concentration. One can observe that a 300 times increase of the ND concentration gives a 15 times increase in the energy of the 90 degree scattered pulse.
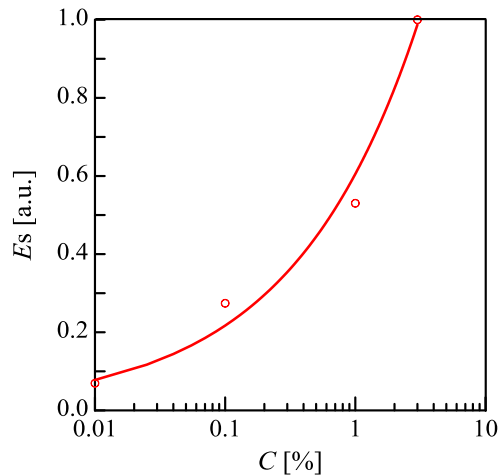
Figure 5.11. *The energy of the laser pulses scattered at 90° as a function of the ND concentration at z = 0. Solid line corresponds to the fitting with equation $E_s = rC^p$, where r = 0.59 and p = 0.44 are fitting parameters.*

One may expect that similarly to carbon nanotubes [5], and carbon black [7] suspensions, the light absorption in the ND suspensions results in heating of the clusters and the formation of the vapor microbubbles surrounding them. The size and hence

the scattering cross section of these microbubbles increases with laser fluence giving rise to the thermal mechanism of the nonlinear light scattering. However when the fluence increases further, the multiphoton ionization may result in the formation and expansion of microplasma as it was observed by Blau et al. for nanotubes [62], and Mansour et al. for carbon black [7]. One may also expect that under high fluence the microplasma can be formed due to the photoionization [101] of some defects in the ND particles. The formation of microplasma results in lower ray stability of suspensions. However, in our experimental conditions, the optical properties of the suspensions did not change because the ND possess higher ray stability in comparison with carbon black and CNT [39].

It is of interest to find out the optimal ND concentration that corresponds to the maximum of the OL performance. For this purpose, in Fig. 5.12 we plot the transmittance at $|z| = 25$ mm (i.e. out of the beam waist) and $z = 0$ (in the beam waist) as functions of the ND concentration using data presented in Fig. 5.10.
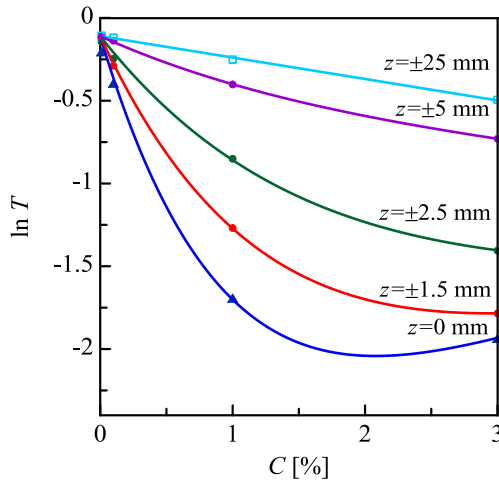
Figure 5.12. *The transmittance of ND suspension as a function of the concentration when focal point is out of the cell ($|z| = 1.5, 2.5, 5$, circles and $|z| = 25$ mm, squares) and in the center of the cell ($z = 0$ mm, triangles). The experimental points are taken from Fig. 5.10. Solid lines represent results of fitting with equation $lnT = -0.11 - 0.129 \times C - A(I) \times C \times exp\{-B(I) \times C\}$, where A ($A > 0$) and B ($B > 0$) are nonlinear functions of light intensity.*

One can observe from Fig. 5.12 that at |z| = 25 mm (squares), ln (T|z|=25mm) is a linear function of C in agreement with the Bouguer-Lambert law [102]. When |z| decreases, the ln$T$ becomes nonlinear function of C (see plotted ln$T$ for $z = ± 5$, $z = ± 2.5$, $z = ± 1.5$ (circles) and $z = 0$ mm (triangles) in Fig. 5.12). The obtained the experimental dependence of the transmittance on the ND concentration C and the light intensity I can be described by introducing the nonlinear correction to the extinction coefficient in the following form:

$$\ln T(|z| < 25\text{mm}) =$$
$$= -0.11 - 0.129\,C - A(I)\,C\,exp\{-B(I)\,C\}, \quad (5.20)$$

where $A(I)$ and $B(I)$ are nonlinear functions of the intensity I, and $A(I = 0) = 0$. The first two terms in the above equation describe the Bouguer-Lambert law, i.e. linear dependence of the extinction coefficient on the ND cluster concentration C. This is the case of low laser intensity, i.e. $z > 25$ mm. The intensity-dependent term in the above equation describes the contribution of the nonlinear scattering and absorption to the extinction coefficient. This dependence is chosen to achieve the best fit for all studied cluster concentrations and intensities.

The OL performance can be quantitatively characterized by the ratio [36]:

$$\xi(C) = \ln(T_{|z|<25\text{mm}})/\ln(T_{|z|=25\text{mm}}). \quad (5.21)$$

This figure of merit, which is presented in Fig. 5.13, *a* as a function of the ND concentration, takes into account both the transmittance of the material at low intensities, and its suppression in the nonlinear regime. Specifically, curve *1* in Fig. 5.13, *a* shows that $\xi(C) = \ln(T$|z|<25mm$)/\ln(T$|z|=25mm$)$ has a maximum at $C_{opt} = 0.88\%$, which can be considered as the optimum C that corresponds to the maximum OL performance in our experimental conditions (i.e. for $F = 100$ mm focal length, pulse energy of 1.1 mJ, and $I = 0.8$ GW/cm² ($z = 0$ mm)). At this concentration, the excitation at the beam waist is about 170 times

higher than that obtained out of the beam waist. Thus the extinction of the ND with $C = 0.88\%$ increases in about 7.14 times when the light intensity increases about 170 times. Curves $2 - 4$ in Fig. 5.13, *a* correspond to the excitations of 0.76 ($|z| = 1.5$), 0.71 ($|z| = 2.5$) and 0.54 GW/cm² ($|z| = 5$ mm), respectively.
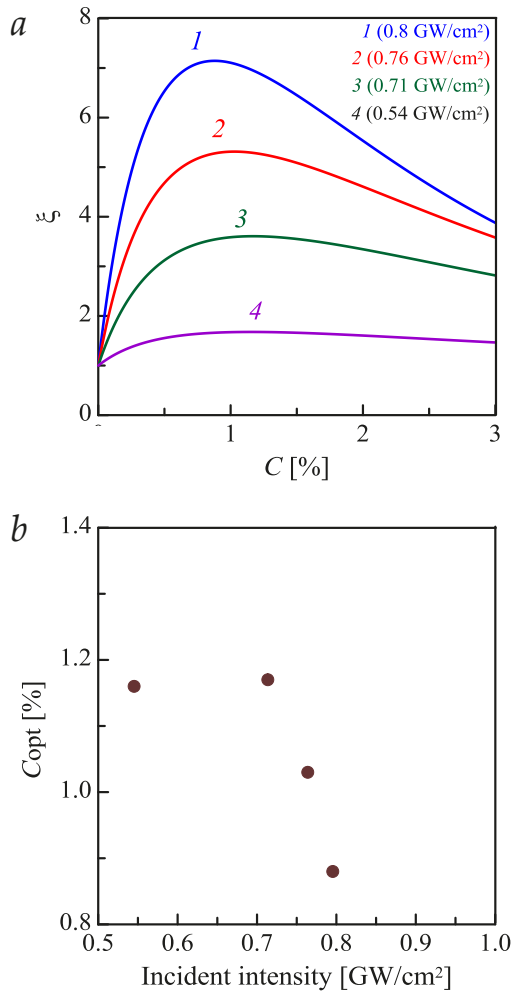
Figure 5.13. (a) The OL performance ξ as a function of the ND concentration C at excitations of 0.8 (1), 0.76 (2), 0.71 (3), and 0.54 GW/cm² (4) that correspond to the sample position at z = 0, 1.5, 2.5, and 5 mm, respectively, in the Z-scan. Solid lines show $\xi(C) = \ln(T|_{z|<25mm})/\ln(T|_{z|=25mm}) = 1+[A(I) \times C \times exp\{-B(I) \times C\}/(0.11 + 0.129 \times C)]$ obtained from fitting of the transmittance data from Fig. 5.12. (b) The optimum ND concentration dependence on the incident intensity. The brown circles correspond to the experimental data.

Non-monotonous dependence of ξ on concentration C presented in Fig. 5.13, *a* can be understood if one recall that intensity-dependent correction to the extinction coefficient, which was introduced in Eq. (5.20) as $\Delta = A\,(I) \times C \times \exp\{-B\,(I) \times C\,\}$, vanishes at low $(C \ll 1)$ and high $(C \gg 1/B\,)$ concentrations. Indeed, when the number of scattering centers (i.e. ND concentration) is small, the light scattering cross section is linearly increases with concentration following the energy absorbed per particle, i.e. in this regime, $(\xi\,(C) - 1) \propto C$. However, at high concentrations of the ND clusters, the light extinction is also high because of linear scattering and absorption. Therefore, the amount of energy absorbed per particle in the focal area of the sample decreases leading to $\xi\,(C\,) \rightarrow 1$ at high concentrations. Indeed the fitting function proposed in Eq. (5.20) gives maximum nonlinear extinction at $C = 1/B$. Most importantly, that similar nonmonotonous dependence of the OL performance on concentration can be made in other nanocarbon suspensions (e.g. carbon nanotubes, carbon black, onion like carbon), when laser induced bleaching [27] does not occur.

One can observe from Fig. 5.13, *a* that the optimal concentration C_{opt} that corresponds to the maximum value of $\xi\,(C)$ essentially depends on the incident intensity. In order to clarify this finding, in Fig. 5.13, *b* we plot the C_{opt} as a function of the incident intensity. The brown circles in figure correspond to the experimental data. Figure 5.13, *b* clearly shows that the optimum concentration increases with decreasing the light intensity, specifically it increases from 0.88% at 0.8 GW/cm^2 up to 1.16 % at 0.54 GW/cm^2. Our additional experiments showed that the optimum concentration of ND in suspension depends on the thickness of the cell as well. The optimum ND concentration in suspension decreases when the cell thickness and thus extinction increases.

5.4 POLARIZATION SENSITIVE NONLINEAR LIGHT SCATTERING AND OPTICAL LIMITING IN AQUEOUS ND SUSPENSIONS

Despite the fact that light polarization may strongly influence the nonlinear optical response of the medium [56], to the best of our knowledge in ND suspensions, the nonlinear polarization effects have been studied neither theoretically nor experimentally. Nevertheless, these effects may be of strong application importance especially for the design of the ND based OL devices that should demonstrate the maximum performance for an arbitrary polarized light beams. Polarization dependence of the nonlinear optical response is crucial for advanced photonics functionalities including pulse shaping [88,100], noise reduction and laser pulse polarization analyzing [103]. In this section, we present the results of the investigation the dependence of the nonlinear light scattering in ND suspension on the polarization of the incident laser beam with focus on the OL applications.

We studied aqueous suspension of ND clusters with an average cluster size of $d_{av.} = 50$ nm. In order to investigate the effect of the polarization on the nonlinear scattering we placed the 1 wt. % stable aqueous ND suspension in 1.01 mm thick cell. The transmittance at the wavelength of $\lambda = 532$ nm is $T_0 = 21.6$ %.

In the OL experiment, we employed Q-switched Nd^{3+}: YAG laser operating at repetition rate of 1 Hz that suits the aqueous solution well [23]. The diameter of the beam waist at the $1/e^2$ intensity level was 70 ± 3.5 μm. The 532 nm laser beam was focused into the edge of the cell containing ND suspension using a $f = 100$ mm lens. The OL in ND suspension were investigated by the Z-scan and the nonlinear transmittance measurements techniques [40]. The experiment was performed using an open-aperture Z-scan shown in Fig. 5.14, a, which is extended to register the scattered at 90 degree photons (see [26]). The polarization plane azimuth Φ of the incident beam (see Fig. 5.14, b) is controlled by rotating the half-wave plate (HWP) placed in the signal leg. The energy of the scattered at 90 degree pulse E_s was measured as a function of polarization plane azimuth Φ of the

incident beam and the sample position *z* with respect to the focal point.
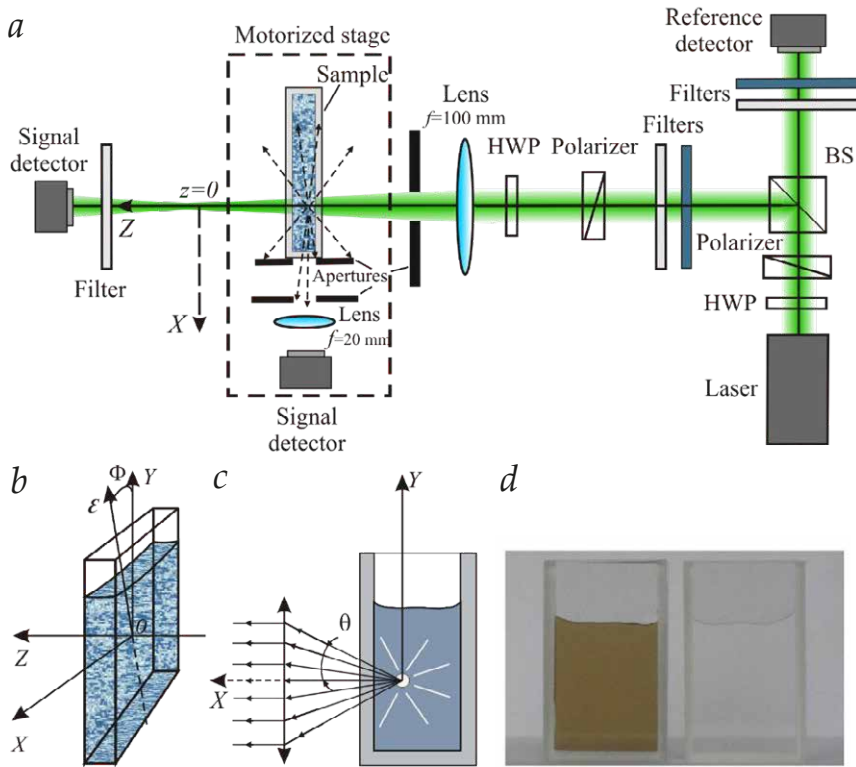
Figure 5.14. *(a) The open-aperture Z-scan setup. (b) Orientation of the electric field vector $\mathcal{E}$ in the linearly polarized incident light beam; light beam propagates along Z axis of the laboratory Cartesian coordinate. (c) The position of the laser beam spot (white circle) inside the cell. A lens that collects scattered at 90 degree light is also shown. (d) A photographic images of the cell containing 1 wt. % suspension with 50 nm ND clusters (left), and distilled water in comparison (right).*

In order to block radiation scattered from interior and exterior walls of the cell, two slit-like apertures were used. The first aperture with a slit size of 1 mm was placed directly on the lateral side of the cell, while the second one with the same slit size was at distance of 15 mm from the cell (see Fig. 5.14, *a*). The lens with the focal distance of *f* = 20 mm and the diameter of 15 mm allowed us collect light scattered inside the cell at 90 degree (see

Fig. 5.14, *c*). In the Z-scan measurements, the cell containing the suspension and the signal detector were moved along the beam axis enabling simultaneous measurements of the energy of transmitted and scattered 90 degree light pulses as functions of distance *z* from the focal point. In the nonlinear transmittance measurements, the focal point coincided with the center of the cell ($z = 0$). The incident fluence was varied by rotating the HWP placed before the beamsplitter (BS) in front of the polarizer in the reference leg. Herewith, the both polarizers on the reference and the signal legs were orientated at the maximum transmittance.

In the open-aperture measurements, the dependence of the transmittance on the cell position *z* with respect to the focal point is shown in Fig. 5.15, *a*. One can see that when the sample was placed at the focal point ($z = 0$), the transmittance shows a sharp minimum for both vertical (●) and horizontal (□) polarizations, indicating a prominent OL behavior. It is clear from Fig. 5.15, *a* that *T* is independent of polarization.

The results of the nonlinear transmittance measurements when the focal point is situated in the center of the cell presented in Fig. 5.15, *b* demonstrate that the transmittance of the ND suspension is the same for orthogonal polarizations of the incident beam. In supplementary experiments, we replaced HWP in the signal leg with the quarter-wave plate and confirmed that *T* is also independent of the beam ellipticity. Thus, we can reveal that the transmittance of the cell with the ND suspension does not depend on the incident light polarization. This is consistent with the observations in carbon particle suspensions and fullerene solutions [104]. The polarization independent OL performance of the ND based optical limiters opens an avenue towards extensive ND application in high-intensity optics.

In order to study the effect of the light polarization on the nonlinear scattering we measured the energy of the light pulse nonlinear scattered at 90 degree as a function of the polarization plane azimuth Φ with respect to the plane of the incidence. The cell was placed at the focal point ($z = 0$), where the input fluence is maximum, and hence, the number of scattered photons is maximum.
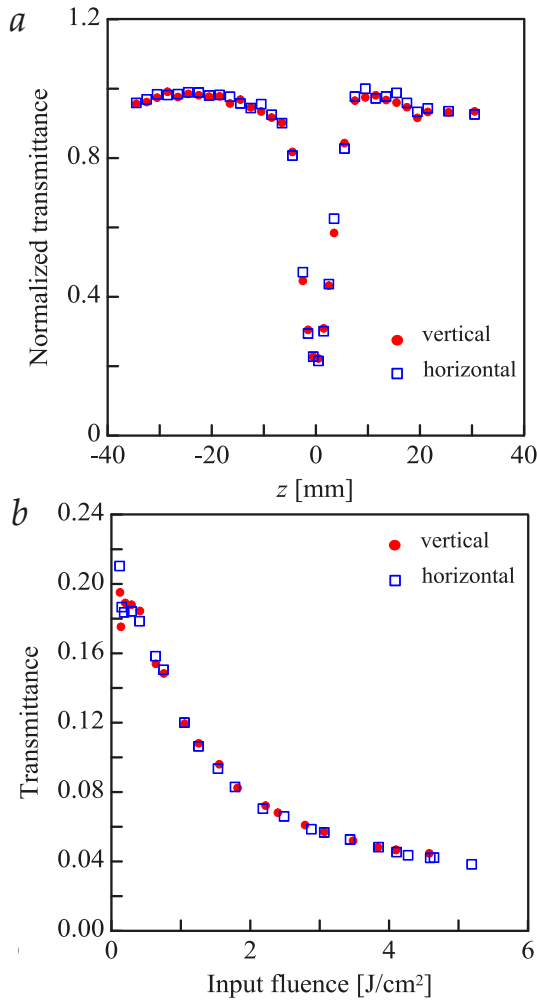
Figure 5.15. *(a) The normalized transmittance of the ND suspension as a function of sample position z for vertical (●) and horizontal (□) polarizations measured in the open aperture Z-scan experiment. (b) The transmittance of 1 wt. % suspension with 50 nm ND clusters on the input fluence for vertical (●) and horizontal (□) polarizations.*

The results of the measurements displayed in Fig. 5.16 (●) clearly indicate that the cross section of the nonlinear light scattering at 90 degree shows a cosine-like dependence on the polarization azimuth of the incident beam. It should be noted that for the linear polarized incident beam the scattered along X-axis light is linearly polarized with polarization azimuth along Y-axis.
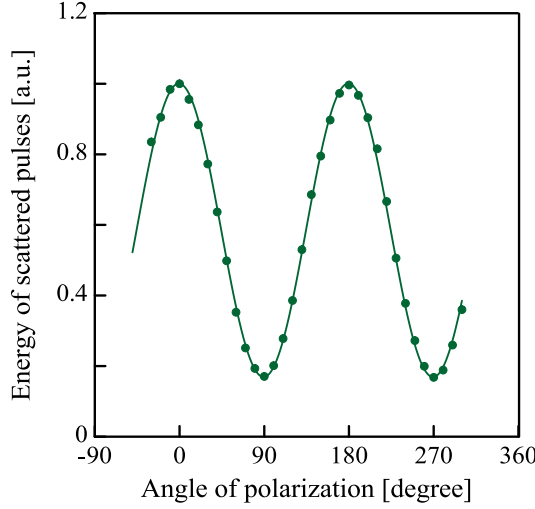
Figure 5.16. *The energy E_s of the nonlinear scattered at 90 degree light pulses on the angle of polarization Φ measured for the cell mounted at the focal point. Green circles correspond to the experimental data, the solid line represents result of fitting with the equation $E_s\ (z{=}0) = E_0\ cos2\Phi + \delta E\ sin^2\Phi$ at $\delta E/E_0 = 0.17$.*

One can observe that the obtained data ($\bullet$) of the energy of the scattered pulses normalized on the incident pulse energy on Φ is well approximated (solid line in above figure) by the following function:

$$E_s(z = 0) = E_0 \cos^2 \Phi + \delta E \sin^2 \Phi. \qquad (5.22)$$

where E_0 and δE are nonlinear scattered energy components corresponding to $\Phi{=}0°$ and $\Phi{=}90°$ respectively, with $\delta E/E_0 = 0.17$. The scattered at 90 degree energy is maximum at $\Phi = 0°$, i.e. when the incident beam is polarized along the Y axis. When the light is horizontally polarized ($\Phi = 90°$, see Fig. 5.14, *b*) the energy of the scattered at 90 degree pulses is minimum. One may expect that in such a case the scattering occur mainly along the Y axis. This implies that the differential cross section of the light scattering depends on the light polarization as one may expect for the Rayleigh-Mie scattering [57]. At the same time, it is worth noting that the total scattered energy (or the scattering cross section) is polarization independent. In order to demonstrate this it is

instructive to consider the energy balance that can be presented by the following equation:

$$T = 1 - A - S - R, \qquad (5.23)$$

where T, A, S, and R are relative (with respect to the incident pulse) number of transmitted, absorbed, scattered, and reflected photons, respectively. At the normal incidence, the reflectivity is polarization independent. Since the suspension is isotropic, one may expect that the relative number of the absorbed photons for orthogonal linear polarizations will also be the same. Finally, the performed Z-scan and the nonlinear transmittance measurements revealed that the relative number of the transmitted photons does not depend on the incident light polarization (see Fig. 5.15). Therefore, one can conclude that the relative number of the scattered photons is also polarization independent. At the same time the differential cross section of the light scattering depends on the light polarization, i.e. most interestingly, one can control the direction of the nonlinear scattered light by changing the polarization of the incident light.

Nonzero δE in Eq. (5.22), can be explained in terms of the Rayleigh-Mie scattering. In the Rayleigh regime ($d < \lambda/15$), the scattering along the polarization direction of the incident beam is forbidden [57]. In our experimental setup (see Fig. 5.14), this implies that scattering along the X axis ($\theta = 0°$, see Fig. 5.14, c) should be absent if the incident beam is X-polarized ($\Phi = 90°$), and hence $\delta E = 0$. However, one can see from Fig. 5.16 that in our experiments, the measured signal does not vanish at $\Phi = 90°$. There are two mechanisms that may result in non-zero δE in Eq. (5.22). Firstly, in our experiment we measured the energy of the light pulse scattered in a finite solid angle, i.e. the lens in Fig. 5.14, c collects light beams scattered at a finite angle θ with respect to the X axis. Since the Rayleigh scattering cross section at $\theta \neq 0°$ is nonzero, we arrive at nonzero δE in Eq. (5.22). The second mechanism that can lead to non-zero δE is the presence of the ND clusters of larger size ($d > \lambda/15$) in the suspension. These clusters scatter light in the Mie regime, i.e. scattering along the

polarization direction of the incident beam is not suppressed [57]. Thus at $\Phi = 90°$, the differential scattering cross section is nonzero both at $\theta = 0°$ and at $\theta \neq 0°$ also contributing to δE.

It is most important that the decreasing the size of the ND clusters down to below $\lambda/15$ allows one to obtain the zero second term in Eq. (5.22), i.e. to achieve the Rayleigh scattering regime when $E_s = E_0 \cos^2 \Phi$. This means that the ND suspension with the clusters sizes below $\lambda/15$ can be employed to reveal polarization of the laser beam. Indeed, zero energy of the scattered horizontally at 90 degree light pulses is a signature of the X-polarized ($\Phi = 90°$) incident light.

In order to evaluate the polarization dependence of the E_0 and δE on the input fluence we varied the incident power by rotating the HWP in the signal leg (see Fig. 5.14, a). The measured energies of the scattered pulses for vertical, E_s ($\Phi = 0°$) = E_0, and horizontal, E_s ($\Phi = 90°$) = δE, polarizations of the incident beam as functions of the input fluence are shown in Fig. 5.17.
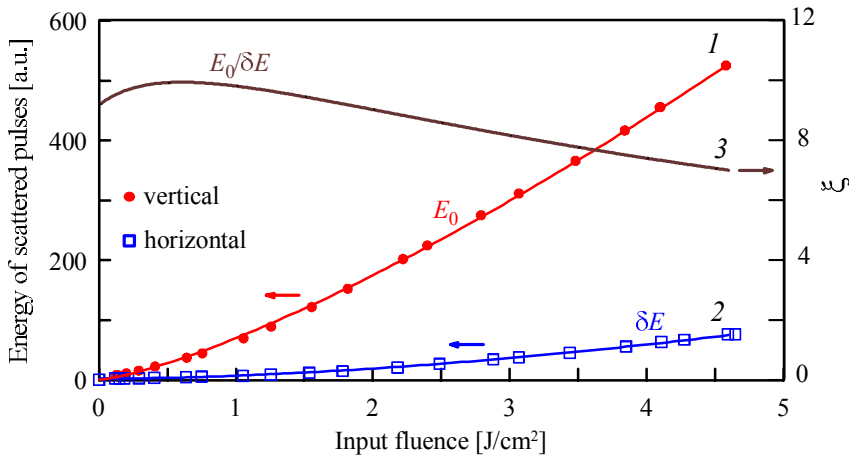
Figure 5.17. *The energy of the scattered at 90 degree pulses for vertical 1, and horizontal 2 polarizations as functions of the input fluence P_{in}. Dots and squares correspond to the experimental data, the solid lines 1 and 2 represent results of fitting with equations $E_0 = \sigma_V P_{in} [1 + B_V (1 - e^{-P_{in}/P_V})]$ at $B_V = 3.76$, $P_V = 2.36$ J/cm^2 for vertical ($\Phi = 0$), and $\delta E = \sigma_H P_{in} [1 + B_H (1 - e^{-P_{in}/P_H})]$ at $B_H = 13.66$, $P_H = 11.39$ J/cm^2 for horizontal ($\Phi = 90°$) polarizations, respectively, with $\sigma_H/\sigma_V = 0.11$. Experimental data deviation is less than 1%. Solid line 3 shows the ratio $\xi = E_s(\Phi = 0) / E_s(\Phi = 90°) = E_0 / \delta E$.*

Solid lines in the figure are the fitting of the experimental data with the following functions:

$$E_0 = \sigma_V P_{in}\left[1 + B_V\left(1 - e^{-P_{in}/P_V}\right)\right], \qquad (5.24, a)$$

$$\delta E = \sigma_H P_{in}\left[1 + B_H\left(1 - e^{-P_{in}/P_H}\right)\right], \qquad (5.24, b)$$

where σ_H and σ_V are differential cross sections of the linear scattering for the light polarized horizontally and vertically with respect to the scattering plane, respectively, and $\sigma_H/\sigma_V = 0.11$. Parameters $B_V = 3.76$, $P_V = 2.36$ J/cm² and $B_H = 13.66$, $P_H = 11.39$ J/cm² describe the contribution of the nonlinear scattering to the measured signals for X- and Y- polarized incident beams, respectively. At $P_{in} \ll P_{V,H} / B_{V,H}$ the second terms in square brackets in the right-hand side of the Eqs. (5.24, a, b) can be neglected, i.e. only linear scattering takes place.

As one may expect, in the linear scattering regime, the measured signal for the Y-polarized incident beam is much higher than that for the X-polarized. As we mentioned above, this is because when the incident beam is X-polarized, the Rayleigh scattering is forbidden and the measured signals originate from the Mie scattering (due to the presence of relatively small amount of large ND clusters in the suspension) and a finite collection solid angle (see Fig. 5.14, c).

Since $P_V \ll P_H$ the nonlinear scattering for the vertically polarized beam manifest itself at lower P_{in} than that for the horizontally polarized one. One may expect that at relatively low incident fluence radius of vapor bubbles increases thus leading to the increasing of the Rayleigh scattering. As a result in this fluence range, the formation of the bubbles results in a nearly parabolic growth of the scattered energy, $E_0 \approx \sigma_V P_{in} (1+B_V P_{in} /P_V)$. However at $P_{in} > P_V$ the exponential term in the Eq. (5.24, a) can be neglected and the scattered energy becomes proportional to the first power of the input fluence, $E_0 \approx \sigma_V (1+B_V) P_{in}$, that is nonlinear scattering can be described in terms of the fluence independent effective differential cross section $\sigma_V^{eff} = \sigma_V (1+B_V)$. This experimental finding can be explained by results of the

numerical simulation of bubbles kinetics in aqua nanocarbon suspensions performed in [64] and already presented in the review section 2.2.2 of the Thesis. Specifically, in [64] it have been demonstrated that for 10 ns long laser pulses, the radius of the vapor bubbles that are formed around CNT (and hence the scattering cross section) becomes independent on the input fluence at $P_{in} > 0.4$ J/cm². Starting from this fluence, the energy absorbed by a carbon nanoparticle cannot anymore result in the heating and evaporation of water because the heat transfer from the nanoparticle to the water is suppressed due to presence of the vapor. In CNT suspensions, the further increase of the fluence results in the distortion of nanoparticles However, the ND suspensions have much better ray stability and we can expect that they will be destroyed at much higher fluencies.

For the horizontally polarized incident beam ($\Phi = 90°$) the scattering energy is much lower than that for the vertically polarized one. However since P_V/B_V is the same order as P_H/B_H, the nonlinear scattering manifests itself for both X- and Y-polarized incident beams. However in contrast to the case of $\Phi = 0°$, the scattered energy for horizontally polarized beam is a nonlinear function of the input fluence in the whole measured range. Since $P_{in} < P_H$ the Eq. (5.24, b) can be reduced down to $\delta E \approx \sigma_H P_{in} (1 + B_H P_{in}/P_H)$ (Eq. (5.24, a) cannot be reduced down to a similar form since P_{in} is comparable with P_V). That is in contrast to the case of the vertically polarized incident beam, the differential scattering cross section continue increasing despite the fact that the size of the vapor bubbles does not change. This indicates that at $\Phi = 90°$, the measured signal originates from the Mie rather than from the Rayleigh scattering.

The polarization dependence of the nonlinear scattering can be quantitatively characterized by the ratio:

$$\xi = \frac{E_s(\Phi = 0)}{E_s(\Phi = 90°)} = \frac{E_0}{\delta E}. \qquad (5.25)$$

This ratio for the linear scattering will give a constant value and will not depend on the input fluence. However it can be seen

(Fig. 5.17, curve *3*) that for the nonlinear scattering ξ (P_{in}) is a non-monotonous function that has a maximum at $P_{in} = 0.6$ J/cm^2. We observed similar non-monotonous behavior of ξ (P_{in}) for ND suspensions with concentrations from 1 to 0.01 wt. %. Such a non-monotonous dependence of the ratio E_s ($\Phi=0°$) / E_s ($\Phi=90°$) on the input fluence may be explained by the modification of the ND clusters under the laser irradiation. At $P_{in} < 0.6$ J/cm^2 the increase of the incident pulse energy results in the breaking the larger ND clusters into the smaller ones. This leads to the increase of the Rayleigh scattering of the light polarized along *Y*-axis ($\Phi = 0°$), and hence, to the increase of ξ. At $P_{in} > 0.6$ J/cm^2, irradiation with the intense laser beam results in the formation of micron sized light-induced scattering centers (e.g. microplasma) that results in the enhancement of the Mie scattering contribution to the measured signal and hence to the increasing the E_s ($\Phi = 90°$).

In addition to the exceptional ray and sedimentation stability, the ND suspensions possess a low OL threshold. This parameter, which is defined as the input fluence at which the transmittance is halved [94], allows one to compare quantitatively performance of different OL materials [105]. Figure 5.13, *b* clearly shows that the ND transmittance is halved at 1.2 J/cm^2 which is comparable with 1 J/cm^2 obtained by Sun et al. for multiwalled carbon nanotube suspensions in water at linear transmittance of 50% at 532 nm [94].

5.5 OPTICAL LIMITING IN ND SUSPENSIONS IN NEAR-INFRARED SPECTRAL RANGE

Fast optical nonlinearity and a low limiting threshold allow one to employ carbon nanotubes, carbon black, graphene, carbon dots and nanodiamonds for the OL in the visual and the near infrared (NIR) spectrum ranges. The latter makes these materials of high importance for suppression the intensity fluctuations in optical telecommunication and data-processing systems working in the wavelengths range of 1400-1600 nm [106]. In nanocarbon materials, the OL may originate from the various processes

including nonlinear refraction, nonlinear absorption and nonlinear scattering. It has been shown that in nanocarbon suspensions, the nonlinear scattering caused by the formation of bubbles, sublimation of carbons and microplasma dominate OL in the visual spectrum range making possible in particular to control the temporal profile of the laser pulse [100]. However in the NIR range (1100-2500 nm), the information on the nonlinear filtering with nanocarbon materials is rather limited [107,108]. This is partially because conventional solvents including ethanol, toluene, dimethylformamide, distilled water etc. strongly absorb radiation in the NIR range [109], i.e. they cannot be employed for preparing of nanocarbon suspensions.

In order to evaluate the OL performance of the nanocarbon materials in the optical communication window we perform measurements in heavy water (D_2O) ND suspensions. We measured the OL response in 3 and 4.5 wt. % ND suspensions with an average cluster size of 110 nm. The thickness of all samples was 2 mm. D_2O was employed as a host liquid because of its low (in comparison with H_2O, see inset to Fig. 5.18) absorption in the wavelength region of 1100-1600 nm [110].
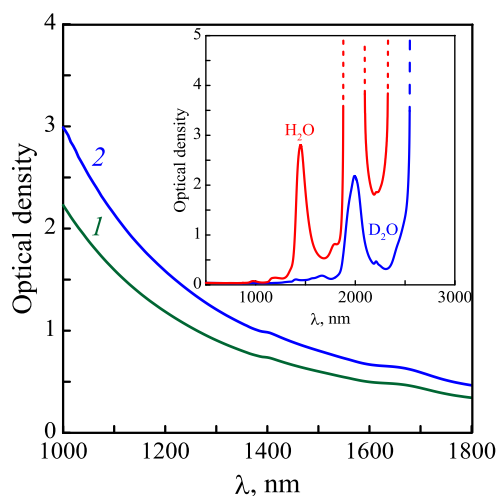
Figure 5.18. *NIR optical density of 2 mm thick samples with ND concentrations of 3 (1) and 4.5 wt.% (2) in dependence of the wavelength. Optical density is measured relative to heavy water. The inset shows the optical density spectra of 2 mm thick samples of water and heavy water relative to air.*

The data shown in Fig. 5.18 are consistent with previous reported [111], specifically one can observe that in the studied wavelength range, the longer the wavelength, the higher the optical density of the ND suspensions.

In order to evaluate the OL performance of the fabricated suspensions in the NIR spectrum range, we employed an open-aperture Z-scan setup that enables simultaneous measurement the energy of the transmitted and scattered at 90 degree pulses on the sample position z. (see Fig. 5.19).
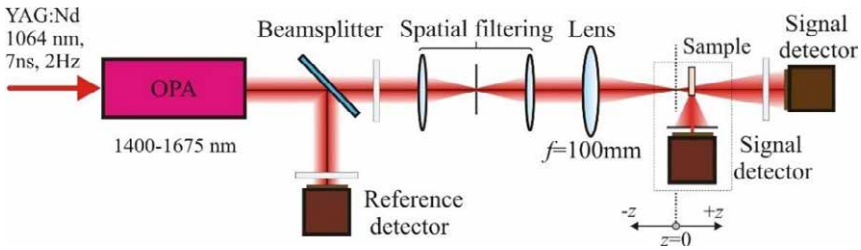
Figure 5.19. The sketch of the open-aperture Z-scan experimental setup.

In the nonlinear optical measurements we employed the optical parametrical amplifier (OPA, Laser Vision, USA) pumped by the first and the second harmonics of the Nd^{3+}: YAG laser with 7 ns pulses at a repetition rate of 2 Hz. The output radiation in the wavelength range of 1350-5000 nm was spatially filtered in order to obtain a single mode beam. The diameter of the beam waist at $1/e^2$ intensity level at the wavelength of 1500 nm was $2w_0 = 60$ μm. The nonlinear optical response of the ND samples was measured at seven different wavelengths of 1400, 1450, 1500, 1550, 1600, 1650 and 1675 nm at the pulse energy of $E_{in} = 0.2$ mJ.

Figure 5.20 shows the normalized transmittance at the wavelengths of 1400, 1450, 1500, 1600, 1675 nm as a function of the sample position. For all the wavelengths, one can clearly observe the OL of the incident laser pulse, i.e. the reduction of the sample transmittance when the light fluence increases. It is worth noting that for the both studied samples, the maximum attenuation was achieved at the shortest wavelength. In particular, for the suspension with 4.5 wt.% ND concentration,

the suppression of the transmittance was as high as 45 % at the wavelength of 1400 nm.
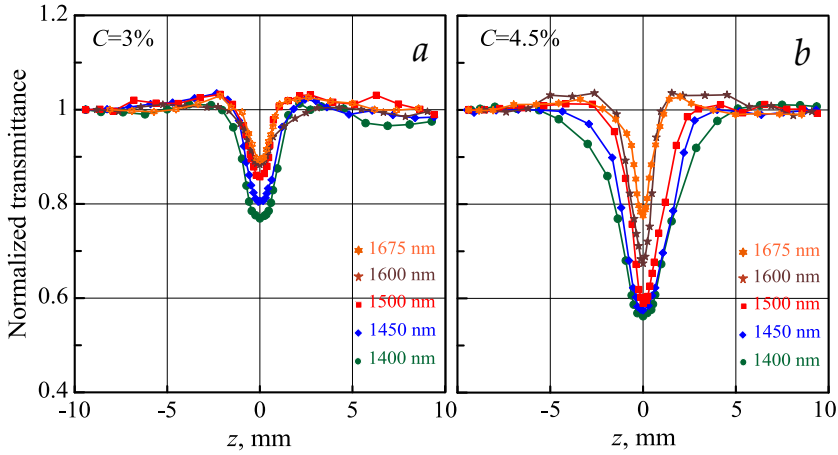
Figure 5.20. *The normalized transmittances of the heavy water ND suspensions with 3 (a) and 4.5 wt.% (b) concentrations as functions of z. z=0 corresponds to the position of the focal point at the center of the sample. The measurements were performed at the incident pulse energy of 0.2 mJ and the pulse duration of 7 ns.*

The OL efficiency η can be quantitatively characterized by the ratio of the transmittance T_0 measured at $|z| > 5$ mm to the transmittance T_{nl} measured at $z = 0$ (when the fluence is maximum), i.e. $\eta = T_0/T_{nl}$ [112]. The dependence of η on the OPA wavelength in Fig. 5.21 clearly shows the decrease of the OL efficiency with the increase of the wavelength. This effect may originate from the lower absorption coefficient of the light, as well as from the decreasing of the light scattered cross section [57] with the longer wavelengths.

The important role of the nonlinear scattering in the observed effect was confirmed by the measurements of the energy of the light pulses scattered at 90 degree with respect to the incident beam. The simultaneously recorded normalized transmittance and the scattered at 90 degree pulse energy for the sample with 4.5 wt.% ND concentration are given in Fig. 5.22.
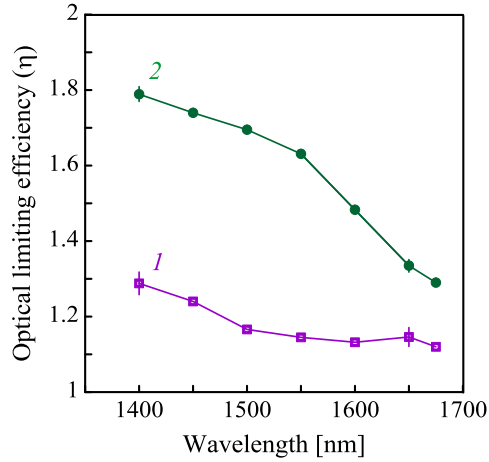
Figure *5.21.* *The wavelength dependence of the OL efficiency* *η* *for ND clusters dispersed in D₂O with mass concentrations of 3 (1) and 4.5 % (2). The sample thickness is 2 mm. Vertical lines show the deviation the experimental data from the mean values.*
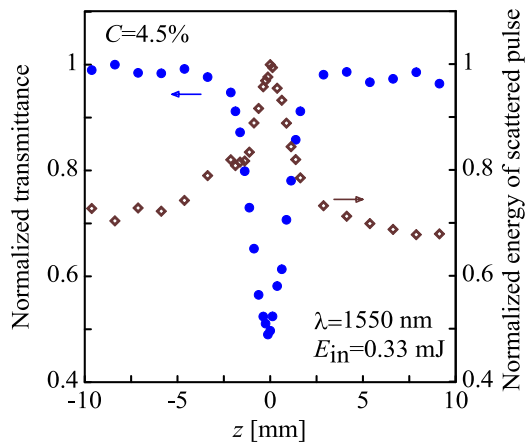
Figure *5.22.* *The normalized transmittance (solid blue circles), and the normalized energy of the scattered pulse (open diamond) as functions of the sample position z relative to the focal plane. The measurements performed at the wavelength of 1550 nm at the pulse energy of 0.33 mJ.*

As one can see from the figure, the minimum of the sample transmittance corresponds to the maximum scattered energy, confirming a direct link between the power limiting and an increase of the scattering cross section. The nonlinear scattering

in suspension with 4.5 wt.% concentration of ND clusters is stronger than that in the suspension with 3 wt.% concentration. Correspondingly, the dependence of the transmittance on the sample position in the Fig. 5.20, *b* is more pronounced than that in the Fig. 5.20, *a*. This experimental finding is consistent with results obtained at the fundamental wavelength of a Nd^{3+}: YAG laser and originates from the increasing of the number of the scattering centers in the focal volume when the ND concentration increases [36,113].

5.6 SATURABLE ABSORPTION IN ND SUSPENSIONS

The shortest laser pulses are generated when phases of cavity modes are synchronized. Such a synchronization a time domain is called mode-locking. It can dramatically change the laser performance leading to generation of trains of pico- or femtosecond pulses with MHz repetition rate. In order to achieve mode-locking regime, the laser cavity should include a saturable absorber (SA), an optical component whose optical loss decreases at high light intensity [114]. The faster the mechanism of the optical nonlinearity in the SA, the shorter the pulses can be generated in the cavity.

Recent advances in nanotechnology have made it possible to create materials well suited for laser applications [115]. At present, the most efficient SA are quantum well based semiconductor saturable absorber mirrors (SESAMs) [116]. However, these advanced nonlinear optical materials are capable of working in a narrow spectral range (in the close vicinity of an interband resonant transition) and may suffer from a fast laser-induced degradation.

CNT that possess fast and strong optical nonlinearity offer interesting alternative to SESAMs in the spectral range of 1-2 μm. It is worth noting, however that necessity of polymer matrix to embed the CNTs and dependence of the working range on the tube diameter significantly narrows the applicability of CNTs as the SA [117–119]. That is why the attention of scientists and

engineers is recently attracted to graphene based SA. They are capable to operate at any wavelength due to unusual gapless band structure, which makes optical properties of graphene practically independent on the wavelength for the visual and IR light. The generation of the femtosecond pulses achieved with graphene SA has been first demonstrated in 2009 [120]. The strong optical nonlinearity and subpicosecond relaxation times allow one to use graphene based materials for mode locking and Q-switching for lasers operating in wide spectral range [121–122].

However, advances in fabrication of graphene and CNT along with their exciting optical properties overshadowed the ND, a nanomaterial with sp^3 hybridization of carbon orbitals which possesses a number of unique properties [77,78]. In above sections, we have shown that ND suspensions can possess strong nonlinearity that can be employed for the OL of the nanosecond pulses. In this section, we report the results of the nonlinear optical studies in the ND suspensions in the femtosecond domain. Femtosecond Z-scan showed that the higher the intensity, the lower the optical losses. This is the clear indication that this carbon nanomaterial can also be employed as a SA.

In the experiments, the ND clusters with an average size of 50 nm were suspended in water with mass concentrations of 0.75%, 1%, 1.5%, and 2%. The transmittance spectra and the photographic images of the samples are presented in Fig. 5.23. The optical microscopy measurements were performed relative to distilled water (shown in Fig. 5.23 for comparison).

In the experiments, we employed Ti: sapphire laser operating at the wavelength of λ=795 nm with the repetition rate of 1 kHz and the pulse duration of 120 fs. Measurements were performed using the fundamental 795 nm beam. The computerized Z-scan setup allowed us controlling of the both parameters of the laser pulses and sample position. The focal length was 75 mm and the beam diameters at the focus was as low as $2w_0 \approx 34.5$ μm. In order to register the energy of the incident and transmitted pulses we used the reference and signal photodetectors, respectively. The energy of the incident beam at the sample varied from 60 nJ to 200 μJ by rotating the half-waveplate HWP.
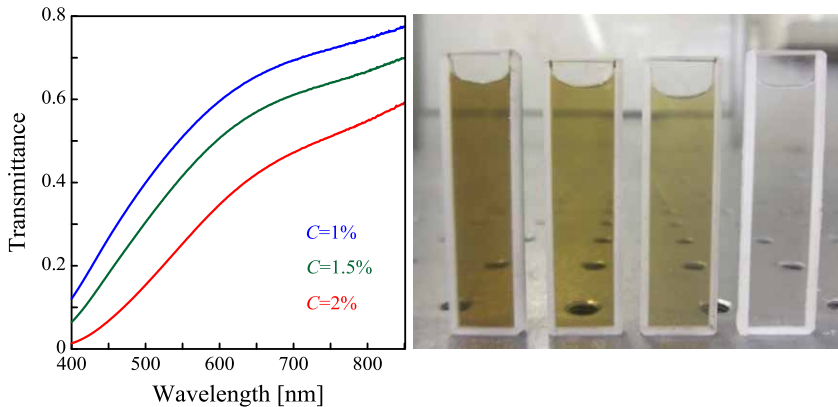
Figure 5.23. *The transmittance spectra of the 50 nm ND clusters dispersed in distilled water with mass concentrations of 2, 1.5, and 1%. The measurements were performed in a 1 mm quartz cell relative to distilled water. Right figure presents a photographic images of the cell containing 2, 1.5, and 1 wt. % suspension with 50 nm ND clusters, and distilled water in comparison.*

The open aperture Z-scan was used to determine the nonlinear absorption coefficients of the samples. Figure 5.24 presents the normalized transmittance dependence $T(z)$ measured at the incident pulse energies of 60 and 100 nJ. which corresponds to excitations of 53.4 and 89 GW/cm² , respectively. The figure is clearly indicating the negative sign of the nonlinear absorption. The upper Z-scan in the figure is vertically shifted for clear presentation. For all the Z-scan experiments reported in this section, the maximum intensity of the laser pulses was 178 GW/cm² , however no laser-induced damaged was observed at intensities below 500 GW/cm² . Above this excitation, the white light continuum generation in water was observed. Figure 5.24, *a* indicates that the transmittance in the 2% ND suspension increases due to saturable absorption as cell with ND suspension approaches the focal point, i.e. $z=0$. At the laser pulse excitations of 53.4 and 89 GW/cm² the saturation riches 3.3 and 3.8%, respectively. It is clearly seen that transmittance dependence is an even function with respect to $z=0$, hence, light-induced bleaching does not occur.
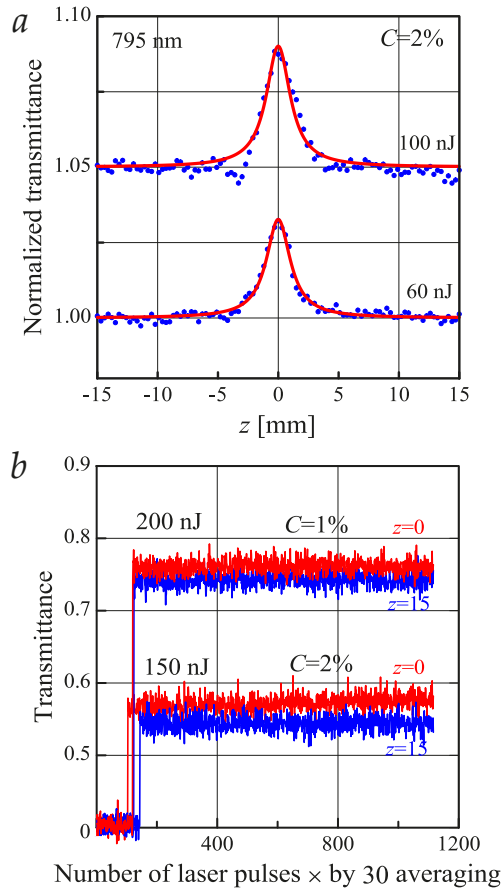
Figure 5.24. (a) The normalized transmittances of the ND samples with mass concentration of 2% measured in the course of Z-scan for the incident pulse energies of 60 and 100 nJ. The upper Z-scan is vertically shifted for clear presentation. Solid lines represent the result of fitting. Figure (b) represents the transmittance of the ND samples with concentrations of 1 and 2% placed either in the vicinity of the focal point (z=0), and away from it (z=15 mm) measured for the pulse energies of 200 and 150 nJ, respectively as functions of the number of laser pulses. Each experimental point in figure was averaged over 30 laser pulses. The measurements were performed for the femtosecond laser pulses at the wavelength of 795 nm.

In order to demonstrate this we measured the transmittance of the ND samples as function of the number of laser pulses, i.e. as a function of time. In these experiments, two ND samples with mass concentrations of 2 and 1% were placed in the focal point (z=0) and at the distance of z=15 mm from it, and were exposed to

more than 30 thousands femtosecond laser pulses with pulse energies of 150 and 200 nJ that corresponds to excitations of 133 and 178 GW/cm^2, respectively. The results of the experiments are presented in Fig. 5.24, *b*. Each experimental point in the figure was averaged over 30 laser pulses. One may clearly see that the transmittance for both samples and both positions remain constant. This implies that no light-induced irreversible transparency occurs, and that the transmittance increase originates from the saturation of the light absorption in the ND.

The origin of the revealed effect may be associated with a strong increase of absorption in 1-2 eV photon energy region which was recently discovered for the ND particles in [111]. In a pure diamond bulk crystal, the optical absorption is absent because of the large band gap (about 5.4 eV), however, ND suspension is semi-transparent and its extinction is monotonically decreases when the wavelength increases. This extinction is caused by the both light scattering, and the optical absorption due to the presence of graphite and dimer chains on the surface of nanoparticles [111]. The presence of dimer chains (Pandey dimer chains) on the nanocrystal diamond surface leads to the appearance of the absorption band in the range of 1 to 2 eV with a peak at 1.5 eV. Most interestingly, that this peak coincides with the photon energy (1.56 eV) used in our experiments. It is worth noting that we observed no saturable absorption induced transmittance changes in the supplementary experiments performed at 614 and 1300 nm, i.e. photon energies of 2.02 and 0.95 eV, respectively.

For the light intensities used in our experiments (< 178 GW/cm^2), the two-photon absorption in water was too low to outperform the saturation of the linear absorption in ND. However, for the excitations exceeding 350 GW/cm^2, the two-photon absorption processes in water become noticeable effecting on the transmittance curve.

In the absence of two-photon absorption in water, the intensity dependence of the absorption coefficient of the ND suspension can be described by the following equation [41,48]:

$$\alpha(I) = \frac{\alpha_0}{1 + I/Is},\qquad(5.26)$$

where α_0 is a linear absorption coefficient, I and Is are the incident and saturation intensities, respectively. The experimental data in Fig. 5.24, *a* can be approximated with a fitting parameter Is. The best fit was obtained and presented as solid lines in Fig. 5.24, *a*. with $Is = 9.5 \times 10^2$ GW/cm^2 (for 2% ND sample). This value is about 135 times higher than that obtained for bilayer graphene on a SiC substrate at the wavelength of 780 nm [41].
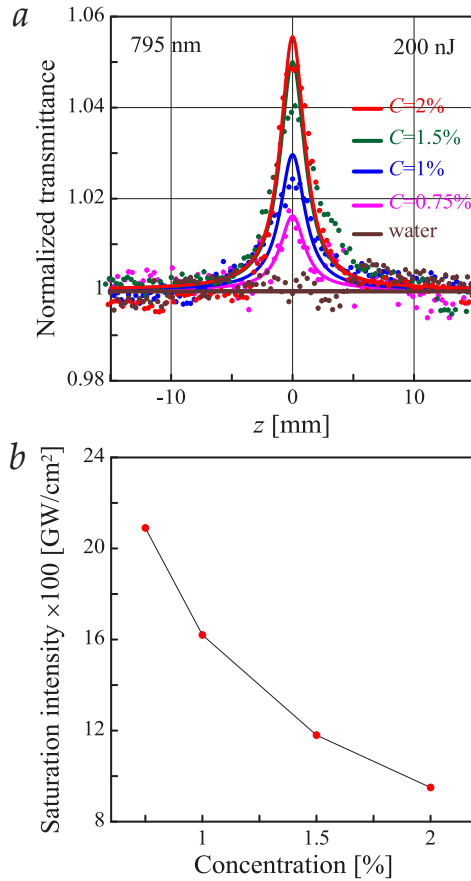
Figure 5.25. (a) *The normalized transmittances of the ND suspension samples with mass concentrations of 2, 1.5, 1, and 0.75 % measured in the course of Z-scan for the incident pulse energy of 200 nJ. The water response is presented in comparison. Solid lines represent the result of fitting. (b) The evaluated saturation intensity as a function of the ND concentration indicating a monotonous behavior.*

In order to study the concentration dependence of the effect we performed similar measurements for ND suspensions with concentrations of 2, 1.5, 1, 0.75 % and the pulse energy of 200 nJ. The results of the measurements are presented in Fig. 5.25, *a*. Response in water, as it was mentioned before, at this excitation was found to be zero, and however we presented it in the same figure for comparison. In the all studied samples, the saturable absorption response clearly manifests itself indicating a prominent saturation intensity (I_s) dependence on the concentration. The I_s values obtained using Eq. (5.26) for the studied ND samples are presented as a function on concentration in Fig. 5.25, *b*. As it can be clearly seen, the concentration increase results in the decrease of the saturation intensity in the ND suspensions. Specifically, the concentration increase in 2,7 times results in 2.2 times decrease in saturation intensity. One can expect that the more decrease of the saturation intensity can be achieved by the further increase of the particles concentration.

In conclusion, we observed a transmittance increase in ND suspensions with femtosecond laser pulse excitation at the wavelength of 795 nm. This increase have been found generating from the saturable absorption rather than from the light-induced irreversible transparency. The revealed effect originates from a strong increase of absorption in 1-2 eV photon energy region with a peak at 1.5 eV, which coincides with the photon energy (1.56 eV) used in the experiments. We have demonstrated experimentally that in a wide range of the ND concentrations saturable absorption contributes to the negative nonlinear absorption. The saturation intensity have been found a monotonous function on concentration allowing one to regulate the saturation intensity in a particular application. The observed nonlinear phenomenon presents a clear indication that ND can also be employed as a saturable absorber.

CONCLUSIONS OF CHAPTER 5

In conclusion, we observed the OL of nanosecond laser pulses in stable aqueous suspensions of detonation nanodiamond clusters with the average size of 50, 110, and 320 nm. In all the samples, the OL originates from the nonlinear absorption and the nonlinear scattering rather than from the nonlinear refraction. The relative contribution of the nonlinear scattering and the nonlinear absorption essentially depends on the incident fluence. The OL threshold decreases with increasing the average size of the ND clusters. Nanoparticles with the average size of 320 nm show better OL performance compared to 50 nm in the high fluence region and are capable of absorbing laser pulses with power density about 0.2 GW/cm^2 for a long time without changing their nonlinear optical properties.

We have demonstrated experimentally that the OL performance of stable aqueous ND suspensions is a non-monotonous function of concentration. In a wide range of ND concentrations the nonlinear light scattering strongly contributes to the OL performance. The optimum concentration that corresponds to the maximum OL performance essentially depends on the cell thickness, as well as on the incident intensity. Most importantly, that such a conclusion is valid for other nanocarbon suspensions (e.g. carbon nanotubes, carbon black, onion like carbon), when laser induced bleaching does not occur.

We have determined experimentally that the light polarization does not effect on the nonlinear transmittance of the ND suspension, while it significantly influences on the pattern of the nonlinear scattering in the plane perpendicular to the plane passing through the incident beam (for example vertical). The energy of the nonlinear scattered at 90 degree pulse shows a cosine-like dependence on the polarization plane azimuth of the incident beam. At the same time, in contrary to the linear scattering, the ratio of the energies of the laser pulses nonlinear scattered along and perpendicular to the polarization azimuth of the incident beam is a non-monotonous function of the input fluence. The non-monotonous dependence can be interpreted by

the interplay of the light-induced breaking of the ND clusters and the formation of the light-induced scattered centers in the suspension.

We also showed that the heavy water suspensions of the detonation ND enable efficient OL in the wavelength range of 1400-1675 nm. In this nanocarbon material, the efficiency of the nonlinear filtering decreases with increasing the wavelength. The observed nonlinear filtering makes D_2O ND suspension a prospective material for photonic and optical data processing devices operating in the optical communication window.

In the femtosecond time scale, we observed also the increase in the ND transmittance at the wavelength of 795 nm. This effect is originated from the saturation of the light absorption in the ND suspension and manifests in a wide range of the nanodiamond concentrations.

6 Summary

In this Thesis, we investigate mechanisms of the optical limiting (OL) phenomenon in nanocarbon materials. The performed comprehensive study has revealed that the nonlinear light scattering dominates the OL in aqueous suspensions of carbon nanotube (CNT) and detonation nanodiamonds (ND). The presented experimental findings indicate that these materials are well suited for the limiting the high intensity laser beams.

The performed nanosecond Z-scan measurements at the wavelength of 532 nm revealed the OL performance essential dependence on the particle size. Specifically, the larger the particle size, the better the OL performance and the higher the ray stability of the ND suspension. The nanosecond nonlinear transmittance and Z-scan measurements at 532 nm also showed that the nonlinear transmittance of the ND suspension is independent of polarization, whereas the latter significantly influences the pattern of the nonlinear scattering. The ratio of the energies of the vertically and horizontally polarized scattered pulses has been found a nonmonotonous function of the input fluence.

The performed pulse temporal profile measurements demonstrated that in the OL regime, the nonlinear light scattering cuts off the trailing part of the transmitted pulse. This result makes possible to employ the CNT and the ND suspensions for the controlling of the nanosecond laser pulse duration. The presented results of Z-scan measurements at 1064 nm indicate that the OL performance of the nanocarbon suspensions is a nonmonotonous function of concentration. Moreover, the performed analyses revealed that the optimum concentration that corresponds to the maximum OL performance essentially depends on the incident light intensity.

By using nanosecond Z-scan measurements we also demonstrate that the heavy water ND suspension enable strong

optical limiting in the wavelength range of 1400-1675 nm. The presented enhancement of the OL performance has been observed in the blue part of the communication window.

The performed femtosecond Z-scan experiments at 795 nm revealed the negative sign of the nonlinear absorption in the ND suspension. This effect has been demonstrated originating from the saturation of the light absorption in the ND suspension.

Bibliography

[1]   L.W. Tutt and T.F. Boggess, "A review of optical limiting mechanisms and devices using organics, fullerenes, semiconductors and other materials," *Prog. Quantum Electron*. **17**, 299–338 (1993).

[2]   L.W. Tutt, A. Kost, "Optical limiting performance of C_{60} and C_{70} solutions," *Nature* **356**, 225–226 (1992).

[3]   D.J. Hagan, T. Xia, A.A. Said, T.H. Wei, E.W. Van Stryland, "High dynamic range passive optical limiters," *Inter. J. Nonl. Opt. Phys*. **2**, 483 (1993).

[4]   E.W. Van Stryland, S.-B. Mansoor, "Z-scan measurements of optical nonlinearities," in *Characterization Techniques and Tabulations for Organic Nonlinear Materials* (1998), pp. 655–692.

[5]   L. Vivien, P. Lanc, D. Riehl, F. Hache, E. Anglaret, "Carbon nanotubes for optical limiting," *Carbon* **40**, 1789–1797 (2002).

[6]   X.-F. Jiang, L. Polavarapu, S.T. Neo, T. Venkatesan, and Q.-H. Xu, "Graphene oxides as tunable broadband nonlinear optical materials for femtosecond laser pulses," *J. Phys. Chem. Lett*. **3**, 785–790 (2012).

[7]   K. Mansour, M.J. Soileau, and E.W. Van Stryland, "Nonlinear optical properties of carbon-black suspensions (ink)," *J. Opt. Soc. Am. B* **9**, 1100–1109 (1992).

[8]   E. Koudoumas, O. Kokkinaki, M. Konstantaki, S. Couris, S. Korovin, P. Detkov, V. Kuznetsov, S. Pimenov, V. Pustovoi,

"Onion-like carbon and diamond nanoparticles for optical limiting," *Chem. Phys. Lett*. **357**, 336–340 (2002).

[9] B. Zhao, B. Cao, W. Zhou, D. Li, W. Zhao, "Nonlinear optical transmission of nanographene and its composites," *J. Phys. Chem. C* **114**, 12517–12523 (2010).

[10] G.-K. Lim, Z.-L. Chen, J. Clark, R.G.S. Goh, W.-H. Ng, H.-W. Tan, R.H. Friend, P.K.H. Ho, L.-L. Chua, "Giant broadband nonlinear optical absorption response in dispersed graphene single sheets," *Nat. Photonics* **5**, 554–560 (2011).

[11] K.C. Chin, A. Gohel, H.I. Elim, W.Z. Chen, W. Ji, G.L. Chong, C.H. Sow, A.T. Wee, "Modified carbon nanotubes as broadband optical limiting nanomaterials," *J. Mater. Res*. **21**, 2758–2766 (2006).

[12] Y. Chen, Y. Lin, Y. Liu, J. Doyle, N. He, X. Zhuang, J. Bai, W.J. Blau, "Carbon nanotube-based functional materials for optical limiting," *J. Nanosci. Nanotechnol*. **7**, 1268–1283 (2007).

[13] J. Wang and W. J. Blau, "Inorganic and hybrid nanostructures for optical limiting," *J. Opt. A Pure Appl*. Opt. **11**, 1–16 (2009).

[14] S.A. Curran, P.M. Ajayan, W.J. Blau, D.L. Carroll, J.N. Coleman, A.B. Dalton, A.P. Davey, A. Drury, B. McCarthy, S. Maier, A. Strevens, "A composite from poly (m-phenylenevinylene- carbon nanotubes: a novel material for molecular optoelectronics," *Adv. Mater*. **10**, 1091–1093 (1998).

[15] S.M. O'Flaherty, R. Murphy, S.V. Hold, M. Cadek, J.N. Coleman, W.J. Blau, "Material investigation and optical limiting properties of carbon nanotube and nanoparticle dispersions," *J. Phys. Chem*. B **107**, 958–964 (2003).

[16] S.M. O'Flaherty, S.V. Hold, M.E. Brennan, M. Cadek, A. Drury, J.N. Coleman, W.J. Blau, "Nonlinear optical response of multiwalled carbon-nanotube dispersions," *J. Opt. Soc. Am. B* **20**, 49–58 (2003).

[17] J. Wang, W.J. Blau, "Nonlinear optical and optical limiting properties of individual single-walled carbon nanotubes," *Appl. Phys. B* **91**, 521–524 (2008).

[18] J. Wang, W.J. Blau, "Solvent effect on optical limiting properties of single-walled carbon nanotube dispersions," *J. Phys. Chem. C* **112**, 2298–2303 (2008).

[19] S. Giordani, S.D. Bergin, V. Nicolosi, S. Lebedkin, M.M. Kappes, W.J. Blau, J.N. Coleman, "Debundling of single-walled nanotubes by dilution: observation of large populations of individual nanotubes in amide solvent dispersions," *J. Phys. Chem. B* **110**, 15708–15718 (2006).

[20] P. Chen, X. Wu, X. Sun, J. Lin, W. Ji, K.L. Tan, "Electronic structure and optical limiting behavior of carbon nanotubes," *Phys. Rev. Lett.* **82**, 2548–2551 (1999).

[21] N. Izard, P. Billaud, D. Riehl, E. Anglaret, "Influence of structure on the optical limiting properties of nanotubes," *Opt. Lett.* **30**, 1509–11 (2005).

[22] S.R. Mishra, H.S. Rawat, S.C. Mehendale, K.C. Rustagi, A.K. Sood, R. Bandyopadhyay, A. Govindaraj, C.N.R. Rao "Optical limiting in single-walled carbon nanotube suspensions," *Chem. Phys. Lett.* **317**, 510–514 (2000).

[23] F.E. Hernández, W. Shensky, I. Cohanoschi, D.J. Hagan, E. Van Stryland, "Viscosity dependence of optical limiting in carbon black suspensions," *Appl. Opt.* **41**, 1103–7 (2002).

[24] L. Vivien, D. Riehl, P. Lançon, F. Hache, E. Anglaret, "Pulse duration and wavelength effects on the optical limiting

behavior of carbon nanotube suspensions," *Opt. Lett.* **26**, 223–225 (2001).

[25] X. Sun, Y. Xiong, P. Chen, J. Lin, W. Ji, J. Lim, S. Yang, D.J. Hagan, E.W. Van Stryland, "Investigation of an optical limiting mechanism in multiwalled carbon nanotubes," *Appl. Opt.* **39**, 1998–2001 (2000).

[26] G.M. Mikheev, T.N. Mogileva, A.V. Okotrub, D.L. Bulatov, V.V. Vanyukov, "Nonlinear light scattering in a carbon nanotube suspension," *Quantum Electron.* **40**, 45–50 (2010).

[27] G.M. Mikheev, V.L. Kuznetsov, D.L. Bulatov, T.N. Mogileva, S.I. Moseenkov, A.V. Ishchenko, "Optical limiting and bleaching effects in a suspension of onion-like carbon," *Quantum Electron.* **39**, 342–346 (2009).

[28] G.M. Mikheev, V.L. Kuznetsov, K.G. Mikheev, T.N. Mogileva, S.I. Moseenkov, "Laser-induced diamagnetism in suspension of onion-like carbon particles," *Tech. Phys. Lett.* **37**, 831–834 (2011).

[29] S.R. Mishra, H.S. Rawat, S.C. Mehendale, "Reverse saturable absorption and optical limiting in C_{60} solution in the near-infrared," *Appl. Phys. Lett.* **71**, 1998–2001 (1997).

[30] N.V. Kamanina, L.N. Kaporskii, B.V. Kotov, "Absorption spectra and optical limiting of the fullerene–polyimide system," *Opt. Commun.* **152**, 280–282 (1998).

[31] R.A. Ganeev, T. Usmanov, "Nonlinear-optical parameters of various media," *Quantum Electron.* **37**, 605–622 (2007).

[32] J. Wang, Y. Chen, R. Li, H. Dong, Y. Ju, J. He, J. Fan, K. Wang, K.-S. Liao, L. Zhang, S. Curran, W.J. Blau, "Graphene and carbon nanotube polymer composites for laser protection," *J. Inorg. Organomet. Polym. Mater.* **21**, 736–746 (2011).

[33] J. Wang, Y. Hernandez, M. Lotya, J. Coleman, W.J. Blau, "Broadband nonlinear optical response of graphene dispersions," *Adv. Mater.* **21**, 2430–2435 (2009).

[34] Y. Zhou, Q. Bao, L.A.L. Tang, Y. Zhong, K.P. Loh, "Hydrothermal dehydration for the "green" reduction of exfoliated graphene oxide to graphene and demonstration of tunable optical limiting properties," *Chem. Mater.* **21**, 2950–2956 (2009).

[35] M. Feng, H. Zhan, Y. Chen, "Nonlinear optical and optical limiting properties of graphene families," *Appl. Phys. Lett.* **96**, 033107–0331010 (2010).

[36] S. Josset, O. Muller, L. Schmidlin, V. Pichot, D. Spitzer, "Nonlinear optical properties of detonation nanodiamond in the near infrared: Effects of concentration and size distribution," *Diam. Relat. Mater.* **32**, 66–71 (2013).

[37] A.P. Puzyr, V.S. Bondar, "Nanodiamonds for biological investiga-tions," *Phys. Solid State* **46**, 716–719 (2004).

[38] N. Gibson, O. Shenderova, T.J.M. Luo, S. Moseenkov, V. Bondar, A. Puzyr, K. Purtov, Z. Fitzgerald, D.W. Brenner, "Colloidal stability of modified nanodiamond particles," *Diam. Relat. Mater.* **18**, 620–626 (2009).

[39] G.M. Mikheev, A.P. Puzyr, V.V. Vanyukov, K.V. Purtov, T.N. Mogileva, V.S. Bondar, "Nonlinear scattering of light in nanodiamond hydrosol," *Tech. Phys. Lett*. **36**, 358–361 (2010).

[40] V.V. Vanyukov, T.N. Mogileva, G.M. Mikheev, A.P. Puzyr, V.S. Bondar, Y.P. Svirko, "Size effect on the optical limiting in suspensions of detonation nanodiamond clusters," *Appl. Opt*. **52**, 4123–4130 (2013).

[41] H. Yang, X. Feng, Q. Wang, H. Huang, W. Chen, A.T.S. Wee, W. Ji, "Giant two-photon absorption in bilayer graphene," *Nano Lett*. **11**, 2622–7 (2011).

[42] J. Wang, Y. Chen, W.J. Blau, "Carbon nanotubes and nanotube composites for nonlinear optical devices," *J. Mater. Chem*. **19**, 7425-7443 (2009).

[43] F. Hache, D. Ricard, C. Flytzanis, U. Kreibig, "The optical kerr effect in small metal particles and metal colloids: the case of gold," *Appl. Phys. A* **47**, 347–357 (1988).

[44] Li. Yang, K. Becker, F.M. Smith, R.H. Magruder, R.F. Haglund, L. Yang, R. Dorsinville, R.R. Alfano, R.A. Zuhr, "Size dependence of the third-order susceptibility of copper nanoclusters investigated by four-wave mixing," *J. Opt. Soc. Am. B* **11**, 457 (1994).

[45] B. Palpant, "Third order nonlinear optical response of metal nanoparticles," in *Non-Linear Optical Properties of Matter: From Molecules to Condensed Phases* (2006), pp. 461–508.

[46] R.A. Ganeev, A.I. Ryasnyansky, A.L. Stepanov, T. Usmanov, "Saturated absorption and nonlinear refraction of silicate glasses doped with silver nanoparticles at 532nm," *Opt. Quantum Electron.* **36**, 949–960 (2004).

[47] R.A. Ganeev, A.I. Ryasnyansky, A.L. Stepanov, T. Usmanov, "Characterization of nonlinear optical parameters of copper- and silver-doped silica glasses at 1064 nm," *Phys. Status Solidi B* **944**, 935–944 (2004).

[48] R.A. Ganeev, A.I. Ryasnyansky, A.L. Stepanov, T. Usmanov, "Saturated absorption and reverse saturated absorption of $Cu: SiO_2$ at 532 nm," *Phys. Status Solidi B* **4**, 3–6 (2004).

[49] R.A. Ganeev, A.I. Ryasnyansky, A.L. Stepanov, T. Usmanov, "Nonlinear optical susceptibilities of copper- and silver-doped silicate glasses in the ultraviolet range," *Phys. Status Solidi B* **238**, R5–R7 (2003).

[50] R.A. Ganeev, A.I. Ryasnyansky, S.R. Kamalov, M.K. Kodirov, T. Usmanov, "Nonlinear susceptibilities, absorption coefficients and refractive indices of colloidal metals," *J. Phys. D. Appl. Phys.* **34**, 1602–1611 (2001).

[51] R.G. Ispasoiu, L. Balogh, O.P. Varnavski, D.A. Tomalia, T. Goodson, "Large optical limiting from novel metal-dendrimer nanocomposite materials," *J. Am. Chem. Soc.* **122**, 11005-11006 (2000).

[52] L. Francois, M. Mostafavi, J. Belloni, J.A. Delaire, "Optical limitation induced by gold clusters: mechanism and efficiency," *Phys. Chem. Chem. Phys.* **3**, 4965–4971 (2001).

[53] L. Francois, M. Mostafavi, J. Belloni, J.-F. Delouis, J. Delaire, P. Feneyrou, "Optical Limitation induced by Gold Clusters. 1. Size Effect," *J. Phys. Chem. B* **104**, 6133–6137 (2000).

[54] S.R. Mishra, H.S. Rawat, M. Laghate, "Nonlinear absorption and optical limiting IN metalloporphyrins," *Opt. Commun.* **147**, 328–332 (1998).

[55] W. Blau, H. Byrne, W.M. Dennis, and J.M. Kelly, "Reverse saturable absorption in tetraphenylporphyrins," *Opt. Commun.* **56**, 25–29 (1985).

[56] L. Landau, E. Lifshitz, *Electrodynamics of Continuous Media* (Pergamon Press, 1960).

[57] C.F. Bohren, D.R. Huffman, *Absorption and Scattering of Light by Small Particles* (Wiley, N.Y., 1983).

[58] J. Strutt, "On the light from the sky, its polarization and colour," *Philos. Mag.* **41**, 87-103 (1871).

[59] J. Strutt, "On the scattering of light by small particles," *Philos. Mag.* **41**, 104-110 (1871).

[60] J. Seinfeld, S. Pandis, *Atmospheric Chemistry and Physics*, 2nd Edition, John Wiley and Sons, (New Jersey, 2006).

[61] J. Stratton, *Electromagnetic Theory* (New York: McDraw-Hill, 1941).

[62] J. Wang, Y. Chen, R. Li, H. Dong, L. Zhang, M. Lotya, J. Coleman, W.J. Blau, "Nonlinear optical properties of graphene and carbon nanotube composites," Siva Yellampalli, Carbon Nanotubes-Synthesis, Characterization, Applications. (InTech Uurope, 2011), 397–424.

[63] I.M. Belousova, N.G. Mironova, A.G. Scobelev, M.S. Yur'ev, "The investigation of nonlinear optical limiting by aqueous suspensions of carbon nanoparticles," *Opt. Commun.* **235**, 445–452 (2004).

[64] I.M. Belousova, N.G. Mironova, M.S. Yur'ev, "Theoretical investigation of nonlinear limiting of laser radiation power by suspensions of carbon particles," *Lasers and their Appl.* **94**, 92–98 (2003).

[65] V. Joudrier, P. Bourdon, F. Hache, C. Flytzanis, "Characterization of nonlinear scattering in colloidal suspensions of silica particles," *Appl. Phys. B Lasers Opt.* **70**, 105–109 (2000).

[66] I. Papagiannouli, A.B. Bourlinos, A. Bakandritos, S. Couris, "Nonlinear optical properties of colloidal carbon nanoparticles : nanodiamonds and carbon dots," *RSC Adv.* **4**, 40152–40160 (2014).

[67] A.V. Okotrub, L.G. Bulusheva, A.I. Romanenko, A.L. Chuvilin, N.A. Rudina, Y.V. Shubin, N.F. Yudanov, "Anisotropic properties of carbonaceous material produced in arc discharge," *Appl. Phys. A* **486**, 481–486 (2001).

[68] A.V. Okotrub, N.F. Yudanov, V.M. Aleksashin, L.G. Bulusheva, O.A. Komarova, U.O. Kostas, P.N. Gevko, N.V. Antyufeeva, S.I. Il'chenko, G.M. Gunyaev, "Study of thermal and mechanical properties of composites based on arc-grown carbon nanotubes and heat-resistant cyanoether binder," *Polym. Sci. Ser. A* **49**, 702–707 (2007).

[69] J.L. Bahr and J.M. Tour, "Covalent chemistry of single-wall carbon nanotubes," *J. Mater. Chem.* **12**, 1952–1958 (2002).

[70] V.S. Bondar, A.P. Puzyr, "A method of obtaining an explosive synthesis of nanodiamonds with high colloidal stability," Russian Patent 2252192 (2005).

[71] A.P. Puzyr, V.S. Bondar, A.A. Bukayemsky, G.E. Selyutin, V.F. Kargin, "Physical and chemical properties of modified nanodiamonds," in *Syntheses, Properties and Applications of Ultrananocrystalline Diamond*, D. Gruen, ed. (Kluver Academic Publishers, 2005), 261–270.

[72] M. Dubois, K. Guérin, E. Petit, N. Batisse, A. Hamwi, N. Komatsu, J. Giraudet, P. Pirotte, and F. Masin, "Solid-state NMR study of nanodiamonds produced by the detonation technique," *J. Phys. Chem. C* **113**, 10371–10378 (2009).

[73] V. Mochalin, S. Osswald, Y. Gogotsi, "Contribution of functional groups to the raman spectrum of nanodiamond powders," *Chem. Mater.* **21**, 273–279 (2009).

[74] I.I. Vlasov, O. Shenderova, S. Turner, O.I. Lebedev, A.A. Basov, I. Sildos, M. Rähn, A.A. Shiryaev, G.Van Tendeloo,

"Nitrogen and luminescent nitrogen-vacancy defects in detonation nanodiamond," *Small* **6**, 687–694 (2010).

[75] G.M. Mikheev, K.G. Mikheev, T.N. Mogileva, A.P. Puzyr, V.S. Bondar, "Laser image recording on detonation nanodiamond films," *Quantum Electron.* **44**, 1–3 (2014).

[76] P.-H. Chung, E. Perevedentseva, C.-L. Cheng, "The particle size-dependent photoluminescence of nanodiamonds," *Surf. Sci.* **601**, 3866–3870 (2007).

[77] M.Y. Shalaginov, G.V. Naik, S. Ishii, M.N. Slipchenko, A. Boltasseva, J.X. Cheng, A.N. Smolyaninov, E. Kochman, V.M. Shalaev, "Characterization of nanodiamonds for metamaterial applications," *Appl. Phys. B Lasers Opt.* **105**, 191–195 (2011).

[78] J.M. Say, C.V. Vreden, D.J. Reilly, L.J. Brown, J.R. Rabeau, N.J.C. King, "Luminescent nanodiamonds for biomedical applications," *Biophys. Rev.* **3**, 171–184 (2011).

[79] R. Greenwood, K. Kendall, "Selection of suitable dispersants for aqueous suspensions of zirconia and titania powders using acoustophoresis," *J. Eur. Ceram. Soc.* **19**, 479–488 (1999).

[80] S.-B. Mansoor, A.A. Said, T.-H. Wei, D.J. Hagan, E.W. Van Stryland, "Sensitive measurement of optical nonlinearities using a single beam," *IEEE J. Quantum Electron.* **26**, 760–769 (1990).

[81] R.A. Ganeev, S.R. Kamalov, I.A. Kulagin, A.V. Zinov'ev, V.I. Redkorechev, A.I. Ryasnyansky, R.I. Tugushev, T. Usmanov, "An automated setup for investigating nonlinear optical characteristics of various materials by the Z-scan method," Gen. Exp. Tech. **45**, 810–815 (2002).

[82] R.A. Ganeev, N.V. Kamanina, I.A. Kulagin, A I. Ryasnyansky, R. I. Tugushev, T. Usmanov, "Study of nonlinear optical characteristics of various media by the methods of Z-scan and third harmonic generation of laser radiation," *Quantum Electron.* **32**, 781–788 (2002).

[83] X. Liu, S. Guo, H. Wang, L. Hou, "Theoretical study on the closed-aperture Z-scan curves in the materials with nonlinear refraction and strong nonlinear absorption," *Opt. Commun.* **197**, 431–437 (2001).

[84] A.A .Said, S.-B. Mansoor, D.J. Hagan, T.H. Wei, J. Wang, J. Young, E.W. Van Stryland, "Determination of bound-electronic and free-carrier nonlinearities in ZnSe, GaAs, CdTe, and ZnTe," *J. Opt. Soc. Am. B* **9**, 405–414 (1992).

[85] G.M. Mikheev, D.I. Maleev, T.N. Mogileva, "Efficient passively *Q*-switched single-frequency YAG:Nd^{3+} laser with polarized coupling out of radiation," *Sov. J. Quantum Electron.* **22**, 37–39 (1992).

[86] M. Pessot, P. Maine, G. Maine, "1000 times expansion/ compression of optical pulses for chirped pulse amplification," *Opt. Commun.* **62**, 419-421 (1987).

[87] J.M. Khosrofian, B.A. Garetz, "Measurement of a Gaussian laser beam diameter through the direct inversion of knife-edge data," *Appl. Opt.* **22**, 3406-3410 (1983).

[88] G.M. Mikheev, T.N. Mogileva, A.V. Okotrub, V.V. Vanyukov, "Shapes of laser radiation pulses modified by nonlinear scattering in aqueous suspension of carbon nanotubes," *Tech. Phys. Lett.* **36**, 195–198 (2010).

[89] A. Penzkofer, D. Linde, A. Laubereau, and W. Kaiser, "Generation of single picosecond and subpicosecond light pulses," *Appl. Phys. Lett.* **20**, 351–354 (1972).

[90] V.A. Gorbunov, S.B. Papernyĭ, V.F. Petrov, V.R. Startsev, "Time compression of pulses in the course of stimulated Brillouin scattering in gases," *Sov. J. Quantum Electron.* **13**, 900–905 (1983).

[91] R.R. Buzyalis, V. Girdauskas, A.S. Dementjev, V.B. Ivanov, E.K. Kosenko, A.A. Mak, S.B. Papernyĭ, V.A. Serebryakov, "Multistage stimulated-scattering compression of pulses from a YAG: Nd laser," *Sov. J. Quantum Electron.* **17**, 1444–1446 (1987).

[92] A.J. Kiran, D. Udayakumar, K. Chandrasekharan, H.D. Shashikala, R. Philip, "Nonlinear optical studies of a newly synthesized copolymer containing oxadiazole and substituted thiophenes," *Opt. Commun.* **271**, 236–240 (2007).

[93] D. Vincent, S. Petit, S.L. Chin, "Optical limiting studies in a carbon-black suspension for subnanosecond and subpicosecond laser pulses," *Appl. Opt.* **41**, 2944–2946 (2002).

[94] X. Sun, R.W. Yu, G.Q. Xu, T.S.A. Hor, W. Ji, "Broadband optical limiting with multiwalled carbon nanotubes," *Appl. Phys. Lett.* **73**, 3632–3634 (1998).

[95] Q. Wang, Y. Qin, Y. Zhu, X. Huang, Y. Tian, P. Zhang, Z.X. Guo, Y. Wang, "Optical limiting performances of multi-walled carbon nanotubols and [C60]fullerols," *Chem. Phys. Lett.* **457**, 159–162 (2008).

[96] T. Olivier, F. Billard, H. Akhouayri, "Nanosecond Z-scan measurements of the nonlinear refractive index of fused silica," *Opt. Express* **12**, 1377–1382 (2004).

[97] M.R. Ferdinandus, M. Reichert, T.R. Ensley, H. Hu, D. Fishman, S. Webster, D.J. Hagan, E.W. Van Stryland, "Dual-arm Z-scan technique to extract dilute solute

nonlinearities from solution measurements," *Opt. Mater. Express* **2**, 1776–1790 (2012).

[98] K.-Y. Niu, H.-M. Zheng, Z.-Q. Li, J. Yang, J. Sun, X.-W. Du, "Laser dispersion of detonation nanodiamonds," *Angew. Chem. Int. Ed.* **50**, 4099–4102 (2011).

[99] K.-W. Lin, C.-L. Cheng, H.-C. Chang, "Laser-induced intracluster reactions of oxygen-containing nanodiamonds," *Chem. Mater.* **10**, 1735–1737 (1998).

[100] V.V. Vanyukov, T.N. Mogileva, G.M. Mikheev, A.V. Okotrub, D.L. Bulatov, "Application of nonlinear light scattering in nanocarbon suspensions for adjustment of laser pulse duration," *J. Nanoelectron. Optoelectron.* **7**, 102–106 (2012).

[101] N.B. Manson, J.P. Harrison, "Photo-ionization of the nitrogen-vacancy center in diamond," *Diam. Relat. Mater.* **14**, 1705–1710 (2005).

[102] M. Born, E. Wolf, "Principles of Optics," (Pergamon Press LTD, London 1961).

[103] G.M. Mikheev, V.M. Styapshin, "Nanographite analyzer of laser polarization," *Instruments Exp. Tech.* **55**, 85–89 (2012).

[104] K. Nashold, D.P. Walter, "Investigations of optical limiting mechanisms in carbon particle suspensions and fullerene solutions," *J. Opt. Soc. Am. B* **12**, 1228 (1995).

[105] D. Vincent, "Optical limiting threshold in carbon suspensions and reverse saturable absorber materials," *Appl. Opt.* **40**, 6646–53 (2001).

[106] P.A. Bouit, G. Wetzel, G. Berginc, B. Loiseaux, L. Toupet, P. Feneyrou, Y. Bretonnière, K. Kamada, O. Maury, C. Andraud, "Near IR nonlinear absorbing chromophores

with optical limiting properties at telecommunication wavelengths," *Chem. Mater.* **19**, 5325–5335 (2007).

[107] N.V. Kamanina, M.O. Iskandarov, A.A. Nikitichev, "Middle infrared optical investigations of fullerene-2-(n-prolinol)-5-nitropyridine," *Opt. Commun.* **225**, 337–340 (2003).

[108] N. Liaros, E. Koudoumas, S. Couris, "Broadband near infrared optical power limiting of few layered graphene oxides," *Appl. Phys. Lett.* **104**, (2014).

[109] L.A. Kazicina, N.B. Kupletskaya, "Application of UV-, IR- and NMR spectroscopy in organic chemistry," *Opt. Commun.* **225**, 337–340 (2003).

[110] C.L. Braun, S.N. Smirnov, "Why is water blue?," *J. Chem. Educ.* **70**, 612–614 (1993).

[111] A.E. Aleksenskii, A.Y. Vul', S.V. Konyakhin, K.V. Reich, L.V. Sharonova, E.D. Eidel'man, "Optical properties of detonation nanodiamond hydrosols," *Phys. Solid State* **54**, 578–585 (2012).

[112] S.-H. Chi, J. M. Hales, M. Cozzuol, C. Ochoa, M. Fitzpatrick, J.W. Perry, "Conjugated polymer-fullerene blend with strong optical limiting in the near-infrared.," *Opt. Express* **17**, 22062–22072 (2009).

[113] V.V. Vanyukov, G.M. Mikheev, T.N. Mogileva, A.P. Puzyr, V.S. Bondar, Y.P. Svirko, "Concentration dependence of the optical limiting and nonlinear light scattering in aqueous suspensions of detonation nanodiamond clusters," *Opt. Mater.* **37**, 218–222 (2014).

[114] G. Steinmeyer, "Frontiers in ultrashort pulse generation: pushing the limits in linear and nonlinear optics," *Science* **286**, 7–12 (1999).

[115] U. Keller, "Recent developments in compact ultrafast lasers," *Nature* **424**, 831–838 (2003).

[116] U. Keller, K.J. Weingarten, F.X. Kartner, D. Kopf, B. Braun, I.D. Jund, R. Fluck, C. Honninger, N. Matuschek, J.A. der Au, "Semiconductor saturable absorber mirrors (SESAM's) for femtosecond to nanosecond pulse generation in solid-state lasers," *IEEE J. Sel. Top. Quantum Electron.* **2**, (1996).

[117] F. Bonaccorso, Z. Sun, T. Hasan, A. Ferrari, "Graphene Photonics and Optoelectronics," *Nat. Photonics* **4**, 611–622 (2010).

[118] T. Hasan, Z. Sun, F. Wang, F. Bonaccorso, P. H. Tan, A.G. Rozhin, A. Ferrari, "Nanotube-polymer composites for ultrafast photonics," *Adv. Mater.* **21**, 3874–3899 (2009).

[119] W. Cho, J. Yim, S. Choi, S. Lee, A. Schmidt, G. Steinmeyer, U. Griebner, V. Petrov, D. Yeom, K. Kim, F. Rotermund, "Boosting the nonlinear optical response of carbon nanotube saturable absorbers for broadband mode-locking of bulk lasers," *Adv. Funct. Mater*. **20**, 1937–1943 (2010).

[120] H. Zhang, D.Y. Tang, L.M. Zhao, Q.L. Bao, K.P. Loh, "Large energy mode locking of an erbium-doped fiber laser with atomic layer graphene," *Opt. Express* **17**, 17630–17635 (2009).

[121] Z. Sun, T. Hasan, A. Ferrari, "Ultrafast lasers mode-locked by nanotubes and graphene," *Phys. E Low-Dimensional Syst. Nanostructures* **44**, 1082–1091 (2012).

[122] G.Q. Xie, J. Ma, P. Lv, W.L. Gao, P. Yuan, L.J. Qian, H.H. Yu, H.J. Zhang, J.Y. Wang, D.Y. Tang, "Graphene saturable absorber for Q-switching and mode locking at 2μm wavelength," *Opt. Mater. Express* **2**, 878-883 (2012).

Viatcheslav Vanyukov
Effects of nonlinear light scattering on optical limiting in nanocarbon suspensions

This work is devoted to experimental investigation of the nonlinear light scattering and optical limiting in carbon nanotubes and detonation nanodiamonds. The study of third-order nonlinear optical response of these materials in the nanosecond and femtosecond time domains within the visual and near- infrared spectral ranges is presented. The application of carbon nanotubes and nanodiamonds for adjusting nanosecond laser pulse duration is demonstrated. The presented results reveal that aqueous suspensions of detonation nanodiamonds possess a high ray stability and are attractive for optical limiting applications.

UNIVERSITY OF
EASTERN FINLAND